Cyprus University of Technology

Faculty of Engineering and Technology

Ph.D. Dissertation

Effects of Posture Change on the Geometry and Hemodynamics of the Human Carotid Bifurcation

Nicolas Aristokleous

Lemesos 2013

Cyprus University of Technology

Faculty of Engineering and Technology

Department of Mechanical Engineering and Materials Science and Engineering

Effects of Posture Change on the Geometry and Hemodynamics of the Human Carotid Bifurcation

Nicolas Aristokleous

Lemesos 2013

Approval Page

Ph.D. Dissertation

Effects of Posture Change on the Geometry and Hemodynamics of the Human Carotid

Presented by

Nicolas Aristokleous

Academic Supervisor _____

Professor Andreas S. Anayiotos

Committee Member (President) _____

Professor Georgios C. Georgiou

Committee Member _____

Associate Professor Tasos Georgiades

Cyprus University of Technology

July, 2013

Copyright Page

Suggested citation: Nicolas Aristokleous, Effects of Posture Change on the Geometry and Hemodynamics of the Human Carotid Bifurcation. PhD Dissertation, Lemesos, Cyprus University of Technology, 2013.

Acknowledgements

This study represents the PhD Dissertation in the framework of the postgraduate schedule of the department of Mechanical Engineering and Materials Science and Engineering at the Cyprus University of Technology. Before presenting this study I would like to thank all people who helped, contributed and support to this study and especially:

- My supervisor Prof. Anayiotos Andreas, for his supervision and precious guidance and suggestions from the beginning of this study.
- Our collaborators Prof. Georgiou Georgios, Dr. Seimenis Yiannis, Dr. Papaharilaou Yannis and Dr. Hari Radhakrishnan for their constant help and efforts during the past years.
- The work of this thesis has been supported financially by IPE/YGEIA/DYGEIA/ 0609/11 from the Cyprus Research Promotion Foundation.
- Finally, many thanks to my family and friends for their support and the encouragement, in several ways.

Abstract

Cardiovascular diseases (CVD), especially atherosclerosis, continue to be the leading cause of morbidity and mortality and the principal cause of death in the United States, Europe and most of Asia. Scientific research in this field over the last few decades shows that vessel geometry and hemodynamic forces influence vascular pathology. As it is well known, regions of disturbed and oscillatory flow in the circulatory system, like bifurcations and arches, are characterized by low shear stresses, which allow the atherogenesis and the development of atherosclerotic lesions. In general, the nature of the blood flow plays an essential role in determining whether atherosclerotic lesions occur at various vascular sites. This study focuses on the morphological changes of human carotid bifurcation (CB) that may occur as the head is rotated in different postures. These morphological changes of the bifurcation geometry may cause alterations in the blood flow field within the CB and consequently lead to the initiation and/or to the further development of the disease.

The first part of the thesis focuses on the literature review and the theoretical study of the physiology of human carotid bifurcation and the diseases developed in this area, specifically atherosclerosis, and their relation to hemodynamic parameters. It also provides an overview of the basic theory of biofluid dynamics and Magnetic Resonance Imaging (MRI).

The second part presents the work done using medical image acquisition and processing for the construction of three dimensional (3D) surface models. More specifically, by using MR images of human individuals and employing segmentation techniques, the construction of realistic 3D surface models was feasible. This was done to investigate the bifurcation region, and in more detail to assess the geometric changes of normal human carotid bifurcations. Initially, the geometric alterations were estimated for the right and left carotid artery bifurcation (RCA and LCA respectively) in the case of ten volunteers, in two head positions, the neutral supine (SP) and the prone position with rightwards head rotation up to 80 degrees (PPRR). In addition, a third head position was

investigated in the case of two out of the ten volunteers, the prone position with leftwards head rotation up to 80 degrees (PPLR).

The first step was to construct accurate CB models using MR images and to quantify the important geometric features of each model in order to investigate the differences between the supine position and the prone with head rotation. The next step was to use the extracted information from the medical images. This information is in the form of spatial pixel coordinates and intensities that determine the boundaries of the wall and lumen of the carotid arteries. Using this information and by employing specialized segmentation software, the 3D carotid models were constructed consisting of the common carotid artery (CCA), the internal carotid artery (ICA) and the external carotid artery (ECA). Next, using vascular model toolkit (VMTK) software I was able to calculate the following geometric features of each model: a) the bifurcation angle; b) the ICA angle; c) the planarity angle; d) the asymmetry angle; e) the tortuosity; e) the curvature; f) the bifurcation area ratio; h) the ICA/CCA diameter ratio; i) the ECA/CCA diameter ratio; and j) the ECA/ICA diameter ratio.

The results obtained have demonstrated that head rotation positions lead to random and frequent significant changes in geometric parameters. The changes observed may also cause significant changes in the bifurcation hemodynamics environment which is related to the initiation and the development of atherosclerotic disease.

In the third part of the thesis, the evaluation of the influence of head rotation on the flow characteristics took place, with the use of computational fluid dynamics (CFD). More specifically, with a specialized meshing software (ICEM-CFD), using the carotid surface models I proceeded to the construction of the corresponding CB meshes. These were necessary to solve the equations governing the blood flow, which was achieved using the finite volume method. The numerical calculation of the important hemodynamic parameters related with atherosclerosis was carried out on a subject-specific basis in two extensive studies. First, I performed CFD simulations on two volunteers using the same inlet velocity waveform as boundary condition. What I investigated were the changes on RCA and LCA in the three head positions (SP, PPLR and

PPRR). In the second study and on the same volunteers, I performed CFD simulations using the realistic inlet velocity waveform. The results indicated that torsion of the head causes notable changes in spatial distribution of wall regions exposed to unfavorable hemodynamics. Another conclusion was that the effect of geometry on the hemodynamic features was more significant than that of the inlet waveform.

The main conclusion of the thesis is that the head and neck postures may cause significant morphological changes on human CB. These geometric alterations lead to blood flow field alterations, which may be associated with the initiation and development of atherosclerotic disease.

7. What we cannot speak about we must pass over in silence

Ludwig Wittgenstein
Tractatus Logico-Philosophicus

Table of Contents

List of Figures

Figures of Appendices

List of Tables

Tables of Appendices

Nomenclature

Abbreviations

3D	Three-dimensional
2D	Two-dimensional
BAR	Bifurcation area ratio
BFI	Blood flow index
BI	Bifurcation index
CAD	Computer – Aided Design
CB	Carotid bifurcation
CCA	Common carotid artery
CFD	Computational fluid dynamics
CVD	Cardiovascular disease
CV	Control volume
DICOM	Digital Imaging and Communications in Medicine
ECA	External carotid artery
FVM	Finite volume method
ICA	Internal carotid artery
IMT	Intima-media thickness
IQR	Interquartile range
LCB	Left carotid bifurcation
LDL	Low density lipoprotein
MIP	Maximum intensity projection
MRI	Magnetic resonance imaging
NO	Nitric oxide
OSI	Oscillatory shear index
PC-MRI	Phase-contrast MRI
PISO	Pressure implicit with splitting of operators
PPLR	Prone position with leftward rotation up to 80^{o}
PPRR	Prone position with rightward rotation up to 80^{o}
RBC	Red blood cells
RCB	Right carotid bifurcation
RRT	Relative residence time
SP	Supine position
TAWSS	Time-averaged WSS
VMTK	Vascular modeling toolkit
WBC	White blood cells
WSS	Wall shear stress
WSSTG	WSS temporal gradient

Symbols

C	Compliance	m^3/Pa	
D, d	Diameter	m	
D_i	Inlet diameter	m	
D_o	Outer diameter	m	
De	Dean number	-	
E	Young's modulus of elasticity	Pa	
E_{inc}	Incremental elastic modulus	Pa	
El	Elastance	Pa/m^3	
H	Helicity	m^4/s^2	
Ht	Hematocrit	%	
h	Wall thickness	m	
l	Length	m	
LNH	Localized Normilized Helicity	-	
m	Mass	kg	
P	Pressure	Pa, mmHg	
Q	Flow rate	m^3/s, ml/min	
R	Resistance	$dynes \cdot s/m^5$	
Re	Reynolds number	-	
r	Radius	m	
rho	Correlation coefficient	-	
T	Period	s	
u	Velocity, axial direction	m/s	
V	Volume	m^3	
α	Womersley number	-	
$\dot{\gamma}$	Strain rate	1/s	
ΔP	Pressure difference or drop	Pa, mmHg	
Δt	Time step	s	
ε	Strain	-	
κ	Curvature	1/m	
μ	Viscosity (dynamic)	Pa·s	$dynes \cdot s/cm^2$ (P, Poise)
ν	Viscosity (kinematic)	m^2/s	cm^2/s (St, Stokes)
ρ	Density	kg/m^3	
σ	Stress	Pa	
σ_θ	Circumferential (hoop) stress	Pa	
σ_L	Longitudinal (axial) stress	Pa	
σ_R	Radial stress	Pa	
τ	Shear stress	Pa	
τ_w	Wall shear stress	Pa	
ω	Frequency	Hz	rad/s

PART I: INTRODUCTION

Chapter 1:

Introduction

1.1 Motivation and Objective

One of the major causes of morbidity and mortality in the Western world today is stroke, with carotid disease representing an important contributory risk factor [1]. Stroke is the third leading cause of death in the United States (US), resulting in 137,119 deaths in 2006, and accounts for approximately 795,000 cases each year, 610,000 of which are first-time attacks [2]. Updated data for 2013 reports that cardiovascular disease (CVD) causes over 800,000 deaths in US and 1.9 million in the European Union (EU) per year, amounting respectively to 32 % and 40 % of all deaths [3, 4]. Asymptomatic carotid stenosis constitutes a significant risk factor for stroke with a prevalence of 2-8 % and carotid stenosis is responsible for 15-20 % of all strokes [5]. Several studies over the years have demonstrated that the geometry of the carotid bifurcation determines blood flow patterns and have postulated that it directly influences the formation of atherosclerotic plaques [6-9].

The first hemodynamic hypothesis that implicates high wall shear stress (WSS) in the development of atherosclerosis in large arteries was reported by Fry in 1968 [10]. Fry described that the acute yield stress for endothelial cells was found to be 379 ± 85 dynes/cm^2 and the exposure of endothelial cells above this stress value for periods as short as one hour resulted in changes such as cell deformation, swelling, and ultimate dissolution [10]. The second hypothesis involves low shear stress and was reported by Caro *et al.* in 1971 [11]. Contrary to what Fry reported, Caro and associates showed that the distribution of early atheroma coincides with the regions in which arterial wall shear rate is expected to be relatively low [11].

Atherosclerosis is not only influenced by local arterial hemodynamics, but it is also linked to genetic multiple risk factors including genetic predesposition, hypertension, smoking, hyperlipidemia, social stress, and diabetes mellitus, among others [8, 12, 13]. Despite the systemic nature of its associated risk factors, atherosclerosis is a geometrically focal disease and atherosclerotic plaques arise in geometrically complex regions of large arteries. Such vasculature regions are arterial bifurcations and regions of high curvature that experience a complicated blood flow field, containing regions of

low and high mean shear stress as well as areas of flow reversal and possible flow separation. In adult human vessel branches, lesions are more likely to form along the outer wall of the vessel branch, where the WSS is relatively low as shown in **Fig. 1** [8, 14-16]. The critical WSS values were estimated from in vitro studies, and more specifically the WSS below 4 dynes/cm^2 are called low WSS, shear stress levels of 10 to 15 dynes/cm^2 are known as normal WSS values and induces atheroprotective endothelial gene expressions (**Fig. 1**) [8, 17]. High WSS refers for values above 70 dynes/cm^2.

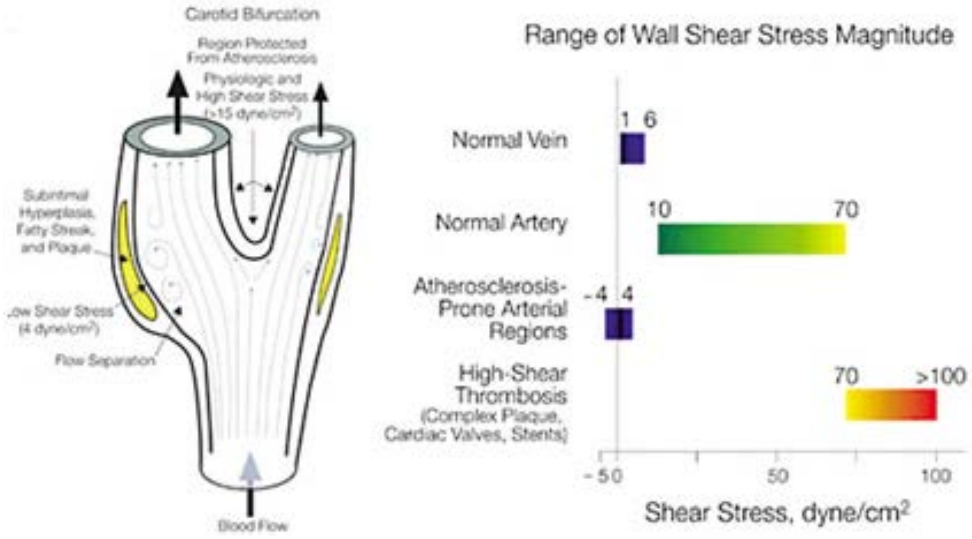

Figure 1: Schematic illustration of atherosclerosis tendency to involve the outer walls of vascular bifurcations (left), and the range of WSS magnitudes (right) (from [8] without permission).

In the present study, magnetic resonance imaging (MRI) was performed on the right and the left carotid artery bifurcations (RCB and LCB) on ten healthy male volunteers in two head positions: a) the supine neutral position (SP), b) the prone rightward rotation head position (PPRR) up to 80 degrees. For two out of ten volunteers, the prone with leftward rotation head position (PPLR) up to 80 degrees was also investigated. Furthermore, for six volunteers cross-sectional flow velocity distribution was obtained using phase-contrast MRI (PC-MRI) at the common carotid artery (CCA). Finally, a group of four patients with a hemodynamically moderate to significant stenosis (60-75 %) at the origin of the internal carotid artery (ICA) were imaged by MRI for the supine head position and the prone position with leftwards rotation. The anatomic MR data was used to construct

the solid models of carotid bifurcations. The three-dimensional (3D) surface models were spatially discretized into the computational domain where the governing fluid equations were solved numerically. The blood flow field solution gives the results for further investigation and allows comparisons of hemodynamic factors that are essential in the genesis and development of atherosclerosis.

1.2 Aims

This study aims at investigating the changes in the geometric parameters of the carotid artery bifurcation with head rotation and their influence on hemodynamic variables, which are known to contribute to the initiation and development of atherosclerotic disease.

The first step was the survey of existing studies on the hemodynamic hypothesis and the role of morphological and hemodynamic parameters. The main part of this study involved the construction of bifurcation solid models from MR imaging and the definition and calculation of the important geometric parameters for these models. The next step was the construction of the corresponding meshes and the computational fluid dynamics (CFD) analysis using the finite volume method. CFD analysis was used to investigate the complex 3D blood flow and to calculate the hemodynamic parameters assumed to play a key role in atherosclerosis. Finally, a comparative study was necessary for the assessment of the geometric and hemodynamic alterations in different head postures. This was done to identify any differences in geometric and hemodynamic parameters attributed to changes in head posture and if those alterations may be associated with atherosclerosis disease development.

In conclusion, this study focused on:

A. **An extended literature review**
B. **Construction of realistic 3-dimensional carotid artery bifurcation models from MR images**
C. **Definition and quantification, from the solid models, of important geometric features related with carotid bifurcation geometry**

D. **Statistical analysis of the changes of the geometric parameters related to the changes when the head is rotated**
E. **Construction of meshes of the 3-D bifurcation models and the CFD analysis using the finite volume method**
F. **Quantification and comparison of the important hemodynamic factors related to atherogenesis and development of atherosclerosis.**

1.3 Thesis Outline

This thesis aims to present that the head rotation influences the geometry and hemodynamics of the human carotid bifurcation.

This study was performed at the Biomechanics and Living Systems Analysis Laboratory (BIOLISYS) in the Department of Mechanical Engineering and Materials Science and Engineering of Cyprus University of Technology under the supervision of Prof. Andreas Anayiotos. Well established methodology was applied for the study, including MR images, construction of 3D surface models, definition and quantification of important geometric features and computational calculations.

The first part of this thesis deals with medical and engineering research in the area of human carotid bifurcation and the various parameters that correlate with the development of atherosclerosis at this region. In Chapter 1 and 2 the specific aims of this study and a general literature review are presented.

Chapter 3 deals with the human cardiovascular system and more specific with the carotid bifurcation physiology and functionality. Also, this chapter reviews the very basics of the hemodynamics.

A brief review of Magnetic Resonance Imaging is provided in Chapter 4, as well as an introduction and a description for this modern non-invasive imaging technique which was used to obtain the information from MR images in order to construct the surface models.

The second part is on the construction of 3D surface models from MR images and the calculation of the geometric parameters. In this part, Chapter 5 deals with the image processing, the methodology and the optimization of various techniques exercised and applied for the rest of the study. This was done by trying different software for image processing to discover the most convenient for the purposes of this study, and also to evaluate the accuracy and the robustness of results by a reproducibility study.

In Chapter 6, a broad description of geometric parameters of the carotid bifurcations of the volunteers that were measured is offered, followed by the results for all the investigated head postures. These results were found to be in accordance with similar findings from a much larger sample of volunteers in terms of all geometric parameters. The results show that for all volunteers there are significant changes in the geometric parameters of the carotid bifurcation when the head is rotated. This was observed for both carotid bifurcations. These changes are random and there is no predisposition for a specific direction of change for any of the parameters extracted. The variable changes observed might be due to the considerable variability in the baseline geometry among subjects. Nevertheless, head rotation towards a specific direction could have different effect on the same geometric feature for the two CBs of the same volunteer.

In Chapter 7, the description of the methodology to construct accurate meshes from the existing 3D models and to perform numerical simulations is described. The results of an extensive meshing independence study are presented and the boundary conditions that were used throughout this study are explained.

In Chapters 8 and 9, the results of the CFD simulations and the effect of head posture on CB hemodynamics head are presented. In more detail Chapter 8 provides the investigation of three head postures with the use of the same inlet waveform. Chapter 9 is an account of a patient-specific study, in which the realistic inlet waveform was applied for each volunteer.

In conclusion, head rotation inflicts changes on the geometric and hemodynamic characteristics of the carotid bifurcation. These alterations affect and influence the

exposure of the arterial wall to hemodynamic features related with atherosclerotic disease. The prominent intersubject variability of these changes indicates that an individualized approach for the evaluation of the potential risks that head posture may pose on atherosclerotic plaque deposition and/or rupture of existent vulnerable lesions as well as on potential fractures of stents with carotid bifurcations is preferable.

Chapter 2:

Literature Review

2.1 Literature Review - Related work

The mechanical irritation of the arterial wall caused by blood flow in the artery affects the inner arterial surface, which is composed of endothelial cells. In pathological conditions, this interaction is a contributing factor to atherosclerosis. This effect was described in the 1870s, mostly by Leonhard Euler (1707-1783) and Thomas Young (1773-1829) [18, 19]. The early studies focused on wave propagation in arteries but do not appear to have investigated the blood flow field in arteries. The hemodynamic hypothesis of atherosclerosis was introduced by Fry (1968) [10] and then by Caro *et al.* (1971) [11]. The first advocated high while the other low WSS as the cause of atherosclerosis [18]. Several scientific studies suggested that large arteries, and more specifically the carotid arteries, represent significant regions in the development of atherosclerosis [14, 15, 20, 21], the principal cause of heart attacks, stroke and gangrene of the extremities [22]. Several global factors associated with and contributing to the development and acceleration of large vessel atheroma include hypertension, smoking, hypercholesterolemia, aging and diabetes mellitus [8, 13, 20, 22-25]. However, despite the systemic nature of the associated global risk factors, atheroma is essentially a geometrically focal disease [5, 19, 20, 26-28].

Atherosclerosis is an inflammatory disease that arises due to high plasma concentrations of cholesterol, and in particular the low-density lipoprotein (LDL) cholesterol. The first mechanism that takes place is atherogenesis, which involves the accumulation of lipids at the artery wall [22, 25]. Atherogenesis preferentially involves the outer walls of large and medium sized elastic and muscular arteries as well as vessel bifurcations. In these regions blood flow recirculation and stasis is observed [8, 24].

Numerous studies in humans and animals have led to the formulation of a response to the injury hypothesis of atherosclerosis. It was initially proposed that the endothelial denudation was mainly responsible for atherogenesis, but most recent studies emphasize endothelial dysfunction rather than denudation [13, 29]. The normal endothelium cells do not support binding of white cells; nonetheless, in abnormal cases, they begin to express on their surface selective adhesion molecules that bind to various

classes of leukocytes (monocytes, macrophages etc.) [25, 30]. Possible causes of endothelial dysfunction have already been mentioned as the global factors that are associated with and seem to contribute to the genesis and development of atheroma [31]. When the endothelial layers sustain injury, the immune system is activated and leads to the alteration of the normal homeostatic properties of the endothelium. Immune system activation at the injury sites along the endothelium increases the adhesiveness of leukocytes and platelets membrane permeability, which is consistent with a change from procoagulant to anticoagulant vessel properties/characteristics. When the inflammatory response is not neutralized, it can continue indefinitely, and as a result stimulate migration and accumulation of smooth muscle and collagen accretion which allow rapid evolution of a fatty lesion and become intermixed with the inflammation area [31]. This phenomenon is known as remodeling of the endothelium cells [13]. If inflammation persists, further endothelium damage eventually leads to focal necrosis, and as the lesion is further enlarged and restructured, it becomes covered by a fibrous cap that overlies a core of lipid and necrotic tissue. All these structure alterations affect artery elasticity and the lesion may then intrude into the lumen and alter the flow of blood [13].

Regions of uniform geometry are exposed to a unidirectional and laminar blood flow, which produce physiological values of WSS [9]. Endothelium layer responds in various temporal and spatial shear stress patterns and translates the force into a biological response such as: a) atheroprotection, b) atherogenesis and c) vascular remodeling – arteriogenesis [32]. Atherosclerotic lesions occur preferentially at arterial branches, bifurcations and along curved arteries as these regions exhibit blood flow alterations, with an accompanying decrease of shear stress and increase of turbulence. Changes in blood flow alter the expression of genes that have elements responding to shear stress changes in their promoter regions. Alterations in flow appear to be crucial in determining which arterial sites are prone to have lesions [8, 9, 13-15, 21, 33, 34]. Zhang *et al.* performed CFD simulations on different shapes of internal carotid artery (ICA) branches and found that the large curvature and planarity of vessels increase the risk of

stenosis, because of the low WSS, and elevate oscillatory shear index (OSI) [35]. Recent studies of Knight *et al.* [36] and Rikhtegar *et al.* [37] showed that time-averaged WSS (TAWSS) identify accurately the regions with large number of plaques. Also, they report that these regions could be predicted using a low TAWSS threshold, but this produces more false positives than the uses of OSI and relative residence time (RRT). Finally, the low and oscillatory WSS are involved in the early stages of atherosclerotic disease and also implicated in the late stages of the disease [38]. On the contrary, a recent systemic review study claims that the evidence for the low and oscillatory shear theory so far, is less robust than commonly assumed [39].

Previous studies have shown that regions of low and oscillatory shear stress and areas of flow separation, and disrupted and turbulent flows, cause reduction to nitric oxide (NO) production and other atheroprotective substances such as prostacyclin (PGI2) and tissue plasminogen activator (tPA) [31, 40, 41]. NO is known as the most potent vasodilator which inhibits platelet adherence and aggregation and occurs within seconds after the application of increased shear stress [42]. Moreover, it reduces leukocytes adherence to the endothelium layer and suppresses proliferation of vascular smooth muscle cells [43, 44]. Furthermore, Bao *et al.* [45] found that a temporal gradient in shear stimulates the expression of monocyte chemoattractant protein-1 (MCP-1), a potent chemotactic agent for monocytes, and platelet derived growth factor A (PDGF-A), a potent mitogen and chemotactic agent for smooth muscle cells. From the biological aspect, Resnick *et al.* [32] describe extensively the complex interaction of shear stress and the vascular endothelium. More findings indicate that endothelial cells can discriminate between loading variations which may include temporal and spatial WSS gradients variations [17]. Bao *et al.* [45] first compared the induction of the atherogenetic-related genes, PDGF-A and MCP-1 in endothelium cells exposed to steady and temporal gradient WSS (WSSTG) and suggest distinct roles between them. Essentially, they found that WSSTG in the absence of steady WSS stimulates the expressions of the genes related to atherogenesis. An extensive review by Chiu and

Chien [28] summarizes the endothelium signaling, gene expression and functionality and the role of disturbed flow in endothelium physiology and pathophysiology.

The importance of hemodynamics in the development of atherosclerosis disease led many researchers to study blood flow distribution and wall shear stress caused by flow. Friedman et al. [14] found a negative correlation between intima-media thickness (IMT) and wall shear rate. A similar study from Ku et al. [15] using also a realistic pulsatile flow, found strong correlations between IMT and the reciprocal of maximum shear stress or the reciprocal of mean shear stress. They also found that the OSI correlated strongly with IMT. Recently, in a 20 year follow up study with more than 3000 volunteers, Polak *et al.* found that the average of the maximum IMT in the CCA is more strongly associated with cardiovascular risk than IMT measurements made in the bulb or ICA [46]. Zarins et al. [21] concluded that in the human carotid bifurcation, regions of moderate to high shear stress, where flow remains unidirectional and axially aligned, are relatively spared of intimal thickening. Furthermore, they mentioned that the IMT and atherosclerosis are developed in large regions of relatively low WSS, flow separation, and departure from axially aligned, unidirectional flow.

Several reports highlight the importance of posture change on carotid artery, which may alter morphology and hemodynamic characteristics. A study in premature infants in 2001 showed that head position influenced the cerebral blood flow [47] and later Dimitriou *et al.* investigated the influence in three different head postures on oxygenations again in infants [48]. Glor et al. performed an ultrasound imaging study of the carotid bifurcation and looked at the effects of head rotation in nine patients [49]. They noted that head rotation changed the distribution of WSS and OSI primarily due to flow rate changes in the rotated position. They also reported “planarification” of the common carotid artery (CCA) and changes in centerline location of the vessel with rotation of the head. In contrast, an older study by Caro *et al.* suggested that non-planarity is an important parameter that influences the blood flow in arteries [50].

Earlier studies employing rigid and compliant models for the study of the arterial bifurcations and curvature regions, provided limited velocity and WSS estimations and

correlation of atherosclerotic lesion locations [15, 51-53]. A better approach is the use of 3D carotid bifurcation models and CFD to reconstruct the hemodynamic flow field. Perktold *et al.* first worked on 3D models and provided numerical results in time-varying flow [53-55]. These studies concluded on the existence of complex flow at the carotid bifurcation and the correlation of the location of atherosclerotic plaques with the regions of low and oscillating WSS. A step further was the image-based modeling of blood flow, the combination of 3D imaging techniques with CFD algorithms. The modern non-invasive imaging modalities such as ultrasound and MRI and also the invasive intravascular ultrasound (IVUS), computed tomographic (CT) imaging, and X-ray give potential for accurate imaging of the lumen and the arterial wall and the blood velocity within the artery [56]. A brief overview of the progress achieved in the field of image-based CFD studies was done by Steinman and Taylor [56, 57]. Also, an extensive review in experimental and computational methods for quantifying blood flow velocity and pressure fields in arteries was done by Taylor and Draney [58]. The methodology employed in the present work, from MR images to numerical CFD, is well established and widely applied by many groups and researchers who work in the same field [20, 59-64]. Furthermore, the combination of MRI with CFD allows for more accurate, robust, efficient and highly reproducible results, as it was recently shown by Bijari *et al.* [65] and previously by other researchers [59, 66-73]. Glor *et al.* compared MRI and ultrasound and the results for many hemodynamic parameters included WSS, WSS gradients, OSI, WSS angle gradients (WSSAG) represented qualitatively and quantitatively similar [74-76]. In a similar study, Goubergrits *et al.* compared MRI and CT using a silicon model of the left coronary artery main bifurcation. The calculated average WSS shows high correlation and agreement among the modalities [71].

The progress in image-based modeling with more realistic geometries and boundary conditions enables more accurate calculation and prediction of various hemodynamic markers. It is essential at the same time, to approach the atherosclerotic disease from personalized medicine, involving and validating novel markers associated with gene factors, environmental factors, and gene-by-environment interactions [77]. Finally,

imaged-based modeling techniques and patient-specific analyses of disease progression should be used more frequently for the diagnosis, treatment, interventional and surgical planning and evaluation of the safety and efficiency of cardiovascular devices [56, 78].

The overall principle of physiological and biological events that was followed in this study is described in Fig. 2 and was found in Hyum *et al.* [79].

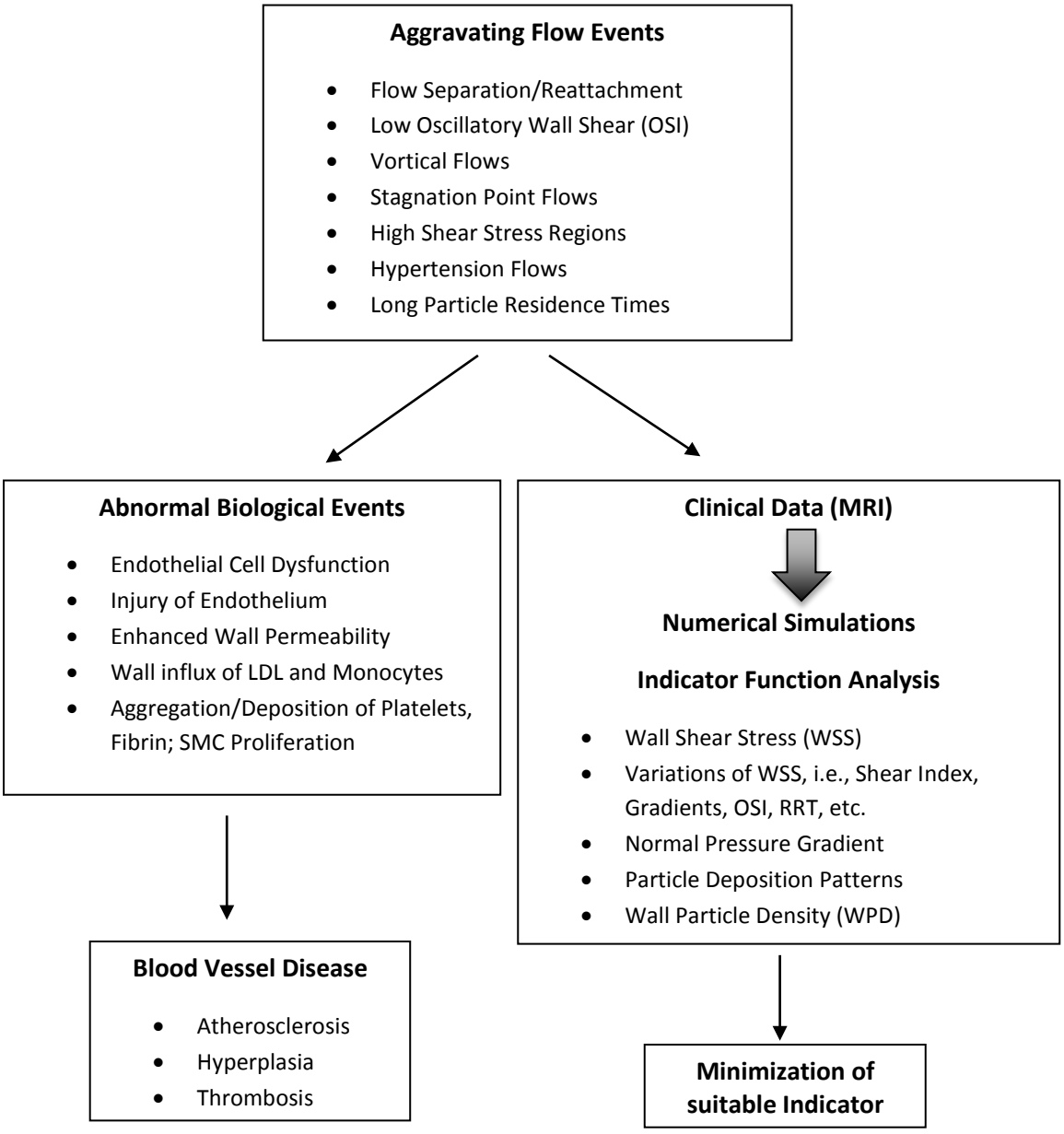

Figure 2: Overview of physio-biological events that outlined the methodology that was followed in this study (from [79], without permission).

2.2 Anatomy, Morphology and Functionality of Cardiovascular System

2.2.1 The Cardiovascular System

The heart and the circulatory system constitute the cardiovascular system which is responsible to service the needs of the body tissues. The human body's circulatory system has three distinct parts: a) the heart (coronary circulation), which is the pump station and basically functions as two separate pumps, b) the right heart that pumps the blood towards the lungs (pulmonary circulation), and c) the left heart that pumps blood through the peripheral organs (systemic circulation) [80]. A schematic of the circulatory system is illustrated in Fig. 3. The function of the circulation is to transport nutrients to the body tissues, to transport waste products away, to transfer hormones from one part of the body to another, and in general, to maintain an appropriate environment in all the tissue fluids of the body for optimal survival and function of the cells. An average human body has roughly five liters of blood moving through the circulatory system without stopping. The functionality of the circulation system is based on the complex configuration of blood vessels that successively branch into smaller vessels down to the capillaries [80].

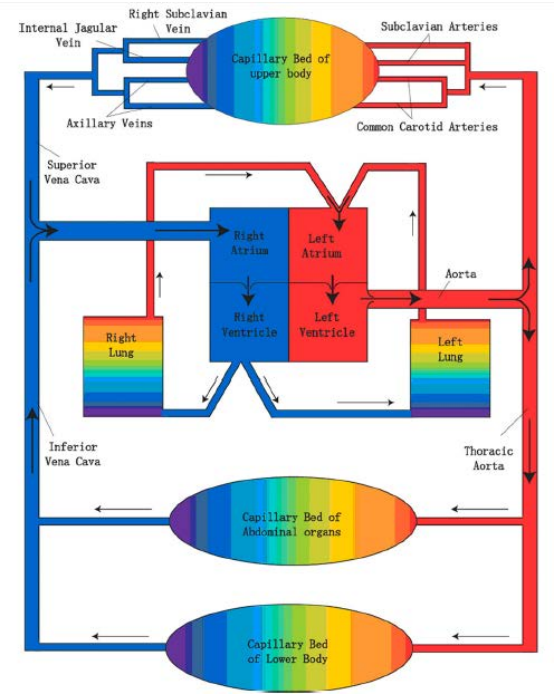

Figure 3: The blood circulation system [from [80] without permission].

2.2.2 The Heart

The heart is a hollow muscular organ of a somewhat conical form. It lies between the lungs in the middle mediastinum and is enclosed in the pericardium (Fig. 4). The heart is placed obliquely in the chest behind the body of the sternum and adjoining parts of the rib cartilages, and projects farther into the left than into the right half of the thoracic cavity, so that about one-third of it is situated on the right and two-thirds on the left of the median plane [81].

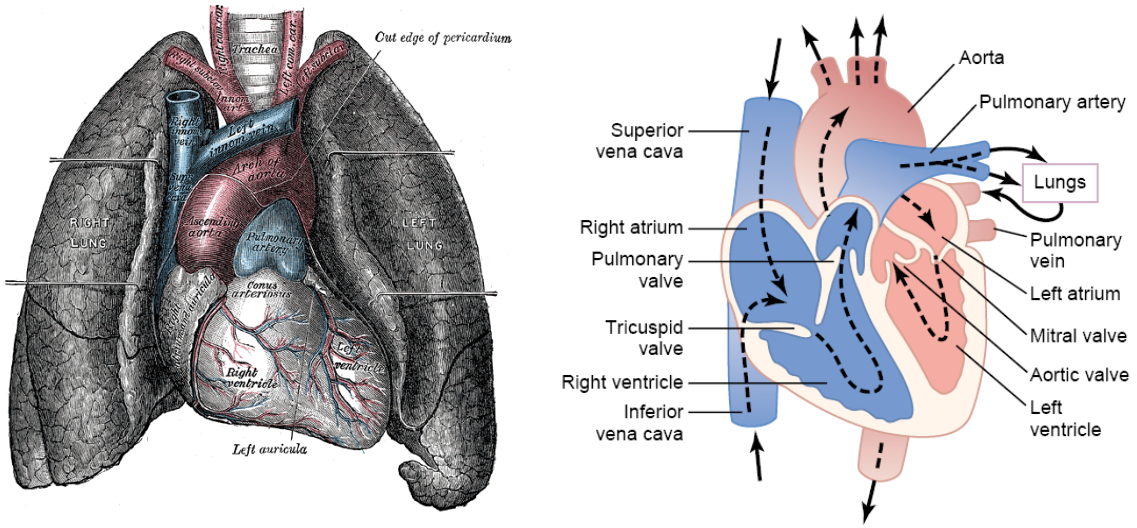

Figure 4: Left: Front view of heart and lungs. Right: Human heart anatomy, and course of blood flow (from [81, 82] without permission).

The heart, in the adult, measures about 12 cm in length, 8 to 9 cm in breadth at the broadest part, and 6 cm in thickness. In the male its weight varies from 280 to 340 g, and in the female, from 230 to 280 g [82]. Furthermore, the heart consists of four chambers, divided by a tough muscular wall, the interatrial-interventricular septum. It is divided into right and left halves and each half is further subdivided into two cavities, the upper parts called the atria and the lower parts called the ventricles. The reason that the heart has two sides is related to the pressure-flow characteristic of the pulmonary and systemic circulation [83]. The left side of the heart drives oxygen-rich blood through the aortic valve into the systemic circulation, which carries the fluid to a different neighborhood of each cell in the body. From there, the low in oxygen and rich

in carbon dioxide blood returns to the right side of the heart which drives this oxygen-poor blood through the pulmonary valve into the pulmonary circulation. Blood is then carried to the lungs, where its oxygen supply is replenished and its carbon dioxide content is purged before it returns to the left side of the heart to begin the cycle all over again.

2.2.2.1 The Cardiac Cycle

The cardiac events that occur from the beginning of one heartbeat to the beginning of the next are called the cardiac cycle. The cardiac cycle consists of a period of relaxation called diastole, during which the heart fills with blood, followed by a period of contraction called systole [82].

Electrocardiography (ECG or EKG) helps in the interpretation and record of the electrical activity of the heart. A typical ECG graph of the cardiac cycle consists of a P wave, a QRS complex, and a T wave as shown on Fig. 5.

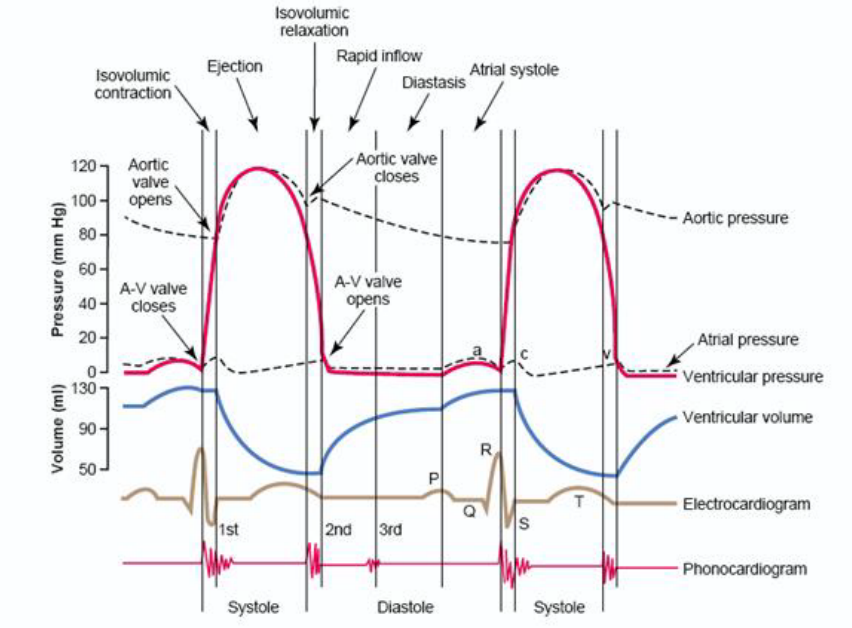

Figure 5: Wiggers diagram shows events of the cardiac cycle for the left ventricular function, showing changes in left atrial and ventricular pressure, aortic pressure, ventricular volume, the electrocardiogram, and the phonocardiogram (from [82] without permission).

The diagram on Fig. 5 is called the Wiggers diagram, which shows the various events during the cardiac cycle for the left side of the heart. The first three curves show the pressure changes in the aorta, left ventricle (LV), and left atrium (LA) respectively. The fourth curve shows the volume change in LV, the fifth shows the electrocardiogram and the sixth curve is a phonocardiogram which is a recording of the sounds produced by the heart (mainly by the heart valves) as it pumps.

2.2.3 The Blood Vessels

The blood vessels transporting blood from the heart to the various organs in the body and back to the heart undergo tremendous changes in both size and composition throughout the arterial tree. Depending on their size, structure and function, vessels are categorized as arteries, arterioles, capillaries, venules and veins. Some physical characteristics of the blood vessels are summarized in Table 1 for arterial vessels and in Table 2 for venous vessels. The blood and the cells exchange substances by diffusion, via selective and specific permeation through two different biomembranes, the cell membrane and the capillary wall [80].

The anatomical structure of the arteries and veins consist of the same five distinct layers. From innermost to outermost, these layers are: a) the luminal *glycocalyx*, a thin layer of macromolecules which is usually less than 100 nm; b) the *endothelium*, a single layer of endothelium cells, which are elongated in the blood flow direction; c) the thinnest *tunica intima*, a continuous lining consisting of a single layer of endothelial cells, the *internal elastic lamina* is a thick elastic band which separates the tunica intima from the next wall layer; d) the thickest *tunica media*, composed of numerous circularly arranged elastic fibers, especially prevalent in the largest blood vessels on the arterial side, the *external elastic lamina* is another thick elastic band which separates the external elastic lamina from the next wall layer; and e) the medium-sized *tunica adventitia*, an outer vascular sheath consisting entirely of connective tissue [84, 85]. These layers represented schematically in the Fig. 6A.

The largest vessels have such thick walls that they require a separate network of tiny blood vessels, the *vasa vasorum*, just to service the vascular tissue itself. Blood vessel structure is directly related to the heart's function; the thick-walled large arteries and main distributing branches are designed to withstand the pulsating 80 to 130 mmHg blood pressure that they must endure. The smaller elastic conducting vessels need only to operate under steadier blood pressures in the range 70 to 90 mmHg, but they must be thin enough to penetrate and course through organs. Arterioles operate at blood pressures between 45 to 70 mmHg and the smallest capillary operate at blood pressures of 10 to 45 mmHg. Traveling back up the venous side, blood pressures continuously decreases from around 30 mmHg to near zero, so these vessels can be thin-walled without disease consequence.

Fig. 6B represents the overview of the circulation and gives the percentage of the total blood volume over the entire circulation system.

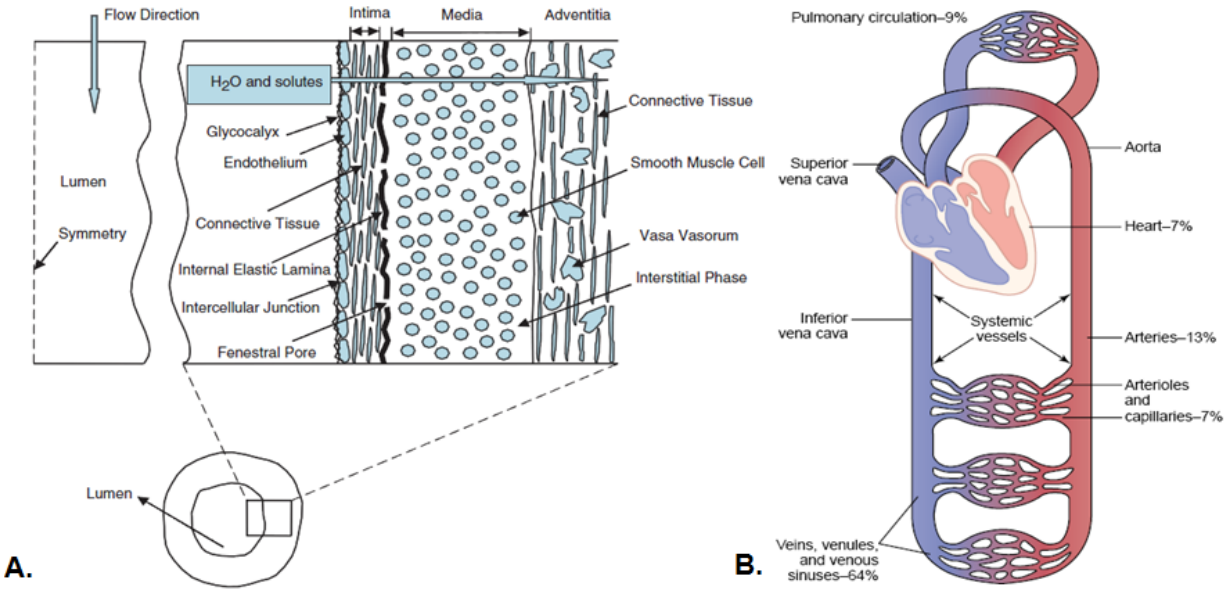

Figure 6: A. The arterial wall layers and B. The blood distribution (% of total blood) in the different blood vessels (from [85] and [82] respectively, without permission).

Table 1: Arterial System(from [84] without permission).

Blood Vessel Type	(Systemic) Typical Number	Internal Diameter Range	Length Range†	Wall Thickness	Systemic Volume	(Pulmonary) Typical Number	Pulmonary Volume
Aorta	1	1.0–3.0 cm	30–65 cm	2–3 mm	156 ml	—	—
Pulmonary artery	—	2.5–3.1 cm	6–9 cm	2–3 cm	—	1	52 ml
Wall morphology: Complete tunica adventitia, external elastic lamina, tunica media, internal elastic lamina, tunica intima, subendothelium, endothelium, and vasa vasorum vascular supply							
Main branches	32	5 mm–2.25 cm	3.3–6 cm	≃2 mm	83.2 ml	6	41.6 ml
(Along with the aorta and pulmonary artery, the largest, most well-developed of all blood vessels)							
Large arteries	288	4.0–5.0 mm	1.4–2.8 cm	≃1 mm	104 ml	64	23.5 ml
(A well-developed tunica adventitia and vasa vasorum, although wall layers are gradually thinning)							
Medium arteries	1152	2.5–4.0 mm	1.0–2.2 cm	≃0.75 mm	117 ml	144	7.3 ml
Small arteries	3456	1.0–2.5 mm	0.6–1.7 cm	≃0.50 mm	104 ml	432	5.7 ml
Tributaries	20,736	0.5–1.0 mm	0.3–1.3 cm	≃0.25 mm	91 ml	5184	7.3 ml
(Well-developed tunica media and external elastic lamina, but tunica adventitia virtually nonexistent)							
Small rami	82,944	250–500 μm	0.2–0.8 cm	≃125 μm	57.2 ml	11,664	2.3 ml
Terminal branches	497,664	100–250 μm	1.0–6.0 mm	≃60 μm	52 ml	139,968	3.0 ml
(A well-developed endothelium, subendothelium, and internal elastic lamina, plus about two to three 15-μm-thick concentric layers forming just a very thin tunica media; no external elastic lamina)							
Arterioles	18,579,456	25–100 μm	0.2–3.8 mm	≃20–30 μm	52 ml	4,094,064	2.3 ml
Wall morphology: More than one smooth muscle layer (with nerve association in the outermost muscle layer), a well-developed internal elastic lamina; gradually thinning in 25- to 50-μm vessels to a single layer of smooth muscle tissue, connective tissue, and scant supporting tissue.							
Metarterioles	238,878,720	10–25 μm	0.1–1.8 mm	≃5–15 μm	41.6 ml	157,306,536	4.0 ml
(Well-developed subendothelium; discontinuous contractile muscle elements; one layer of connective tissue)							
Capillaries	16,124,431,360	3.5–10 μm	0.5–1.1 mm	≃0.5–1 μm	260 ml	3,218,406,696	104 ml
(Simple endothelial tubes devoid of smooth muscle tissue; one-cell-layer-thick walls)							

*Vales are approximate for a 68.7-kg individual having a total blood volume of 5200 ml.
†Average uninterrupted distance between branch origins (except aorta and pulmonary artery, which are total length).

Table 2: Venous System (from [84] without permission).

Blood Vessel Type	(Systemic) Typical Number	Internal Diameter Range	Length Range	Wall Thickness	Systemic Volume	(Pulmonary) Typical Number	Pulmonary Volume
Postcapillary venules	4,408,161,734	8–30 μm	0.1–0.6 mm	1.0–5.0 μm	166.7 ml	306,110,016	10.4 ml
(Wall consists of thin endothelium exhibiting occasional pericytes (pericapillary connective tissue cells) which increase in number as the vessel lumen gradually increases)							
Collecting venules	160,444,500	30–50 μm	0.1–0.8 mm	5.0–10 μm	161.3 ml	8,503,056	1.2 ml
(One complete layer of pericytes, one complete layer of veil cells (veil-like cells forming a thin membrane), occasional primitive smooth muscle tissue fibers that increase in number with vessel size)							
Muscular venules	32,088,900	50–100 μm	0.2–1.0 mm	10–25 μm	141.8 ml	3,779,136	3.7 ml
(Relatively thick wall of smooth muscle tissue)							
Small collecting veins	10,241,508	100–200 μm	0.5–3.2 mm	≃30 μm	329.6 ml	419,904	6.7 ml
(Prominent tunica media of continuous layers of smooth muscle cells)							
Terminal branches	496,900	200–600 μm	1.0–6.0 mm	30–150 μm	206.6 ml	34,992	5.2 ml
(A well-developed endothelium, subendothelium, and internal elastic lamina; well-developed tunica media but fewer elastic fibers than corresponding arteries and much thinner walls)							
Small veins	19,968	600 μm–1.1 mm	2.0–9.0 mm	≃0.25 mm	63.5 ml	17,280	44.9 ml
Medium veins	512	1–5 mm	1–2 cm	≃0.50 mm	67.0 ml	144	22.0 ml
Large veins	256	5–9 mm	1.4–3.7 cm	≃0.75 mm	476.1 ml	48	29.5 ml
(Well-developed wall layers comparable to large arteries but about 25% thinner)							
Main branches	224	9.0 mm–2.0 cm	2.0–10 cm	≃1.00 mm	1538.1 ml	16	39.4 ml
(Along with the vena cava and pulmonary veins, the largest, most well-developed of all blood vessels)							
Vena cava	1	2.0–3.5 cm	20–50 cm	≃1.50 mm	125.3 ml	—	—
Pulmonary veins	—	1.7–2.5 cm	5–8 cm	≃1.50 mm	—	4	52 ml
Wall morphology: Essentially the same as comparable major arteries but a much thinner tunica intima, a much thinner tunica media, and a somewhat thicker tunica adventitia; contains a vasa vasorum							

Total systemic blood volume: 4394 ml—84.5% of total blood volume; 19.5% in arteries (~3:2 large:small), 5.9% in capillaries, 74.6% in veins (~3:1 large:small); 63% of volume is in vessels greater than 1 mm internal diameter

Total pulmonary blood volume: 468 ml—9.0% of total blood volume; 31.8% in arteries, 22.2% in capillaries, 46% in veins; 58.3% of volume is in vessels greater than 1 mm internal diameter; remainder of blood in heart, about 338 ml (6.5% of total blood volume)

2.2.3.1 Geometry and Mechanical Properties of Blood Vessels

The branching structure of blood vessels can be viewed as a simple consequence of the necessity in providing an efficient vascular network for distribution of blood flow. The cardiovascular system consists of the arterial tree, with the bifurcation being the simplest form of branching. Zamir in 1999 termed the arterial tree structure "pseudo-fractal" as the vessels of different calibers represent the same branching pattern but with a range of values of the branching parameters [86].

The vascular structure of bifurcation form in which the "mother" or source vessel bifurcates into two "daughter" or branching vessels, and which undergoes further bifurcation for generations, is known as the "open tree" structure (Fig. 7). The two common carotid arteries represent a long, uniform, bifurcation structure [87]. Good correlations have been found for the extent of bifurcation vessel lengths and diameters. Three properties of the bifurcation are [86, 87]:

a) the bifurcation index (BI) which is a measure of the relative diameters of the two daughter branches

$$BI = \frac{D_2}{D_1} \tag{2.1}$$

b) the bifurcation area ratio (BAR) which is a measure of bifurcation symmetry

$$BAR = \frac{D_1^2 + D_2^2}{D_0^2} \tag{2.2}$$

c) The power law index which gives the relation of vessel diameters and will be extensively discussed in the next paragraph.

$$D_0^n = D_1^n + D_2^n \tag{2.3}$$

A large part of the branching vasculature of the mammalian circulatory obeys Murray's law, which states that the cube of the radius of a parent vessel equals the sum of the cubes of the radii of the daughters. Where this law is obeyed, a functional relationship exists between vessel radius and volumetric flow, average linear velocity of flow, velocity profile, vessel-wall shear stress, Reynolds number, and pressure gradient in individual vessels [88-90].

Murray's law or cube law states that in order to achieve a minimum amount of the rate of energy, the blood flow (Q) required to perfused in a blood vessel must be proportional to the cubic power of the radius (r). For a bifurcation, based on the conservation of mass, it holds that:

$$Q_0 = Q_1 + Q_2 \tag{2.4}$$

where $Q = V_{mean}\pi r^2$ and according to Murray's law

$$r_0^3 = r_1^3 + r_2^3 \tag{2.5}$$

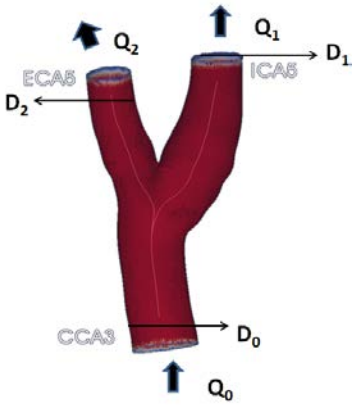

Figure 7: Carotid bifurcation with mother branch of diameter D_0 divided into two daughter branches of diameters of D_1, D_2. Q is the blood flow.

Although many studies in the past proposed that the cube law exist in the artery tree [88-91] recently, Beare *et al.* in a study of 45 subjects using computer tomographic angiography images concluded that Murray's law may not apply at the carotid bifurcations [92]. In a review study, Cheng *et al.* found that for WSS in large arteries the square law applies better rather than Murray's law [93]. For this study, Friedman argues that he was unable to come to the same conclusion for Murray's law [94]. Zamir in his studies had earlier found values that are by far different to the values predicted by the cube and square laws [86]. In this study the results from 20 carotid bifurcations and two head postures (n=40) show that Murray's law does exist for the CB geometry, and the results are presented in following sections of this thesis (Table 14 and Appendix II).

Although the artery wall throughout this study will be assumed as rigid, the knowledge of the vessel mechanical properties is essential for the understanding of vascular

functionality. An extensive comparison of several constitutive models, such as pseudoelastic, poroelastic and viscoelastic previously proposed can be found in the study of Vito and Dixon [95]. Below, I will refer to some significant mechanical properties of blood vessels.

Elasticity and Compliance

The deformation behavior of the artery under stress depends on the elasticity and can be calculated by the tangent elastic modulus, defined as the slope of the stress-strain diagram [96]. Elastic modulus is large for stiff materials and small for compliant materials. The materials with linear behavior obey Hooke's law and the slope on the stress-strain diagram is constant and called Young's modulus of elasticity (E) and defined:

$$E = \frac{\sigma}{\varepsilon} \tag{2.6}$$

where σ is the stress defined by $\sigma=F/A$, has the dimensions of pressure or force (F) per unit area (A) and ε is the strain expressed $\varepsilon=\Delta l/l$, is the ratio of extension per unit length for strain in the longitudinal direction. For the radial direction, or perpendicular to the vessel segment length, strain is given by $\varepsilon=\Delta r/r$.

The arterial walls, and in more general the biological tissues, behave as nonlinear materials (Fig.8B), so Young's modulus has no constant value. For these cases the incremental Young's elastic modulus (E_{inc}) was introduced and can be calculated from medical images that are acquired from the peak systolic and diastolic phase according the equation [97]:

$$E_{inc} = \frac{1.5\Delta P r_i^2 r_o}{(r_o^2 - r_i^2)\Delta r} \tag{2.7}$$

where ΔP is the pulse pressure increment
Δr the change in the internal vessel radius over the cardiac cycle
r_i the internal
and r_o the external radius.

Figure 8A shows the radial stress (σ_R), the longitudinal (axial) stress (σ_L) and the circumferential (hoop) stress (σ_θ) which is the dominant and can be estimated by:

$$\sigma_\theta = \frac{PD_i}{2h} \tag{2.8}$$

where h is the wall thickness, P the blood pressure and D_i the inner arterial diameter.

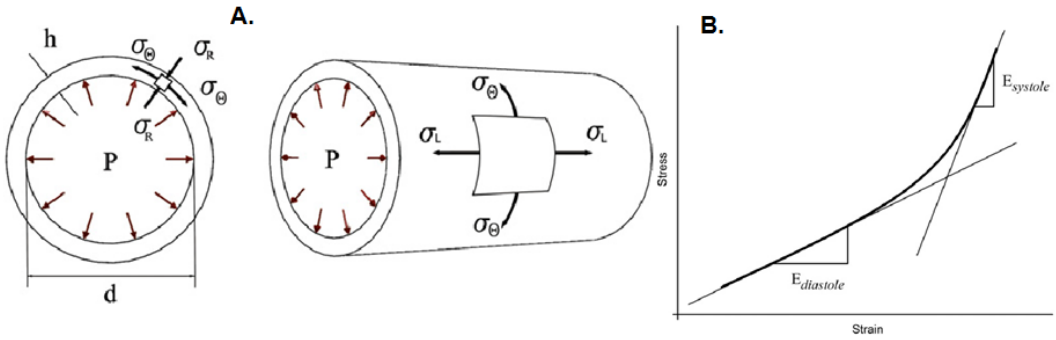

Figure 8: A. Radial stress (σ_R), Longitudinal stress (σ_L) and circumferential stress (σ_θ). B. The stress-strain diagram for CB wall (from [96] without permission).

Compliance

Compliance quantifies the pressure - volume relation and characterizes the flexibility and stiffness of a vessel. Compliance is defined as the local slope on a volume - pressure diagram:

$$C = \frac{\Delta V}{\Delta P} \tag{2.9}$$

More specific, for an artery compliance is estimated by [98]:

$$C = \frac{2}{D_o}\frac{\Delta D_o}{\Delta P} \tag{2.10}$$

where D_o is the outer diameter at P=80 mmHg, and ΔP the pressure difference (120-80 mmHg).

Elastance (El) is a medical term, which also quantifies the stiffness of hollow organs and describes the ability of an organ to return to the original shape after deformation occurred as a result of forces that were applied on it. It is defined as the inverse of compliance [99]:

$$El = \frac{1}{C} = \frac{\Delta P}{\Delta V} \tag{2.11}$$

The normalized compliance is called distensibility and is defined as:

$$\frac{C}{V} = \frac{\Delta V/V}{\Delta P} \tag{2.12}$$

The bulk modulus is obtained by dividing the average normal stress $\sigma = {}^{1}/_{3}(\sigma_\theta + \sigma_L + \sigma_R)$ by volumetric strain [100]. Alternatively, the bulk modulus is the normalized elastance and is calculated by:

$$El \cdot V = \frac{\Delta P}{{}^{\Delta V}/_{V}} \tag{2.13}$$

The Windkessel model describes the artery in terms of compliance and resistance. First, Frank Windkessel formulated the two-element Windkessel model consisting of a compliance (C) and a resistance element (R), and later the third element was added, the characteristic impedance (Z_c). The peripheral resistance (R) is defined as [101]:

$$R \approx \frac{P_{mean}}{CO} \tag{2.14}$$

where P_{mean} the mean aortic pressure and *CO* the cardiac output, the volume of blood pump by heart in a minute.

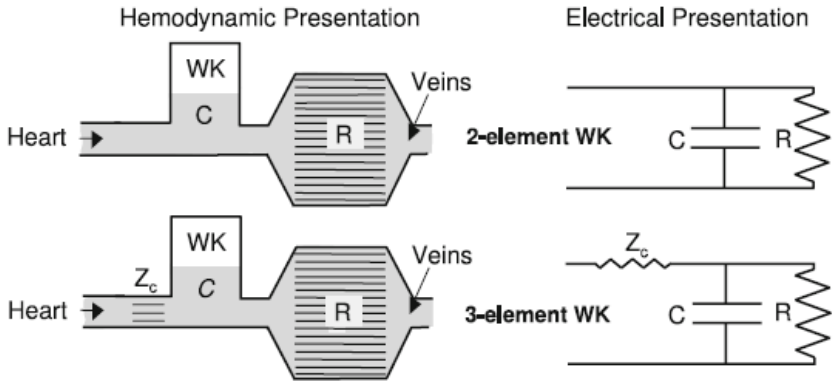

Figure 9: The two and the three-element Windkessel model in hydraulic and electrical representations (From [101] without permission).

2.2.3.2 The Common Carotid Artery

The principal arteries for blood supply to the head and neck are the two common carotid arteries (CCAs), the right carotid and the left artery. Each CCA ascends in the neck and is divided into two branches, the external carotid artery (ECA) and the internal carotid artery (ICA). The ECA supplies the exterior of the head, the face and the greater part of the neck with blood, and ICA is to a great extent responsible for supplying the parts within the cranial and the orbital cavities. The structure of CB is unique at the root

of ICA which is enlarged and known as the carotid sinus or carotid bulb. The root of ICA can be assumed as the origin of cerebral circulation as the ICA has no other branches until just before the circle of Willis (exception the ophthalmic artery) [102]. Based on a sample of 74 human specimens, the shape of the carotid bifurcation approximates the tuning-fork shape model better than the Y-shape [103]. Seong *et al.* found that the morphological development of human CB is age-dependent and more specifically that the substantial growth of ICA is related to age. Furthermore, they found that the development of the carotid sinus at the origin of ICA occurred during late adolescence. Finally, they concluded that the bifurcation angle remains unchanged from infancy to adulthood [102]. The position of the right CB [81] is represented in Fig. 10.

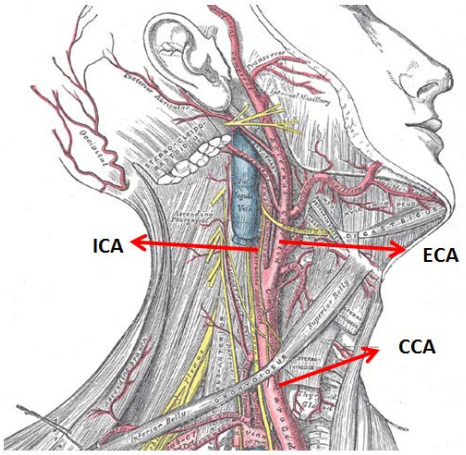

Figure 10: The Right Carotid Bifurcation with CCA, ECA and ICA (from [81] without permission).

2.2.4 The Blood

Blood is the transport medium which carries oxygen and nutrients to metabolically active tissue, returns carbon dioxide to the lungs, and delivers metabolic end-products to the kidneys. The blood is a complex, heterogeneous suspension of formed elements, the blood cells, or hematocytes, suspended in a continuous, straw-yellow colored fluid called plasma. Blood accounts for about 8±1 % of total body weight, averaging 5200 ml and has a mass density 1.057±0.007 g/cm^3. The hematocytes include three basic types of cells: a) Red Blood Cells (RBC, erythrocytes, totaling nearly 95 % of the formed elements), b) White Blood Cells (WBC, leukocytes, averaging <0.15 % of all hematocytes) and c) Platelets (thrombocytes, on the order of 5 % of all blood cells). The characteristics of blood cells are shown in Table 3. The primary

function of erythrocytes is to aid in the transport of blood gases, of leukocytes is to endow the human body with the ability to identify and dispose of foreign substances and of platelets is to participate in the blood clotting process [82]. The blood distribution in the different blood vessels was represented above in Fig. 6B.

The number of RBC is relatively much bigger compared with the number of Platelets and WBC, consequently the mechanical behavior of the formed elements is dominated by the RBC, in large vessels. The volume fraction of RBC is an important index for the rheological and physiological characteristics of blood and is known as the hematocrit (Ht), and defined by [83]:

$$Ht = \frac{Volume\ of\ RBC}{Total\ Blood\ Volume} \tag{2.15}$$

Table 3: The hematocytes include three basic types of cells: RBC, WBC and Platelets (from [84] without permission).

Cell Type	Number Cells per mm³ Blood*	Corpuscular Diameter (μm)*	Corpuscular Surface Area (μm²)*	Corpuscular Volume (μm³)*	Mass Density (g/cm³)*	Percent Water*	Percent Protein *	Percent Extractives*†
Erythrocytes	4.2–5.4	6–9 (7.5)	120–163	80–100	1.089–1.100	64–68	29–35	1.6–2.8
(red blood cells)	× 10⁶ ♀	Thickness	(140)	(90)	(1.098)	(66)	(32)	(2)
	4.6–6.2	1.84–2.84						
	× 10⁶ ♂	"Neck"						
	(5 × 10⁶)	0.81–1.44						
Leukocytes	4000–11000	6–10	300–625	160–450	1.055–1.085	52–60	30–36	4–18
(white blood cells)	(7500)					(56)	(33)	(11)
Granulocytes								
Neutrophils:	2–6 × 10³	8–8.6	422–511	268–333	1.075–1.085	—	—	—
55–70% WBC (65%)	(4875)	(8.3)	(467)	(300)	(1.080)			
Eosinophils:	45–480	8–9	422–560	268–382	1.075–1.085	—	—	—
1–4% WBC (3%)	(225)	(8.5)	(491)	(321)	(1.080)			
Basophils:	0–113	7.7–8.5	391–500	239–321	1.075–1.085	—	—	—
0–1.5% WBC (1%)	(75)	(8.1)	(445)	(278)	(1.080)			
Agranulocytes								
Lymphocytes:	1000–4800	6.75–7.34	300–372	161–207	1.055–1.070	—	—	—
20–35% WBC (25%)	(1875)	(7.06)	(336)	(184)	(1.063)			
Monocytes:	100–800	9–9.5	534–624	382–449	1.055–1.070	—	—	—
3–8% WBC (6%)	(450)	(9.25)	(579)	(414)	(1.063)			
Thrombocytes	(1.4 ♂),	2–4 (3)	16–35	5–10	1.04–1.06	60–68	32–40	Neg.
(platelets)	2.14 (♀)–5	Thickness	(25)	(7.5)	(1.05)	(64)	(36)	
(2.675 × 10⁵)	×10⁵	0.9–1.3						

*Normal physiologic range, with "typical" value in parentheses.
†Extractives include mostly minerals (ash), carbohydrates, and fats (lipids).

2.3 Vascular Diseases

The cardiovascular diseases are divided broadly into two major categories, a) those which are related to heart failure, congenital and coronary heart diseases; and b) those that will be summarized in this paragraph, and are related to blood vessel abnormalities such as atherosclerosis, aneurysm, thrombosis and stroke [80]. For the initiation of the vascular diseases, the endothelium layer plays an important role, as it is the structure

that is in constant contact with blood flow [78]. The wall thickness of vessels, is regulated to maintain the circumferential wall shear near a target value. Some pathology conditions related with the endothelium layer inside the blood vessels are: a) the hypertrophy; b) the hyperplasia; c) the apoptosis; and d) the migration; each involved in diseases such as atherosclerosis, aneurysms and hypertension [78]. The main techniques that are followed for treatment of peripheral artery diseases are: a) angioplasty and stenting; b) endarterectomy; and c) bypass grafting [104].

2.3.1 Atherosclerosis

Atherosclerosis is a chronic, progressive, vascular disorder caused by the weakness of the arterial wall and characterized by gradual narrowing and finally occlusion of the blood vessel. The process consists of the formation of fibrofatty and fibrous lesions that lead to inflammation [22, 24]. The chronic accumulation of fatty material within the intimal layer, cause also an increase in the wall stiffness (or a decrease in compliance) of the vessel. One of the essential causes of the plaque genesis and development may be the anomalous enlargement of the intima by infiltration and accumulation of macromolecules like lipoproteins [80]. The composition of plaque plays a crucial role for its own rupture that may cause myocardial infraction, peripheral vascular diseases and ischemic events [105, 106]. In more detail, a plaque with a thin fibrous cap and a large lipid core is more prone to rupture. The composition of atherosclerotic plaque consists of: a) the fibrous cap, composed of smooth muscle cells and fibrotic tissue; b) the lipid-rich necrotic core, composed by fat-laden macrophages and extracellular lipids; c) the calcification; and d) the hemorrhage or thrombus [107, 108].

2.3.2 Aneurysm

Aneurysm refers to the abnormal dilatation of the arterial wall as the result of its weakness or thinning. Aneurysms usually occurs in arteries and the two most common types are the intracranial saccular aneurysms and abdominal aortic aneurysms (AAA) [78, 109]. Two mechanisms involved in aneurysm growth are: a) the WSS-driven apoptotic behavior of endothelium cells, leading to loss of vascular tone which is

important for the initiation of aneurysm growth; and b) the arterial wall remodeling [110]. Meng *et al*. suggested that a combination of high WSS and high WSSSG constitutes a dangerous hemodynamic condition that predisposes the vessel wall to aneurysm formation [111, 112].

2.3.3 Stroke

Stroke is the blockage of an artery that supplies blood to the brain. The classification of stroke consists of ischemic stroke (thrombosis, embolic, etc.) and hemorrhage. The thrombotic stroke is the most common type of stroke (referred to extensively in the next paragraph); and the embolic stroke which is the least common type, and occurs when the blood clot travels to the brain from the heart or other vessels. The intracranial hemorrhagic stroke happens when an artery leaks or bursts and the result is the interruption of the brain's blood supply [113].

2.3.4 Thrombosis

Thrombosis refers to blood clotting, the situation of the aggregation of blood substances. Thrombus, the blood clot, may form on implanted devices like stents and/or ruptured atherosclerotic plaques, from where it can be detached and travel in flowing blood into smaller-diameter vessels, where it eventually lodges. The highest WSS was found at the CB in a CFD model by Brown *et al*. and their results showed that the stresses may reach the rupture value [114]. The lodged clots cause distal ischemia such as stroke, pulmonary embolism, heart attack, and in the case of cerebral aneurysms, cause cerebral vasospasm [78].

Chapter 3:

Blood Flow Dynamics

3.1 Overview

Blood, as already described in paragraph 2.2.4, is a complex fluid comprised by cells and plasma. Fluid refers to the liquid and gas state of matter. The third distinct state of matter is the solid state. The distinction between fluid and solid lies with the corresponding response to an applied shear or tangential stress. Solids resist to shear stress by a static deformation in contrast with fluids, which no matter how small the shear stress applied on them is, move and experience a continuous deformation [115]. The elements of a fluid in motion can move in different directions and velocities, however, these elements are not separated. Fluid elements in continuous deformation result in the velocity gradients [116]. The velocity gradients may occur in all directions and comprise the flow field. There are two ways to view and analyze the velocity field within a fluid: a) the Lagrangian method, which follows an individual particle moving through the flow; and b) the Eulerian method, which is based on calculations of properties in specific positions within the fluid [115, 116].

3.2 Blood Characteristics

3.2.1 Viscosity

The viscous force is a force exerted by a fluid as a resistance to flow. The dynamic viscosity is the degree to which a fluid resists flow under an applied force, measured by the tangential friction force per unit area divided by the velocity gradient, under conditions of streamline flow. Generally, when the force is proportional to the velocity gradient, the fluid is known as Newtonian, as he was the first observe this relation. The local shear stress (τ) is calculated [117] by:

$$\tau = \mu \frac{du}{dy} \tag{3.1}$$

where μ is the dynamic viscosity and $\frac{du}{dy} = \dot{\gamma}$ the rate of shear.

The units of shear rate is 1/s and viscosity's is Pa·s=Ns/m^2, or Poise (dynes·s/cm^2), with 1 Pa·s=10 Poise. Viscosity is sometimes called dynamic viscosity in contrast to the kinematic viscosity, which is defined as viscosity divided by density (μ/ρ) [99].

The viscosity of blood depends on the viscosity of plasma in combination with the hematocrit and red cell deformability. One of the simplest relations between viscosity and hematocrit is called Einstein's equation and is defined $\mu = \mu_{plasma}(1 + 2.5Ht)$. The viscosity of plasma is about 0.0015 Poise (1.5 centipoise, cP) and the viscosity of blood at physiological hematocrit (40-45%) is about 3.2 cP [83, 99].

3.2.2 Blood Pressure

Blood pressure refers to force exerted by the blood against any unit area of the vessel wall and is almost always measured in millimeters of mercury (mmHg). At a vessel pressure of 50 mmHg, the force exerted is sufficient to push a column of mercury against gravity up to a level 50 mm high. Normal blood pressures in various artery types are represented in Fig. 11.

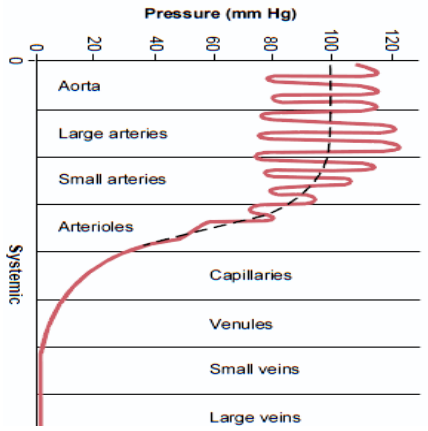

Figure 11: Normal blood pressures in the different artery types (from [82] without permission).

3.3 Blood Flow

As mentioned above, the heart acts as a pump and generates pressure and flow waves to drive blood through the blood vessels network, to the furthest extremes of the organism. Because of the elasticity of the aorta and the major conduit arteries, the pressure and flow waves are not transmitted instantaneously to the periphery, but they propagate through the arterial tree with a certain speed, called wave speed or pulse wave velocity. For simplicity's sake, let us assume that blood vessels are straight, stiff

and uniform and the flow is steady. From fluid mechanics, Poiseuille's law relates the pressure differences (ΔP) and the steady flow (Q) through a rigid tube (Fig. 12) by:

$$Q = \frac{\Delta P}{R} \tag{3.2}$$

where: Q: Flow rate (m^3/s)
ΔP: Pressure difference (mmHg)
R: Resistance ($mmHg \cdot s/m^3$)

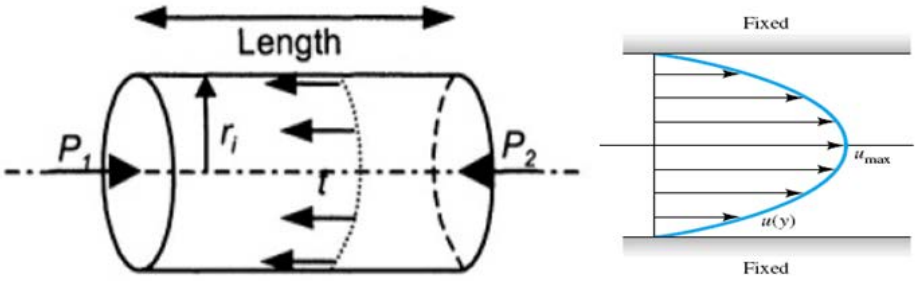

Figure 12: Blood flow in a tube (Left) [99] and the parabolic velocity profile for incompressible viscous flow (Right)[115].

Flows and related phenomena can be described by partial differential (or integro-differential) equations, which cannot be solved analytically except in special cases. To obtain an approximate solution numerically, it is necessary the use of a discretization method which approximates the differential equations by a system of algebraic equations, which can then be solved using a computer. The approximations are applied to small domains in space and/or time so the numerical solution provides results at discrete locations in space and time.

Blood flows in the artery system are a complex problem which cannot be solved using any analytical method so the use of numerical solution methods (CFD) is enforced, as mentioned earlier. The components of a numerical solution method are [118]:

a) **Mathematical Model**, the set of partial differential or integro-differential equations and boundary conditions.

b) **Discretization Method**, the method of approximating the differential equations by a system of algebraic equations for the variables at some set of discrete locations in space and time. The most important are: finite difference (FAM), finite volume (FVM), and finite element method (FEM).

c) **Coordinate and Basis Vector Systems**, the conservation equations can be written in many different forms, depending on the coordinate system and the basis vectors used.

d) **Numerical Grid**, which is a discrete representation of the geometric domain on which the problem is to be solved. It divides the solution domain into a finite numbers of subdomains. Some of the grid options available are: 1) The Structured Grid; 2) The Block-Structured Grid; and 3) The Unstructured Grid.

e) **Finite Approximations**, following the choice of grid type, one has to select the approximations to be used in the discretization process.

f) **Solution Method**, discretization yields a large system of non-linear algebraic equations and the method of solution depends on the problem.

g) **Convergence Criteria**, finally one needs to set the convergence criteria for the iterative method.

3.4 Governing Equations

Throughout the study, the blood is assumed to be an incompressible Newtonian fluid, and its density will remain constant. These assumptions simplify the governing equations. Conservation laws can be derived by considering a given quantity of matter or control mass (CM) and the extensive properties obtained there, such as mass, momentum and energy. This approach is used to study the dynamics of solid bodies, where the CM system is easily identified. In fluid flows it is more convenient to work with the control volume (CV), instead of following a parcel of matter which quickly passes through the region of interest. This method of analysis is called the control volume approach. To convert to a CV analysis, mathematical relations have to be adjusted in order to be applied to a specific region rather than to individual masses. This conversion called the Reynolds Transport Theorem, and can be applied to all fundamental laws. Reynolds Transport Theorem is expressed as [118]:

$$\frac{d}{dt}\int_{\Omega_{CM}} \rho\varphi d\Omega = \frac{d}{dt}\int_{\Omega_{CV}} \rho\varphi d\Omega + \frac{d}{dt}\int_{S_{CV}} \rho\varphi(\boldsymbol{v}-\boldsymbol{v_b})\cdot\boldsymbol{n}dS \tag{3.3}$$

where: Ω_{CM} is the CV

S_{CV} is the surface enclosing CV
φ is any conserved intensive property
ρ is density (mass per unit volume)
n is the unit vector orthogonal to S_{CV} and directed outwards
υ is the fluid velocity
and **υ_b** is the velocity which CV surface is moving (υ_b=0 for fixed CV)

The conservation law for an extensive property relates the rate of change of the amount of that property in a given CM to externally determined effects. For mass, which is neither created nor destroyed in the flows of engineering interest, the conservation equation can be written:

$$\frac{dm}{dt} = 0 \tag{3.4}$$

The conversation of momentum is given by Newton's second law of motion:

$$\frac{d(mu)}{dt} = \sum \boldsymbol{f} \tag{3.5}$$

where: *m* stands for mass, *u* for velocity, and $\boldsymbol{f}$ for forces acting on the CM

3.4.1 Mass Conservation (Continuity)

The conservation of mass states that the net rate of mass flux through the control surfaces should be equal to the rate of mass accumulation within the CV. The integral form of the mass conservation equation follows directly from (2.3) by setting φ =1:

$$\frac{\partial}{\partial t}\int_{\Omega} \rho d\Omega + \int_{S} \rho \boldsymbol{v} \cdot \boldsymbol{n} dS = 0 \tag{3.6}$$

The first part is the rate of mass accumulation and the second the rate of mass flux. The equation (2.6) can be written in differential formulations as:

$$\frac{\partial \rho}{\partial t} + \nabla \cdot (\rho \boldsymbol{v}) = 0 \tag{3.7}$$

where ∇ called nabla, is the divergence (div) function

$$\nabla \cdot \overline{\boldsymbol{S}} = \frac{\partial u}{\partial x} + \frac{\partial v}{\partial y} + \frac{\partial w}{\partial z} \tag{3.8}$$

where $\overline{\boldsymbol{S}}$ a continuous differentiable vector $\overline{\boldsymbol{S}} = u\boldsymbol{i} + v\boldsymbol{j} + w\boldsymbol{K}$

For steady, incompressible flow the equation (2.7) is reduced to:

$$\nabla \cdot \boldsymbol{v} = 0 \tag{3.9}$$

3.4.2 Momentum Conservation

The conservation of mass states that the sum of the net rate of momentum flux through the control surface and the rate of momentum change within the CV, is equal to all applied forces on the system. The integral form of the momentum conservation equation follows from equations (3.3) and (3.5) by setting φ =**υ** for a fixed containing volume of space:

$$\frac{\partial}{\partial t}\int_{\Omega} \rho \boldsymbol{v} d\Omega + \int_{S} \rho \boldsymbol{v}\boldsymbol{v} \cdot \boldsymbol{n} dS = \sum \boldsymbol{f} \tag{3.10}$$

The first part is the rate of momentum accumulation, and the second the rate of momentum flux.

To express the right hand side in terms of intensive properties, one has to consider the forces which may act on the fluid in a CV:

a) Surface forces (pressure, normal and shear stresses, surface tension etc.)
b) Body forces (gravity, centrifugal and Coriolis forces, electromagnetic forces etc.)

For Newtonian fluids, the stress tensor **T**, which is the molecular rate of transport of momentum, can be written as:

$$\boldsymbol{T} = -\left(P + \frac{2}{3}\mu \nabla \cdot \boldsymbol{v}\right)\boldsymbol{I} + 2\mu \boldsymbol{D} \tag{3.11}$$

where μ is the dynamic viscosity
I is the unit tensor
P is the static pressure
and **D** is the rate of strain (deformation) tensor which is given by:

$$\boldsymbol{D} = \frac{1}{2}[\nabla \boldsymbol{\upsilon} + (\nabla \boldsymbol{\upsilon})^{\mathrm{T}}] \tag{3.12}$$

With the body forces (per unit mass) being represented by **b**, the integral form of the momentum conservation equation becomes:

$$\frac{\partial}{\partial t}\int_{\Omega} \rho \boldsymbol{v} d\Omega + \int_{S} \rho \boldsymbol{v}\boldsymbol{v} \cdot \boldsymbol{n} dS = \int_{S} \boldsymbol{T} \cdot \boldsymbol{n} dS + \int_{\Omega} \rho \boldsymbol{b} d\Omega \tag{3.13}$$

A coordinate free vector form of the momentum conservation equation (3.11) is obtained by applying Gauss divergence theorem to the convective and diffusive flux terms:

$$\frac{\partial(\rho \boldsymbol{v})}{\partial t} + \nabla \cdot (\rho \boldsymbol{v}\boldsymbol{v}) = \nabla \cdot \boldsymbol{T} + \rho \boldsymbol{b} \tag{3.14}$$

3.5 Types of Flow

The conservation equations are non-linear, coupled, and difficult to solve, so in many cases the equations of motion can be simplified. Some important types of flow are reported below:

1. **Incompressible Flow**

   In this case we assume the fluid density remains constant and the compressibility is neglected. This flow is true for liquids mainly, but also stands for gases with Mach (Ma) number below 0.3.

2. **Compressible Flow**

   The compressible flows can be listed regarded the Mach number.

   0.3 < MA < 0.8 subsonic flow

   0.8 < Ma < 1.2 transonic flow

   1.2 < Ma < 3.0 supersonic flow

   3.0 < Ma hypesonic

3. **Inviscid Flow (Euler)**

   When the viscous effects are neglected, the Navier-Stokes equations are reduced to the Euler equations. The no-slip condition cannot be assumed here.

4. **Creeping Flow (Stokes)**

   For very small velocities and the fluid is very viscous.

3.6 Hemodynamic Parameters Related to the Development of Atherosclerosis

The endothelial cells are sensors of WSS and responded to abnormal WSS values by trying to regulate vessel caliber and structure to achieve normal WSS. The chronicle abnormal WSS may lead to vessel remodeling, and help for the initiation and the

development of vascular pathologies [119]. For that reason many researchers have suggested the use of a variety of hemodynamic quantities such as WSS, TAWSS, WSSTG, WSSSG, OSI, nOSI, and RRT as potential markers to quantify the disturbance of blood flow. Furthermore, Himburg *et al.* suggested that the frequency content of the WSS exposure may be a contributing factor in lesion development [120, 121]. These parameters may be used to predict areas vulnerable to atherogenesis. They may also be used as indicators of abnormal flow and concerned to deteriorate the vascular dysfunction [122]. The more significant indicators recommended over the years and calculated in this study are presented below.

3.6.1 Wall Shear Stress (WSS)

As already mentioned, fluid shear stress play a key role in atherogenesis and the atherosclerotic development. Zhao *et al.* found a considerable overlap of regions of low WSS and high mechanical stress, areas that correspond to regions favorable to atherosclerosis develop and also the TAWSS in the range 0.5 - 1.69 Pa [123]. From literature for endothelium function the physiological WSS values are 1.5 -2 Pa and high WSS > 5 Pa [44]. Reneman *et al.* concentered from several studies the mean WSS levels in the CCA for healthy individuals and presented a range of 0.9 - 1.6 Pa [17].

The pulsatile blood flow inside arteries produced hemodynamic forces acting on the arterial walls that alter cell physiology. The WSS is exerted in the direction of the flow (longitudinal) and the normal stress (radial direction, pressure) in the direction perpendicular of the blood flow. The arterial wall also suffers from strains due the developed stress. The magnitude of longitudinal motion is negligibly small compared with the radial motion but has recently become highly significant and should be taken into account in the solution of the solid mechanics problem of the thick arterial wall [124].

There are several methods to calculate WSS in arteries, and the most important will be presented below. Firstly, if blood is considered as an incompressible, Newtonian fluid,

then the magnitude of WSS, which depends on the dynamic viscosity of the blood (μ) and the velocity gradient near the arterial wall, is defined as [125]:

$$WSS = \tau_w = \mu \frac{\partial u}{\partial y} = \mu\, \dot{\gamma} \tag{3.15}$$

where $\dot{\gamma}$ is the wall shear rate (s^{-1})

The generalization of eq. (3.15) to 3D flow results in the viscous-stress tensor acting on a volume element, presented as:

$$\tau_{ij} = \begin{bmatrix} \tau_{xx} & \tau_{yx} & \tau_{zx} \\ \tau_{zy} & \tau_{yy} & \tau_{zy} \\ \tau_{xz} & \tau_{yz} & \tau_{zz} \end{bmatrix} \tag{3.16}$$

where the shear stress components acting on the x,y, and z-direction faces are defined:

$$\tau_{xx} = 2\mu \frac{\partial u}{\partial x}, \quad \tau_{xx} = 2\mu \frac{\partial v}{dy}, \quad \tau_{xx} = 2\mu \frac{\partial w}{\partial z}$$

$$\tau_{xy} = \tau_{yx} = \mu \left(\frac{\partial u}{\partial y} + \frac{\partial v}{\partial x}\right), \quad \tau_{xz} = \tau_{zx} = \mu \left(\frac{\partial w}{\partial x} + \frac{\partial u}{\partial z}\right), \quad \tau_{yz} = \tau_{zy} = \mu \left(\frac{\partial v}{\partial z} + \frac{\partial w}{\partial y}\right) \tag{3.17}$$

The WSS is measured in pressure units, $1 \frac{N}{m^2} = 10 \frac{dyn}{cm^2}$. Furthermore, in the case of Poiseuille flow which again the fluid is considered as Newtonian and the flow is under steady conditions, fully developed and the walls are rigid, the WSS is defined as [126]:

$$\tau_w = \frac{4\mu Q}{\pi r^3} = \frac{4\mu u_m}{\pi r} \tag{3.18}$$

where *Q* is the blood volume flow and u_m the mean velocity.

Using the information from PC-MRI the systolic WSS can be calculated by [125]:

$$\tau_w = \frac{4\mu u_m}{r} = \frac{2\mu u_{max}}{r} \tag{3.19}$$

Another method using PC-MRI and equation (2.15) is described by [127] and requires two velocity measurements, one at, and the other near the arterial wall. This linear method uses the approximation from the two locations to calculate the ratio $\frac{du}{dr}$, and by knowing the blood viscosity it is possible to estimate the WSS. Using the same direct method, Gelgand *et al.* confirmed the existence of significant spatial heterogeneity in CB and indicated that the time and frequency dependent parameters of WSS have

significant implications for the regional development of atherosclerosis [128]. In a study of Papathanasopoulou *et al.* it was found that the direct calculation of time-averaged WSS from PC-MRI is in good agreement with CFD in regions of low WSS but in regions of complex flow, a combination of MR and CFD is necessary [62]. A recent study showed the accuracy of a very fast method to calculate the WSS in CB, the spiral Fourier velocity encoded MRI [129]. Although the pulse Doppler sonography technique is used routinely, it will not be discussed. A review study of Shaaban and Duerinckx concluded that despite the differences in the WSS calculations, the most commonly used methods are in great agreement. They also stated that WSS is subject-specific and vessel-specific [130].

3.6.2 Time Averaged WSS (TAWSS)

The TAWSS is calculated by the integration of WSS over the cardiac cycle and defined by [122]:

$$TAWSS = \frac{1}{T}\int_0^T |\tau_w| dt \tag{3.20}$$

Wu *et al.* in a study of 20 volunteers found that the highest and lowest WSS (mean, max, min: 0.83, 2.37, and 0.29 Pa) developed in CCA in comparison with femoral and brachial arteries [131]. The values are calculated using μ=2.5 cP because the values from their study are wall shear rate. Many studies found relative values for WSS, for example: a) Samijo *et al.* found mean WSS ~1.3 Pa and peak WSS ~3.3 Pa for male age 20-50 years old (n=56) [132]; and b) Oyre *et al.* found mean WSS 0.95 Pa and peak WSS 2.56 Pa (n=7) [133].

3.6.3 WSS Temporal Gradient (WSSTG)

The cycle averaged magnitude of the time derivative of the instantaneous WWS, first defined by Ojha [134], was calculated by integrating the absolute rate of change in WSS magnitude over the cardiac cycle [135]:

$$WSSTG = \frac{1}{T}\int_0^T \left|\frac{\partial \tau_w}{\partial t}\right| dt \tag{3.21}$$

3.6.4 WSS Spatial Gradient (WSSSG)

This marker of endothelium cells tension was introduced by Kei and Truskey [136] and is calculated from the WSS gradient components as found in [122, 137]:

$$WSSSG = \frac{1}{T}\int_0^T \sqrt{\left(\frac{\partial \tau_{w,m}}{\partial m}\right)^2 + \left(\frac{\partial \tau_{w,n}}{\partial n}\right)^2}\, dt \tag{3.20}$$

where *m* indicates the direction of TAWSS vector and *n* the perpendicular to *m* on the surface

The high sustained WSSSG could be correlated with susceptible sites of restenosis, hyperplasia and atherogenesis [137, 138].

3.6.5 Oscillatory Shear Index (OSI)

The OSI shows the degree of direction change in WSS throughout the cardiac cycle. It was first defined by ku et al. [15]:

$$OSI = \frac{1}{2}\left(1 - \frac{|\int_0^T \tau_w dt|}{\int_0^T |\tau_w|}dt\right), 0 < OSI < \frac{1}{2} \tag{3.21}$$

An OSI value of 0 corresponds to unidirectional shear flow, whilst 0.5 corresponds to a purely oscillatory shear. In this study, the modified OSI by Papaharilaou *et al.* was used [139]:

$$OSI = \frac{\int_0^T w|\tau_w \cdot \boldsymbol{n_m}|dt}{\int_0^T |\tau_w \cdot \boldsymbol{n_m}|dt},\ 0 <\ OSI < 1/2 \tag{3.22}$$

$$n_m = \frac{1}{T}\int_0^T \left(\frac{\boldsymbol{\tau}}{\|\boldsymbol{\tau}\|}\right) dt \tag{3.23}$$

where T is the heart cycle period, $\boldsymbol{\tau}$ is the instantaneous WSS vector, $\boldsymbol{n_m}$ is the mean shear direction and *w* is defined according to

$$w = 0.5(1 - cosa) \tag{3.24}$$

where α is the angle between $\boldsymbol{\tau}$ and $\boldsymbol{n_m}$.

3.6.6 Normalized OSI (nOSI)

The nOSI is calculated by dividing OSI with the TAWSS magnitude normalized by the time-averaged inlet Poiseuille flow as represented below:

$$nOSI = \frac{OSI}{TAWSS/WSS_{Poiseuille}} \tag{3.25}$$

where $WSS_{Poiseulle}$ is the Poiseulle flow WSS at the inlet.

3.6.7 Relative Residence Time (RRT)

The RRT was proposed by Himburg et al. [140] and is defined as:

$$RRT = \frac{1}{(1-2\cdot OSI)\cdot TAWSS} \tag{3.26}$$

This indicator was recommended and used extensively as it combines the low and oscillating shear and identifies the possible regions of atheromatic concentrations [36, 37, 122]. An earlier study showed that regions of flow recirculation like carotid sinus, corresponds to longer particle residence times within the bifurcation [141].

3.6.8 Helicity (H)

Helicity is the property of moving fluid that represents the potential for helical flow and is proportional to the strength and the amount of the vorticity [142]. Helicity has great influence on the evolution and stability of laminar and turbulent flows. The helical flow is the only hemodynamic parameter represented here, and can possibly play a key role in preventing plaque deposition and intimal thickening [142]. Helicity (H) was introduced by Moffat and Tsinober [143] nd for a fluid in a domain *D* defined by:

$$H(t) = \int_D v(x,t)\cdot\nabla\times v(x,t)dV = \int_D v(x,t)\cdot\omega(x,t)dV \tag{3.27}$$

where $\omega = \nabla\times v$ is the vorticity field of the flow.

Helicity density is the quantity:

$$H_k = \int v(x,t)\cdot\omega(x,t)dV \tag{3.28}$$

The quantity Localized Normilized Helicity (LNH) used in this study defined as in [144, 145]:

$$LNH(x,t) = \frac{v(x,t)\cdot\omega(x,t)}{|v(x,t)||\omega(x,t)|}, -1 \leq LNH \leq 1 \quad (3.29)$$

The positive values of helicity are related to clockwise rotation and negative ones to counterclockwise blood rotation.

A new hemodynamic parameter proposed by Shimogonya *et al*. is the gradient oscillatory number (GON), defined [146] by:

$$GON = 1 - \frac{\left|\int_0^T \boldsymbol{G}\, dt\right|}{\int_0^T |\boldsymbol{G}| dt}, 0 \leq GON \leq 1 \quad (3.30)$$

where T is the heart cycle period and **G** the WSSSG.

Chapter 4:

Magnetic Resonance

4.1 Introduction and Brief History of MR

The Magnetic Resonance Imaging (MRI) is a modern imaging technique which is primarily used in radiology to image the human body for medical purposes. In magnetic resonance the nucleuses which are used for imaging are the hydrogen atoms through the high water percentage which exists in biological organisms. Magnetic resonance techniques provide images in great detail from any layer and any slice of the body. Concerning soft tissues, it provides much greater contrast compared to Computer Tomography (CT), making this modality more useful for the cardiovascular, neurological, musculoskeletal systems, and oncological imaging. Unlike CT and X-ray techniques, magnetic resonance does not use any harmful radiation and for this reason it has become a popular noninvasive imaging technique for normal and pathology measurements for alive organisms [147].

Magnetic resonance imaging is based on the phenomenon of nucleus magnetic resonance which was originally independently described by Bloch and Purcell in 1946. The imaging technique development was first introduced in 1974 by Lauterbur [148] and Grannel and Mabsield [149]. This was based on resonance frequency shift which arises with the enforcement of a magnetic field. The first images were limited in small objects and the first image from the whole body was published in 1977 by Damadian *et al*. [150].

Over the years, fast methods for data acquisition and processing to reduce the imaging time were developed. Also, new methods were developed for water and fat separation in proton images and other techniques for the *in vivo* blood flow measurements. With the MRI diagnosis technique, direct three-dimensional imaging of the anatomical structure is possible. This is only accomplished by the assemblage of multiple slices and the use of suitably reconstruction techniques.

4.2 The Classical View of MR

The classical approach uses the vector of total magnetization **M**, from the total spin of hydrogen nucleus of biological tissues and organs. The MR imaging is based on the

selective excitation of magnetic dipoles of the atoms of the nucleus that compose the examined biological material. The excited nucleus reradiates a radiofrequency signal, which is detected and recorded with the resonance radiofrequency coils at the frequency that the nucleuses spin (or the Larmor frequency). Excitation selectivity is achieved by means of static magnetic field gradients, so that the momentum intension varies linearly with the vector direction. Radiofrequency transmitter is responsible for nucleus excitation. The signal intensity fluctuation received by the receptor is a consequence of nucleus density. With the scanning of the resonance region in the 3D space and the recording of the received intensity signal, the imaging of the nucleus density and even of other factors that relate to the nucleus excitation is achieved.

The basic concept of MRI is based in the interaction between hydrogen nucleus spin of the specimen (biological tissue) and the strength of the external magnetic field **(B)**. Even though this interaction is governed by quantum mechanics principles, for the macroscopic approach it can be well described by the classic mechanics principles. In the presence of an external magnetic field **B**, the magnetization **M**, which is the sum of all spin vectors of a nucleus volume, will experience a torque **T** given by:

$$\boldsymbol{T} = \frac{d\boldsymbol{J}}{dt} = \boldsymbol{M} \times \boldsymbol{B} \tag{4.1}$$

$$\boldsymbol{M} = \gamma \cdot \boldsymbol{J} \tag{4.2}$$

where **J** is the angular momentum and γ is the gyroscopic constant.

The motion equation of the magnetization vector is the Bloch equation:

$$\frac{d\boldsymbol{M}}{dt} = \boldsymbol{M} \times \gamma \boldsymbol{B} \tag{4.3}$$

The Bloch equation in a generalized form for time varying magnetic field is given by:

$$\frac{d\boldsymbol{M}(t)}{dt} = \boldsymbol{M}(t) \times \gamma \boldsymbol{B}(t) - \boldsymbol{R}\{\boldsymbol{M}(t) - \boldsymbol{M}_o\} \tag{4.4}$$

where $\mathbf{M_o}$ the initial magnetization

The Larmor frequency $\omega_o = -\gamma \boldsymbol{B}_o$ defined from the frequency of the magnetic field function.

$$\omega(t) = -\gamma \mathbf{B}(t), \quad \mathbf{M}_0 = \begin{pmatrix} 0 \\ 0 \\ M_0 \end{pmatrix} \tag{4.5}$$

R the relaxation matrix:

$$\mathbf{R} = \begin{pmatrix} \frac{1}{T_2} & 0 & 0 \\ 0 & \frac{1}{T_2} & 0 \\ 0 & 0 & \frac{1}{T_1} \end{pmatrix} \tag{4.6}$$

Substituting the above equations into the Bloch equation for the laboratory reference system gives:

$$\frac{d\mathbf{M}(t)}{dt} = \mathbf{M}(t) \times \gamma \mathbf{B}(t) - \frac{1}{T_2}\left\{M_x \mathbf{i} + M_y \mathbf{j}\right\} - \frac{1}{T_1}\left\{M_z - M_0\right\}\mathbf{k} \tag{4.7}$$

4.3 Basic Instrumentation of MRI

MRI consists of the following basic components (Fig. 13):

a) The main magnet which produces the static magnet field, (0.5 – 11 Tesla). Most modern systems employ a superconductor to reduce energy consumption and to maintain high magnetic fields.

b) Three gradient coils system for frequency and phase encoding in space.

c) Radiofrequency (RF) coils for excitation and signal reception from the resonance nucleus of the examined tissues.

d) The imaging system that includes a computer where the reconstruction and image presentation are performed.

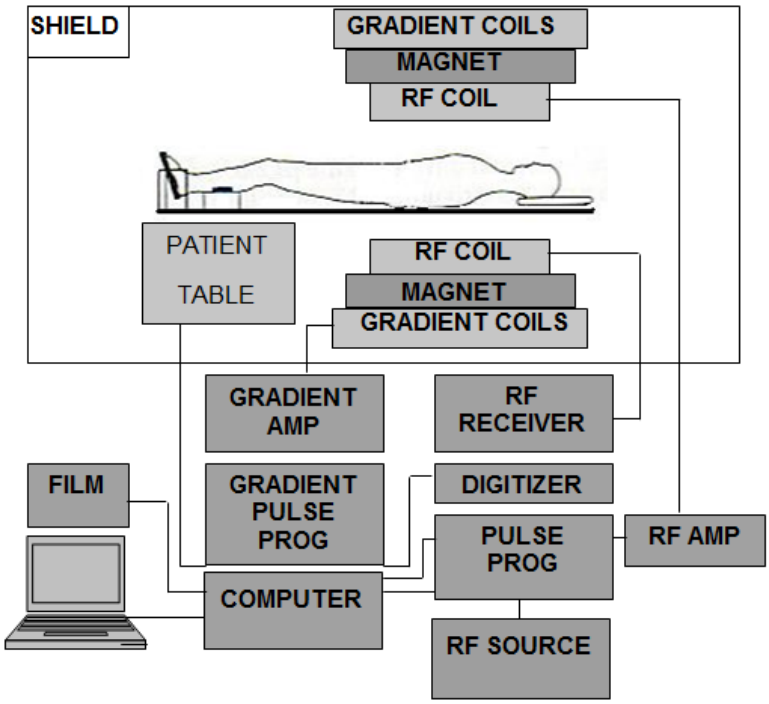

Figure 13: A schematic representation of all MRI components (from [151] without permission)

4.4 Data Acquisition, Reproduction, and Storage of MR Images

4.4.1 Pulse Sequences

Pulse sequences are the time-spatial gradient timing sequences that allow manipulation of the magnetization vector, sampling of k-space and image formation. Different types allow different contrast based on T_1, T_2, T_2*, flow, diffusion, perfusion, motion, with imaging times that range from milliseconds to seconds [151]. The T_2* relaxation time is influenced by magnetic field irregularities and is always shorter than T_2.

A typical Spin-Warp pulse sequence timing diagram is represented in Fig. 14:

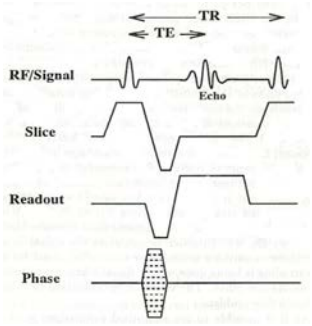

Figure 14: Spin-warp pulse sequence timing diagram (from [151] without permission).

The pulse sequences are associated with the timing diagrams of the RF chain, the frequency, the phase, and the slice selection gradients. Since phase encoding is repeated by pulsing the G_y gradient m times, it is customary to depict the phase encoding with a lobe that is indicative of such a process. Another interesting and important feature is the pre-phasor lobe with an area equal to half the area of G_x gradient, along the readout gradient. The lobe ensures that there is no net phase accumulation on spins due to G_x at the middle of the echo [151].

4.4.2 Fourier Transformation and Image Reproduction

A unique feature of MRI is the fact that the raw data is complex (unlike most other modalities that deal with real data). Therefore, a number of important properties of the Fourier transformation can be used in generating the image and in data acquisition, including the complex symmetry of data in Fourier space and others [151].

Image reconstruction in its simplest form involves application of a fast 2D discrete Fourier transformation.

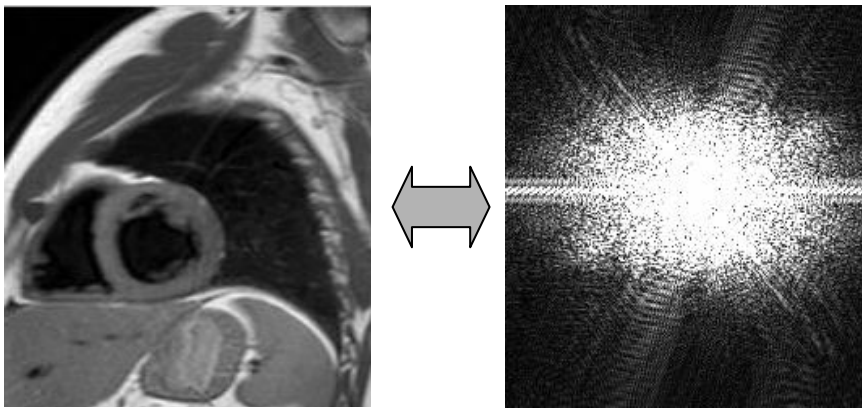

Figure 15: Myocardium view (short axis) in spatial space and k-space respectively (from [151] without permission).

The reproduction of MRI images is performed with the assistance of an image processing and a visualization software. Typical examples of MRI images (sagittal view) from a human head in 3 different postures are presented in Fig. 16.

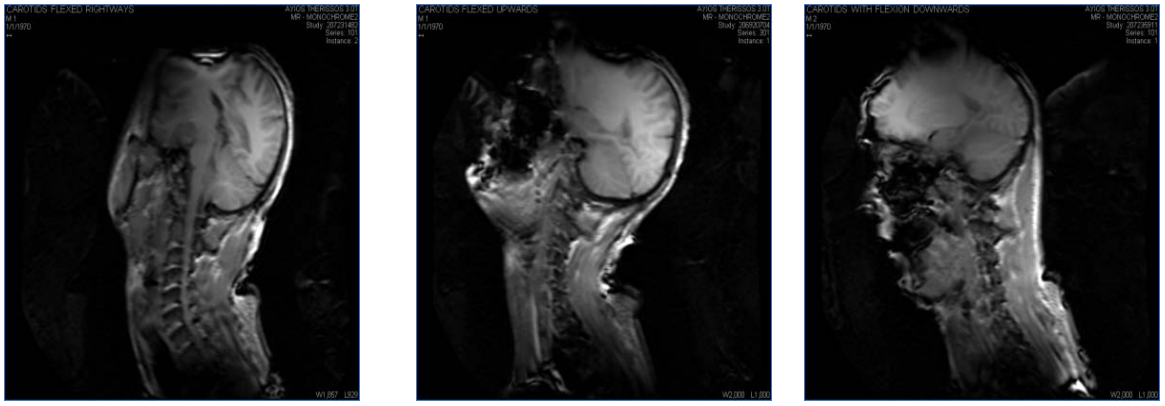

Figure 16: Three MRI images (sagittal view) from a human head in 3 different postures: (a) ~80^{o} Rotation Sideways, (b) ~45^{o} Flexion Up, (c) ~45^{o} Flexion Down. Data acquisition parameters: 3D gradient-echo pulse sequence, TR= 23ms, TE=3.5ms, α=20^{o}, acquisition voxel 0.36x0.36.0.12 mm^{3}, reconstruction voxel 0.2 x 0.2 x 0.6 mm^{3}.

4.4.3 Storage of MR Images

MRI images are stored and handled in a specific file format which is named DICOM (Digital Imaging and Communications in Medicine). This file format is standard for handling, storing, printing and transferring information in medical imaging. It includes a file format definition and a network communications protocol that uses TCP/IP to communicate between systems. The NEMA (National Electrical Manufacturers Association) holds the copyright to this standard. It was developed by the DICOM Standards Committee. DICOM standard was suggested in 1981 and the first version ACR/NEMA was released in 1985.

A DICOM data object consists of a number of attributes, including items such as name, ID, image dimensions etc., and also one special attribute containing the image pixel data.

Medical images are usually stored in hard discs, or in other digital media (CD, DVDs) as well as on the internet. In modern hospitals and diagnostic centers, electronic picture archiving and communication systems (PACS) have been developed in an attempt to provide economical storage and rapid retrieval of images. Electronic images and reports are transmitted digitally via PACS, which eliminates the need for manual filing, retrieval, and/or transportation of film jackets.

4.5 Various MRI techniques for studying Blood Vessels

This section will briefly describe the vascular imaging sequences utilized to acquire vascular images, called Magnetic Resonance Angiography (MRA).

4.5.1 Time-of-flight (TOF)

The Time of Flight sequence is a Gradient Echo (GRE) sequence having a TR shorter than the T1 of stationary tissues, to an extent that it determines saturation of stationary spins. Saturated tissue does not emit measurable relaxation, and it therefore appears dark. On the other hand, blood of first RF pulse is substituted by fresh blood which is excited again to regenerate an MR signal. This produces a high image contrast, depending on the flow rate and on the thickness of the layer. As seen in Fig. 17 (right) the image will be black where the stationary tissue is located and white where the flowing blood is found. For this reason, TOF technique is called “bright blood imaging” [152].

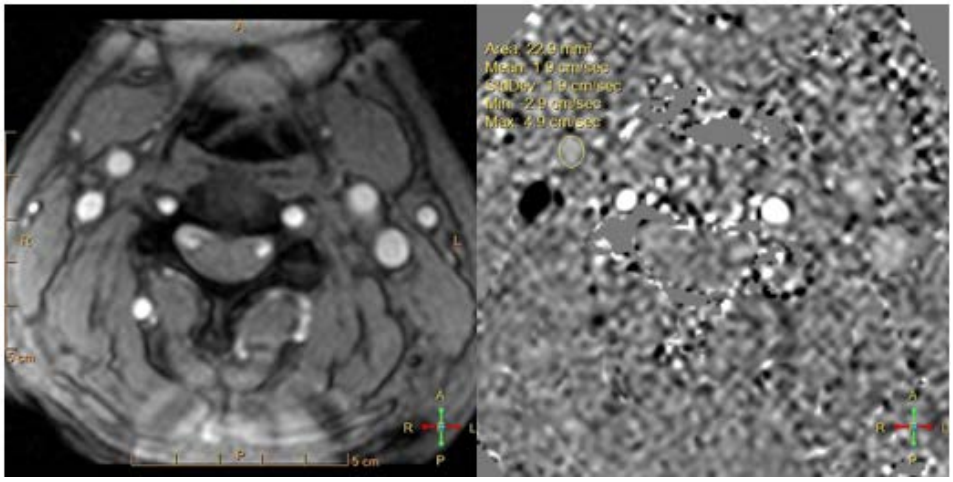

Figure 17:The TOF anatomic image (left) and the corresponding phase image (right).

4.5.2 Cine Phase Contrast (PC) MRI

The Phase Contrast (PC) method uses the phenomenon of phase shift as a signal source and the images produced are sensitive to flow. In phase contrast imaging, a positive gradient is applied first, then a negative one. The spins on the vessel wall have the same phase but the spins in the blood will change due to the gradient switch. PC MRI is also

used for velocity encoding (VENC) techniques to determine the flow velocity of the blood. The term *cine* refers to the fact that it is possible to acquire a number of consecutive images during the cardiac cycle [152].

The blood flow velocity in a pixel ($P_{i,j}$) depends on the encoding velocity (u_{enc}) and the number of DICOM gray levels (4096) and is calculated by [153]:

$$u_{P_{i,j}} = \frac{P_{i,j} \cdot u_{enc} \cdot 2}{4096} - u_{enc} \text{ (cm/s)} \quad (4.8)$$

4.5.3 Contrast Enhanced MR Angiography (CEMRA)

The contrast enhanced techniques presuppose the use of a contrast medium (ex. gadolinium-based), which is intravenously infused. The contrast agent determines a reduction in T1 of blood that in turn translates in a hyperintensity of flow signal over other surrounding tissue. Figure 18 illustrates an example of CEMRA. The success of an MRA with contrast bolus depends on the synchronization between acquisition of data and concentration of the contrast medium in the vascular district of interest [152].

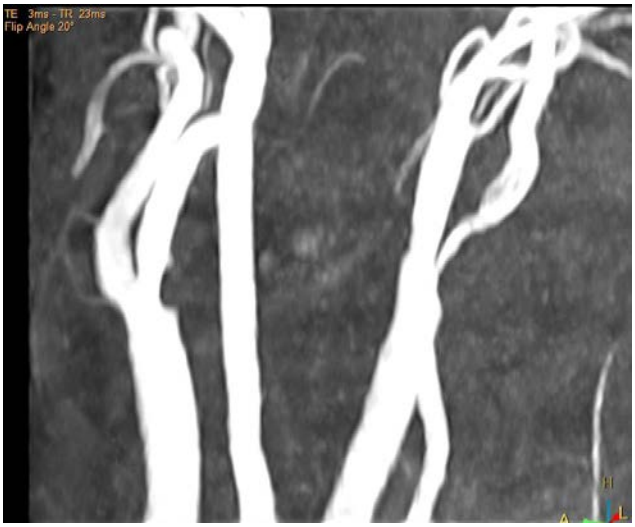

Figure 18: A contrast enhanced MR angiography

The overview of the MRI scan parameters for all the studies which took place for this thesis is represented in Table 4.

Table 4: Overview of MRI Parameters			
Study	Carotid - 3D TOF	Stenotic - Contrast-Enhanced Angiography	Flow data - Phase-Contrast
Parameters			
No. of slices	100	120	20
Thickness (mm)	1.2	1.2	5
TE (ms)	3.5	2	13
TR (ms)	23	6	20
FOV (mm)	160	200	160
Flip angle	20	27	10
Spatial Resolution			
x	0.2	0.3	0.2
y	0.2	0.3	0.2
z	0.6	0.6	0.6
Contrast Agent	-	Gadolinium-based (0.1 mmol/kg b.w.)	-
Velocity encoding (cm/s)	-	-	80-120
Cardiac phase	-	-	20

Part II: MRI-Based Carotid Bifurcation Reconstruction and Analysis of Geometric Parameters

Chapter 5:

MR Image Processing and 3D Surface Reconstruction

The interpretation and assessment of medical images were performed by a specialist radiologist, by employing the use of imaging to diagnose and treat disease visualized within the human body. Medical images provide a lot of clinical information for the internal structures of human body like the variety of organs and tissues. This clinical knowledge is necessary for the diagnosis, validation and reliability and last for the treatment strategy. Furthermore, medical imaging has the ability to contribute in a wide range of applications such as the design of surgical procedures and interventions as well as the quantification of tissue pathology. In order to achieve improved quality of images, successful extraction of a specified region of view, modeling, analysis and parameter quantification, various digital image processing procedures were performed.

5.1 Programming and MR Imaging of Human Carotid Artery

For the completion of this study, medical images from 10 volunteers were used in order to construct the right and left carotid bifurcation model for each individual. Also, image data from 4 patient volunteers with carotid stenosis were used for carotid modeling. The study was approved by the Cyprus Bioethics Committee and each volunteer signed a consent form.

Magnetic resonance (MR) images were acquired using a 3T MRI instrument (Philips Healthcare, the Netherlands) at the Ayios Therissos Imaging Center in Nicosia Cyprus. The built-in quadrature body coil was used for excitation. A phased array head-neck coil and a phased array, flexible, superficial coil were used for signal detection in supine and prone positions respectively. A series of 100 thin sequential slices were obtained in the axial plane by three dimensional (3D) times of flight (TOF) methods, covering the entire left and right carotid artery bifurcations and including parts of the common carotid artery (CCA), internal carotid artery (ICA) and external carotid artery (ECA). A gradient-echo pulse sequence was implemented with an echo time of 2.4 ms and a repetition time of 3.5 ms, while a nominal flip angle of 20° was used. The acquisition voxel size was 0.36 x 0.36 x 1.2 mm^3 and the reconstructed voxel 0.2 x 0.2 x 0.6 mm^3. A parallel imaging technique (SENSE factor 2) was employed to reduce acquisition time. Variable

flip angle (16-24 degrees) and gradient first moment nulling techniques were applied to decrease saturation effects of inflowing blood and reduce signal loss due to complex flow respectively. More details were represented earlier in paragraph 4.5.3.

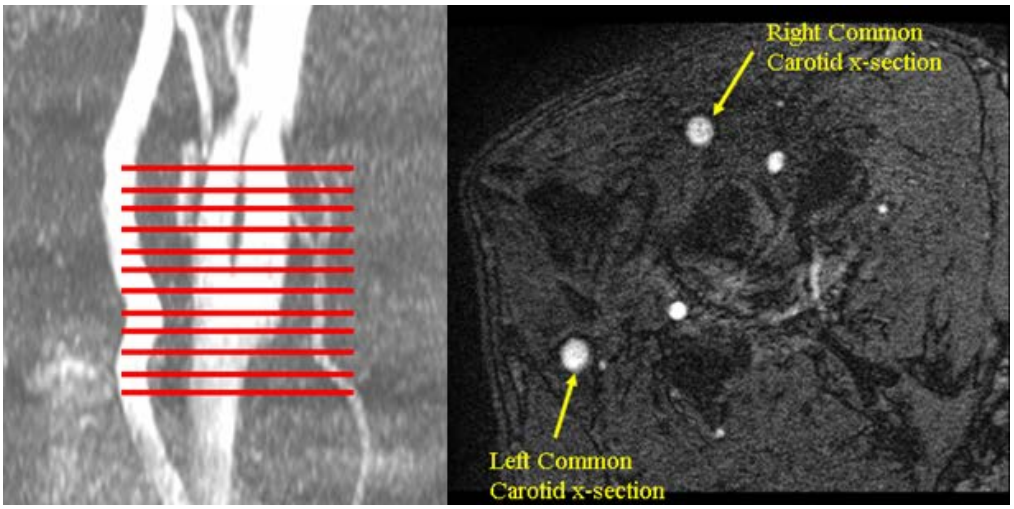

Figure 19: Series of sequential slices along carotid artery bifurcation (left). Axial slice shows the right and left carotid lumen (right).

Each healthy subject was imaged in two different scanning sessions on the same day corresponding to the two head postures examined: a) a neutral head posture with the subject in the supine position and b) a rightward head rotation posture with the subject in the prone position. Two of the subjects were scanned using the same MR protocol on a different day, in an interval of no longer than one month, to allow assessment of the accuracy of the experimental procedure.

The protocol followed for the patients was that each patient was imaged in two different scanning sessions corresponding to the two investigated head postures (neutral and leftward head rotation). In each session, contrast-enhanced (CE) angiographic images were acquired in the arterial phase following the intravenous bolus injection of a gadolinium-based contrast agent (Gadavist, Bayer Healthcare, Germany) at a dose of 0.1mmol/kg b.w. In each case, the prescribed transversal imaging stack was centered on the carotid bifurcation.

5.2 Construction of Human Carotid Artery from MRI

5.2.1 Software Selection for Biomechanics Analysis

To be able to construct, simulate and analyze various organs and parts of human body, the first step is to choose the right tools/software to help for the purpose achievement. There are a lot of commercial packages and open source software available, and Table 5 represents the software used in this study.

Table 5: The software used in this study for the construction of the 3D models from MRI and for CFD simulations.

	Software	Description
1	**ImageJ** (http://rsb.info.nih.gov/ij/), NIH, Bethesda, MD, USA)	An image processing program which can display, edit, analyze, process, save and print 8-bit, 16-bit and 320bit images.
2	**ITK-Snap** (http://www.itksnap.org/)	Software for segmenting anatomical structures in medical images. It provides an automatic active contour segmentation pipeline, along with supporting manual segmentation toolbox [154].
3	**VMTK** (http://www.vmtk.org/)	Libraries and tools for 3D reconstruction, geometric analysis, mesh generation and surface data analysis in image based blood vessel modeling [155].
4	**Segment** (http://www.segment.heiberg.se)	A comprehensive software package for medical image analysis. With the general object segmentation module it can be used for a wide range of radiology and cardiology applications [156].
5	**ANSYS ICEM-CFD v12.1** (http://www.ansys.com/, Ansys, Inc.)	A software package used for CAD and mesh generation. It is the pre–processor for FEA and CFD analysis.
6	**ANSYS FLUENT v12.1** (http://www.ansys.com/, Ansys, Inc., Canonsburg, Pennsylvania)	The software for computational fluid dynamics (CFD) analysis. Advanced solver technology that provides fast and accurate CFD results.
7	**Tecplot** (http://www.tecplot.com/, Tecplot, Inc., Bellevue, Washington)	Visualization software used in post – processing simulation results.
8	**Paraview** (http://www.paraview.org/, Kitware Inc, Los Alamos National Laboratory)	An open source, multi-platform data analysis and visualization application.

5.2.2 Image Segmentation

Image segmentation of high resolution medical images is a principal and necessary process in 3D modeling. The goal of segmentation is to subdivide the image in regions and objects that are easier to analyze. When this process is applied to a stack of 2D images, the resulting contours can be combined to create the 3D models. This can be achieved with the help of various interpolation algorithms like marching cubes.

Suppose there is an image **R**, segmentation subdivides this image into **N** discrete regions, {$\mathbf{R_1}$, $\mathbf{R_2}$, …, $\mathbf{R_N}$}, satisfying the segmentation law **P(R)**, then the following statements are true:

a) The subdivisions must completely cover the image
b) The subdivisions are unlinked
c) The pixel of every subdivision has the same properties
d) The subdivisions have to be discrete

The simplest segmentation method for a 2-D image **f(x,y)** utilizes the thresholding segmentation which mathematically is defined below:

$$g(x,y)=\begin{cases}1 & \text{if } f(x,y)>T \\ 0 & \text{otherwise}\end{cases} \tag{5.1}$$

5.3 3D Surface Model Constructions

The overview of the standard methodology followed for this study is represented in the next page in Fig. 21. More specifically, for image segmentation, the MR images were exported in DICOM format and were converted to a single volume (.img format) using ImageJ. The solid surface models were constructed by manual segmentation on a slice-by-slice basis using ITK-Snap [154, 157] as represented in Fig. 20B. The further imaging processing on the 3D geometries was accomplished by a vascular modeling toolkit (VMTK) [155]. A smoothing technique from VMTK utilizing the Taubin algorithm [158], which preserves the volume enclosed by the paramagnetic solution surface, was used for the reconstruction of the 3D lumen surface.

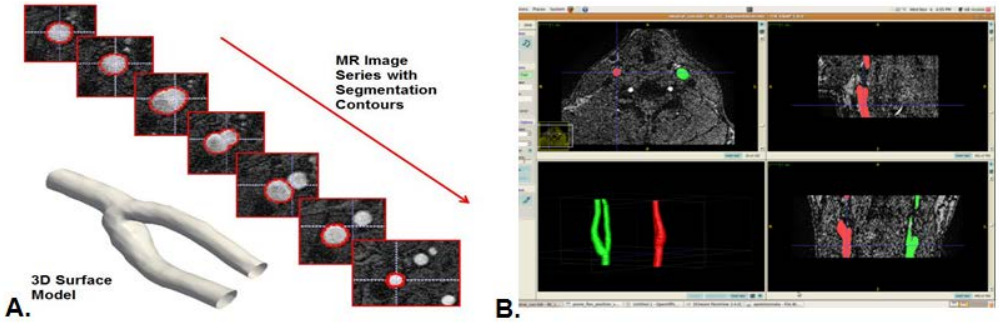

Figure 20: (A) MR image series with the segmentation contours and the resultant CB model. (B) Segmentation of Right (red) and Left (green) CB. The screen layouts are, top left Axial orientation, top right Sagittal, bottom right Coronal, and bottom left window represents the 3D models.

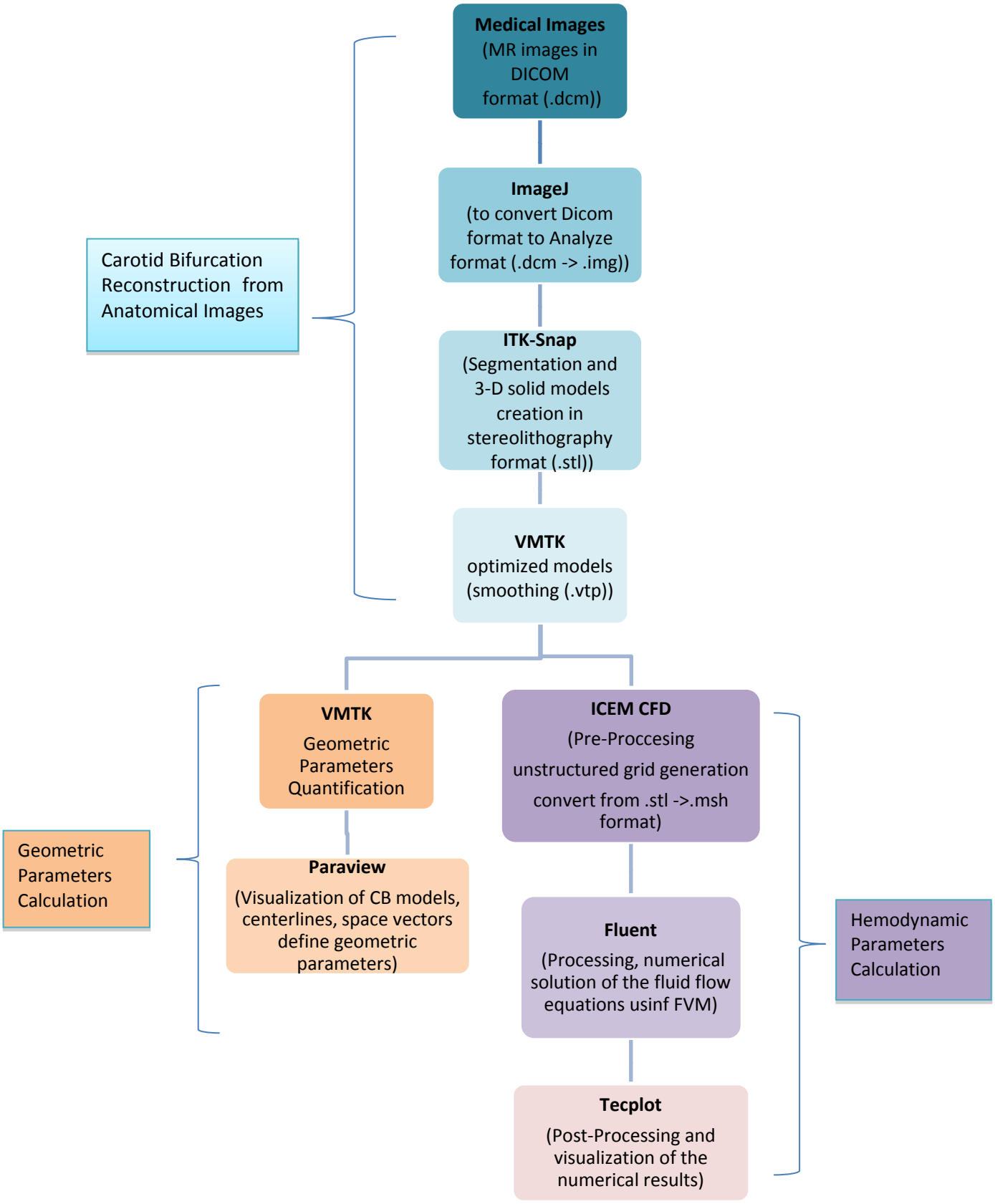

Figure 21: Diagrammatic representation of the methodology pursued from medical images to simulations.

5.4 Processing and Optimization of 3D Model

5.4.1 Effect of Smoothing Parameters

The initial 3D model, which was constructed after segmentation, has many surface abnormalities, e.g. the surface is very rough as it seems in Fig. 22 on the left. Thereby, to correct the model and make it more realistic it must pass from some smoothing procedures. Generally, in statistics and in image processing area, to achieve smoothing in a data set, a function (filter) must be generated and be able to hold the significant information and the same time discard the noise.

For this study the smoothing technique used were from VMTK software, which utilizes the Taubin algorithm [158]. Two main surface smoothing parameters in this algorithm are passband and iterations. The primer passband is the cut-off spatial frequency of the low pass filter and the latter iterations is the number of smoothing passes followed by VMTK. The use of smoothing algorithm leads to surface alterations, and consequently alterations to the model geometry. Using small passpand values (> 0.01), it is able to achieve more smooth surface and that may destroy (kill) the surface due to the huge geometric alterations. The result is to create a model with no relation with the initial. The iteration parameter defines the number of cycles of smoothing algorithm and here too, the large number of iterations leads to model geometry alterations.

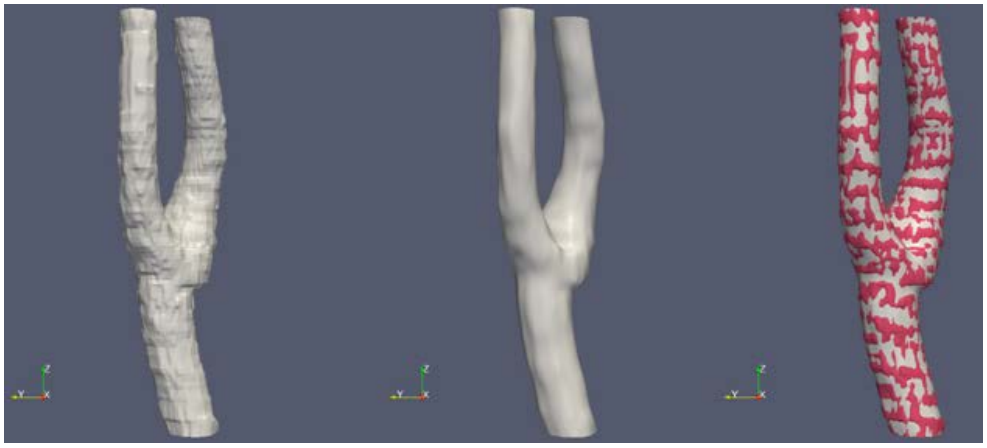

Figure 22: The initial constructed model (Left), the final smoothed model (middle), and the overlapping between initial and smooth model (right).

The optimum values for the smooth factor and iterations were obtained by doing a qualitative and a quantitative study. The qualitative study was done trying empirically various values for the two parameters, based on trial and error analysis. The tested values are represented in Table 6 and the corresponding models in Fig. 23 with white color. The parameters used for the optimum qualitative model were passband 0.04 and iterations 60 are represented as case *a*, the first model in Fig. 23. The overlapping between the initial (rough) and final (smoothed) model is more visible in this case.

The quantitative study showed that the same parameters lead to the optimum smoothed model. In more detail, in the comparison performed between the volume and surface area of the initial and final model, the values and the percent error present an infinitesimal variation (% error <5 %). The results for the quantitative study for case *a* are presented in Table 7 and indicate that the geometric alterations due to smoothing are not significant.

The percent error defined:

$$\%\, error = \left|\frac{I-F}{I}\right| \cdot 100\% \qquad (5.2)$$

where *I* the values for the initial model and *F* for the final model

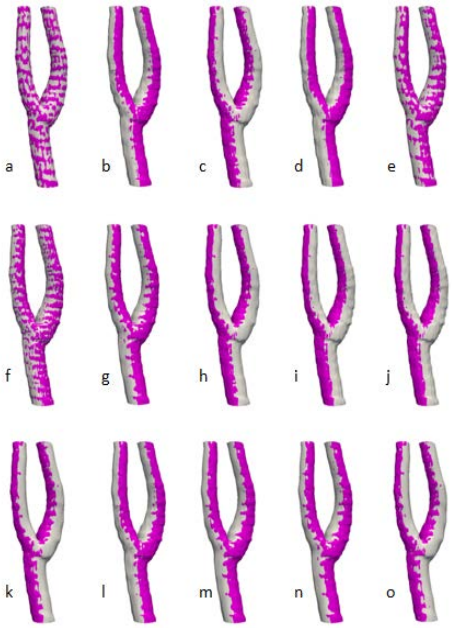

Figure 23: Overlapping of initial rough model (purple) and final smoothed model (white). Case a qualitative seem to fit best.

Table 6: The various values for passband and iterations tested.

Image	Passpand	Iterations
a	0.04 (optimized)	60
b	0.1 (default)	30
c	0.1	45
d	0.1	15
e	0.01	30
f	0.09	30
g	0.03	30
h	0.05	30
i	0.2	30
j	0.04	30
k	0.04	40
l	0.04	20
m	0.04	50
n	0.04	55
o	0.04	60

Table 7: Results of the reproducibility study.			
	Initial Model (Unsmoothed)	**Final Model** (Smoothed)	**% Error**
Volume (mm^3)	3297.6	3323.5	0.79
Surface Area (mm^2)	2024.9	1984.2	2.01

5.4.2 Reproducibility Results and Reliability Assessment

The reproducibility of geometric reconstruction is one of the most crucial steps in the modeling process [67, 159], and for that reason the accuracy of the segmentation and reconstruction procedures, as well as of the geometric parameter estimation was assessed. To estimate the reproducibility, the MRI acquisition procedure was repeated for two volunteers and for both investigated head postures using the same experimental setup and MRI protocol. Furthermore, the same procedure was followed for the segmentation and solid surface modeling processes. The definition and the physical meaning of the geometric parameters appear below and are defined extensively in paragraph 6.1.

Table 8 indicates the percent difference in the calculations of each geometric parameter after repeating the whole procedure of data acquisition and post-processing. The results demonstrate that, for both volunteers and postures studied, computed values of bifurcation angle and ICA angles, the error is acceptable (<30 %). For the ICA planarity and asymmetry angles, the error is unacceptably high and thus to the fact that these two angles are calculated by employing space vectors, which means that small changes in vector parameters may lead to large angle changes. In the supine position, the bifurcation area ratio, ICA/CCA, ECA/CCA, and ECA/ICA diameter ratios, tortuosity and curvature, present a percent error of less than 15 %. In the prone position, the error is strongly variable for the area and diameter ratios, tortuosity and curvature, partly due to the limited resolving power of the technique (i.e. short range of measured values).

The percent difference is defined here:

$$\% \, Diff = \frac{|E_1 - E_2|}{{}^1\!/_2 (E_1 + E_2)} \cdot 100\% \tag{5.3}$$

where E_1 and E_2 the values from the same parameter

Table 8: Results of the reproducibility study.						
Geometric Parameter			Volunteer I		Volunteer II	
			Right Carotid	Left Carotid	Right Carotid	Left Carotid
			% error in absolute value	% error in absolute value	% error in absolute value	% error in absolute value
Angle	Bifurcation	Supine	0.69	25.00	1.74	11.45
		Prone	23.95	12.15	1.94	15.53
	ICA	Supine	12.89	31.83	7.57	9.25
		Prone	4.63	33.21	16.07	15.60
	ICA Planarity	Supine	97.75	19.52	84.43	273.17
		Prone	46.22	31.01	208.42	53.75
	Asymmetry In Plane	Supine	118.43	49.51	500.00	1.29
		Prone	79.10	9.47	88.85	70.73
Area	Bifurcation Area Ratio	Supine	11.94	0.83	6.00	7.89
		Prone	37.50	17.71	26.45	28.83
	ICA/CCA	Supine	1.32	1.23	2.60	1.18
		Prone	2.44	1.37	12.36	2.47
	ECA/CCA	Supine	10.34	4.05	4.76	9.38
		Prone	37.50	20.00	15.63	28.36
	ECA/ICA	Supine	8.77	6.52	1.22	8.00
		Prone	38.97	22.73	4.17	25.61

5.4.3 Accuracy Estimation Using Phantom Studies

To test and validate the proposed methodology followed, a reproducibility study was performed on two volunteers. A part of it was a simple experimental phantom study carried out by imaging a flexible tube simulating the blood vessel in straight and flexed head postures. The phantom was comprised of a box-shaped container filled with sheep's milk yogurt in which flexible plastic tubes (polyvinyl chloride with 3 and 6 mm inner and outer diameter, respectively) filled with an aqueous solution (0.01 mM) of paramagnetic gadopentetic acid (Magnevist, Bayer Shering Pharma, Berlin, Germany) were immersed to represent blood-filled vessel segments adjacent to static anatomical structures. A straight-lying tube segment, a tube segment fixed around an extra-thin plastic hook of 8.*5* cm in diameter, as well as a bifurcation representing structure of three linear tube segments were interconnected via a rigid plastic one-to-two branching fitting (bifurcation and planarity angles of 50^{o} and 0^{o} respectively). Both were embedded into the yogurt and imaged at 3.0 Tesla using the same RF-receiver, and imaging pulse sequence was employed to image the volunteer's carotid bifurcation.

Signal-to-noise ratio (SNR) of the gadolinium chelate solution was close to that of the carotid blood in the human volunteer experiments, whilst contrast-to-noise ratio (CNR) between paramagnetic contrast agent solution and background (yogurt) approximated the average measured CNR between arterial blood and sternocleidomastoid muscle.

The methodology to construct the solid surface models was described in paragraph 5.3. Various features of the VMTK package were used to calculate the mean lumen diameter of the reconstructed model representing the straight-lying tube and the curvature of that representing the curved tube segment. The model developed from the images of the bifurcation resembling structure was used to measure geometric parameters such as the bifurcation and planarity angles, as well as the relevant bifurcation area ratio.

5.4.3.1 Straight Tube Phantom

For the first simple experiment, a flexible plastic tube was used following the steps as described in paragraph 5.3. As it is depicted in Fig. 24, the tube is not perfectly straight. This is because it was not perfectly fixed in the immersed material. The true tube dimensions, as measured by a rule before the experiment were: inner radius 1.6 mm and height 60 mm. The calculated volume from the formula $V=\pi r^2 h$ is 482.5 mm^3. The calculated volume from MR images and imageJ software was 559 mm^3. That calculation was achieved by multiplying the number of pixels in the tube lumen by the pixel size, for each image along the tube. The number of pixels was 23293, and the tube volume was calculated 559 mm^3. The main reason for this variation from the true volume is attributed to the manual segmentation.

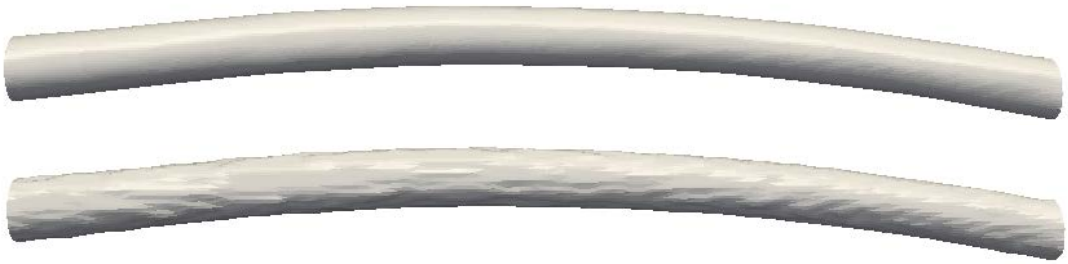

Figure 24: The smoothed (above) and unsmoothed (below) models of straight tube extracted from MR images and then manually segmented.

5.4.3.2 Curved Tube Phantom

For the second experiment the same tube was used with the only difference being the curvature existent on the tube. The same procedure was followed as described earlier and the constructed models are presented in Fig. 25. The curvature of a circle is defined to be the reciprocal of the radius $\kappa=1/r$, and in this case it was calculated 0.021 m^{-1}. To calculate the phantom curvature, the solid model was imported into ICEM CFD software as it seems in Fig. 26 and the curvature was estimated 0.023 m^{-1}. The infinitesimal variation is again due to the manual segmentation.

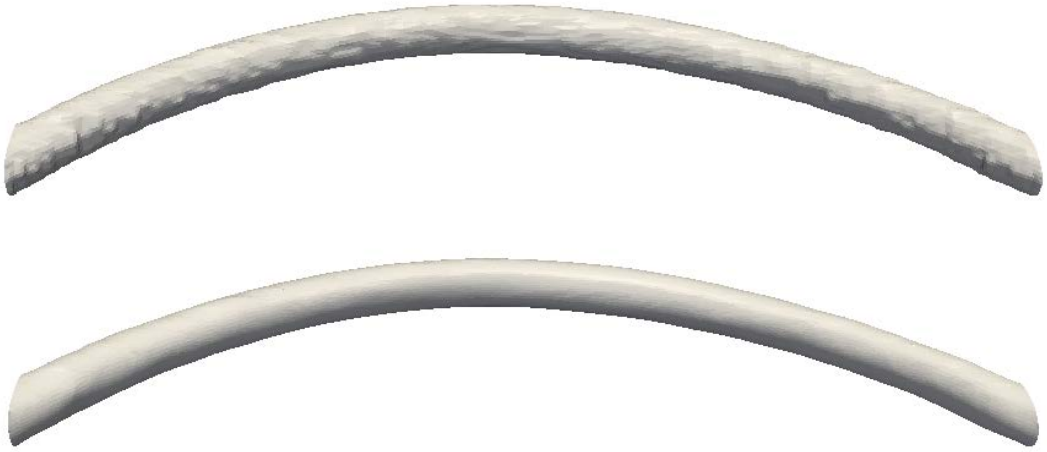

Figure 25: The unsmoothed (above) and smoothed (below) models of curved tube extracted from MR images and then manually segmented.

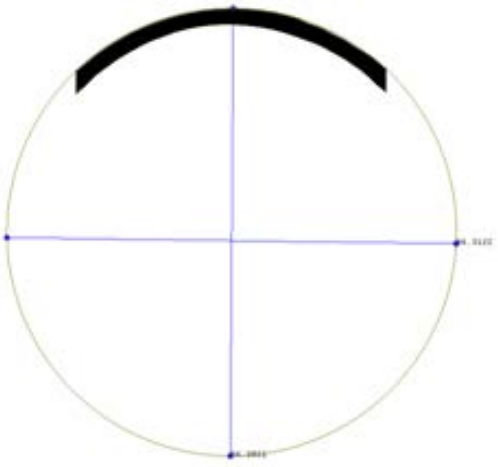

Figure 26: The phantom model imported in ICEM CFD for curvature estimation.

5.4.3.3 Bifurcation Phantom

The third experiment performed was more close to reality as the phantom was a rigid plastic in a Y-shape, like bifurcation shape. At the three ends the same elastic tubes were fitted. Fig. 27 represents the images of the maximum intensity projection (MIP) from MRI and the constructed 3D models.

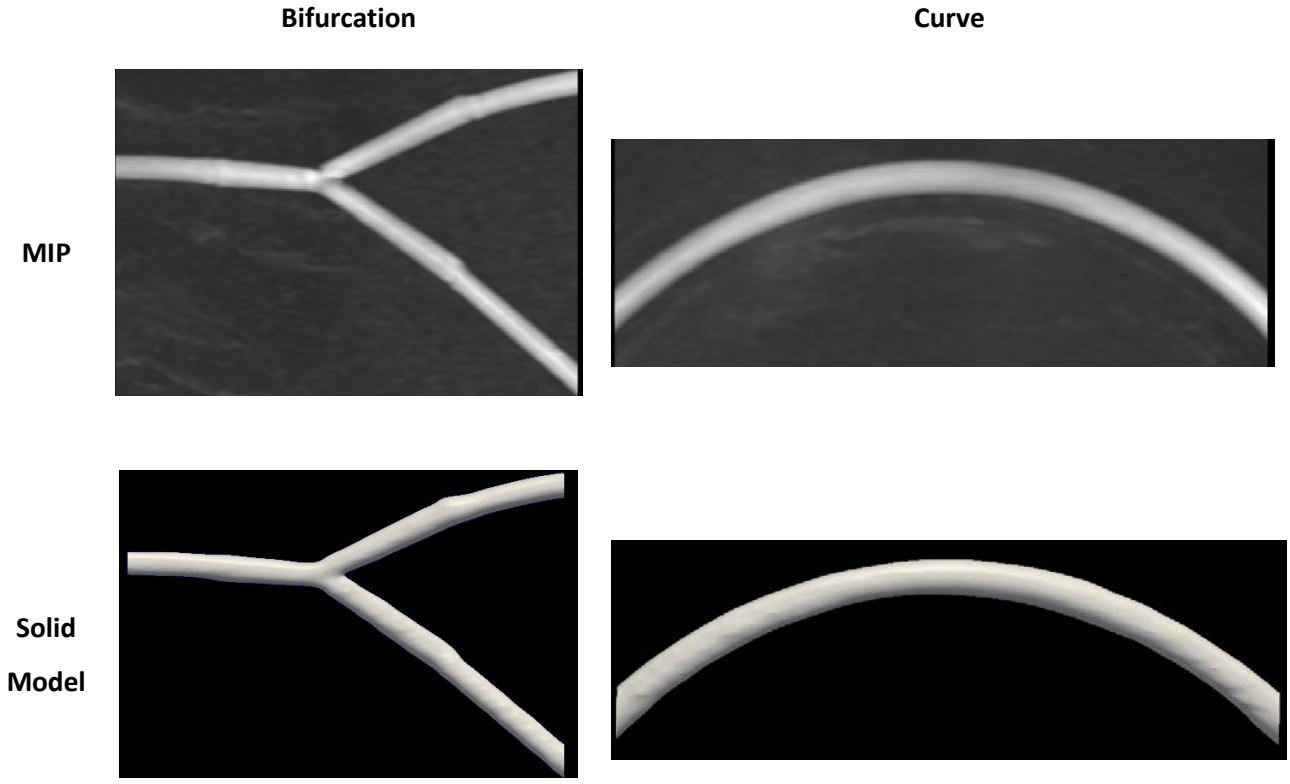

Figure 27: The MIP images for bifurcation phantom (top) and the corresponding solid models (bottom).

The analysis for the bifurcation phantom was done on the clipped model using VMTK and is summarized in Table 9. The values calculated from images are converging with realistic measured values of phantom, as expected.

Table 9: The geometric parameters of phantom and the corresponding values estimated by VMTK for bifurcation model.			
		Phantom	**VMTK**
Bifurcation Angle		55	54.06
ICA Angle		27.5	27.51
ICA Planarity Angle		0	0.59
Asymmetry Angle		0	0.97
Bifurcation Area Ratio		2	1.84
ICA/CCA		1	0.96
ECA/CCA		1	0.96
ECA/ICA		1	1.00
Diameter	CCA	3.2	3.14
	ICA	3.2	3
	ECA	3.2	3.02
Curvature	CCA	0	0.05
	ICA	0	0.05
	ECA	0	0.08
Tortuosity	CCA	0	0.006
	ICA	0	0.001
	ECA	0	0.002

5.4.3.4 Curved Bifurcation Phantom

On the last experiment, planarity was added to the bifurcation model used before. That implies that the bifurcation model is not lying on a flat level as it was previously. The Y-shaped solid plastic was transformed to have planarity around 30^{o} as presented in **Fig. 28**. The results for this study are represented at **Table 10** and show great consistency between reality measurements and calculations from MR images and VMTK.

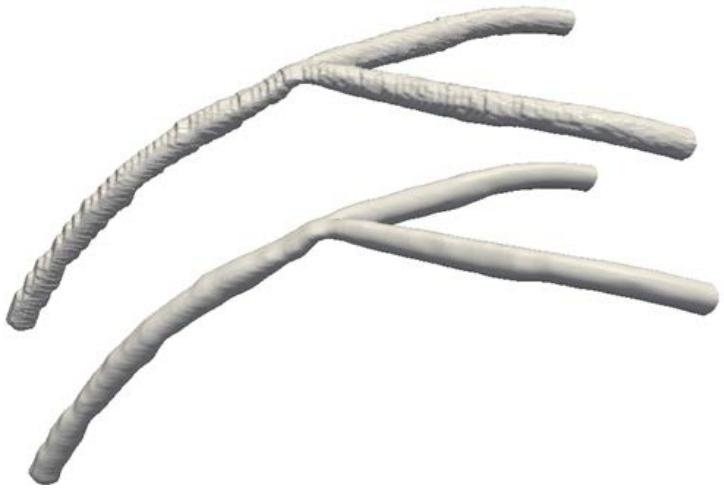

Figure 28: The unsmoothed (above) and smoothed (below) models of curved bifurcation model extracted from MR images.

Table 10: The geometric parameters of phantom and the corresponding values estimated by VMTK for curved bifurcation phantom.			
		Phantom	**VMTK**
Bifurcation Angle		55	30.83
ICA Angle		27.5	13.52
ICA Planarity Angle		30	28.97
Asymmetry Angle		0	3.79
Bifurcation Area Ratio		2	2.75
ICA/CCA		1	1.41
ECA/CCA		1	0.87
ECA/ICA		1	0.62
Diameter	CCA	3.2	3.32
	ICA	3.2	3.3
	ECA	3.2	3.26
Curvature	CCA	0.015	0.17
	ICA	0.014	0.09
	ECA	0.014	0.09
Tortuosity	CCA	0	0.018
	ICA	0	0.005
	ECA	0	0.006

Chapter 6:

Description, Quantification and Statistical Analysis of Geometric Parameters

The objective of this study was to investigate the alteration in geometric parameters of both CB with the head in two different postures, neutral supine and rotated rightwards. Several studies over the years have demonstrated that the vessel geometry plays a key role in the local hemodynamics and consequently is a risk factor for atherogenesis [6, 7, 46, 50, 160-162]. The configuration and the angle of the ICA sinus produce an area of low WSS and alter the hemodynamic field [41]. Another study by Sitzer *et al.* suggested that the angle of ICA origin may be an independent risk factor for early atherosclerotic changes [163]. Lee *et al.* in a study of 50 normal CB found a relationship between disturbed flow and both proximal area ratio and toruosity [164]. Another study with 32 volunteers (n=64 CB) performed by Markl *et al.* confirm the results of Lee *et al.* and furthermore found a significant relationship between high OSI and increased bifurcation angle found [165]. Recently, Harloff and Markl found a significant relationship between critical WSS and ICA/ECA ratio and also found a correlation between regions exposed to critical OSI and geometric parameters such as bifurcation angle, tortuosity and ICA/ECA ratio [166]. Finally, a recent study from Bijari *et al.* presented redefinitions of classical geometric variables and concluded that these indicators improve hemodynamic predictions without burdening the reproducibility [167]. The definitions of significant geometric parameters which improve the morphological characterization of the human carotid are defined below. The results obtained from this study and the content of this section was published in [168].

6.1 Definition of Geometric Features

Using various features of the VMTK package, specific important geometric parameters were identified such as bifurcation angle, ICA angle, ICA planarity angle, in-plane asymmetry angle, curvature and tortuosity. Bifurcation area ratio, ICA/CCA, ECA/CCA, and ECA/ICA diameter ratios were also calculated for right and left carotids. The geometric parameter definitions (Fig. 29) are as follows [169]:

a. **Bifurcation angle** is the angle between the projections of ICA and ECA vectors on to the bifurcation plane (Fig. 29 middle).

b. **ICA angle** is the angle between the projections of CCA and ICA on to the bifurcation plane (Fig. 29 middle).

c. **ICA planarity angle** is the angle between the out of plane components of the CCA and ICA vectors. Also planarity parameter is a very sensitive parameter, and so a single measurement can never fully characterize the bifurcation [170] (Fig. 29 right).

d. **In-plane asymmetry angle** is defined as the difference between two angles (|α-β|), the angle between ICA and CCA (*α*) and the angle between CCA and ECA (*β*) (Fig. 29 middle). The bifurcation is symmetric when *α* and *β* are equal [171].

e. Vessel **tortuosity** was calculated as *L/D-1* where L is the length of the centerline from the origin to the end of the branch, and D is the Euclidean distance between these two points (Fig. 29 left).

f. Vessel **curvature** is defined as the inverse of the radius of the local osculating circle. Curvature values were averaged over the length of the CCA, ECA and ICA segments of the computed centerlines (Fig. 29 left).

The calculation of the last two geometric parameters comes from the centerline parameterization. The Frenet-Serret formula provides the rates of change of the three unit vectors along the centerline in an orthogonal coordinate system. The unit vectors are [172, 173]:

$$T = \frac{dR}{ds},\ N = \frac{1}{\kappa}\frac{dT}{ds},\ B = T \times N \tag{6.1}$$

where *T, N* and *B* the unit tangent, normal and binormal vectors respectively
R, *s* the vector position and the arc length r
κ the centerline curvature

Frenet-Serret formulas

$$\frac{dT}{ds} = \kappa N,\ \frac{dN}{ds} = \tau B,\ \frac{dB}{ds} - \tau N \tag{6.2}$$

where *κ* the curvature and measures the deviation of the curve from a straight line
τ the torsion and measures how sharply the line is twisting in space, the sign indicates the clockwise and counter-clockwise rotation

Thomas *et al.* in their study in 2002 concluded that curvature has a marked influence on the magnitude of hemodynamic parameters such as WSS and OSI. However, they

suggested that the vessel planarity has a minor effect on the spatial distribution of TAWSS and OSI [174]. Caro *et al.* had also supported before that "non-planarity" is an important factor influencing the arterial flows, including WSS [50].

All carotid models were clipped at specific locations, at three or five sphere radii from the bifurcation point (CCA3, ICA5 and ECA5, as shown in Fig. 29 left). The number in the specific locations CCA3, ECA5 and ICA5 indicates their geodesic distance along the centerline from reference points defining the boundaries of the CCA, and the ECA, ICA branches measured in units of maximally inscribed sphere radii as defined in [155]. Therefore, similar lengths of CCA, ICA and ECA segments were used for tortuosity and curvature calculations independent of carotid, subject and scanning session.

Bifurcation area ratio (BAR) was defined earlier in paragraph 2.2.3.1, and is the sum of the ICA5 and ECA5 areas divided by the CCA3 area. The other ratios are: a) ICA5/CCA3, b) ECA5/CCA3, and c) ECA5/ICA5, and are calculated as the square root of the corresponding area ratios [175].

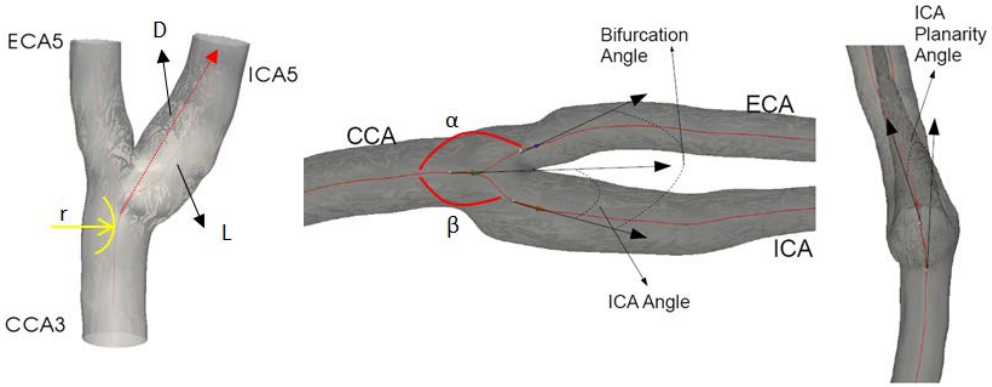

Figure 29: Graphical representation of some of the bifurcation geometric parameters assessed in this study.

6.2 Quantification and Comparison of Geometric Parameters Between Supine Position and the Prone Position with Head Rotation

Using image processing to create the bifurcation 3D surface models from MR images and with the help of some features of VMTK package, the quantification of prescribed geometric parameters was summarized in the tables below for the supine and prone head positions. The tables show the commonly used statistics numbers that describe

the sample of observations from the volunteers group. A brief review of the statistics numbers used in this study is presented below [176].

The most useful single statistic number for describing a set of observations is one that describes the center or the location of the distribution of the observations, and the most common number is called the average or the arithmetic mean. The mean for a sample is defined as the sum of all the observations divided by the number of observations. The formula for the mean value is represented below:

$$\bar{X} = \frac{(X_1 + X_2 + \cdots + X_n)}{n} = \sum_i^n \frac{X_i}{n} \tag{6.1}$$

where: $\bar{X}$ the mean value
n the number of observations in a sample
i the number of observation

Another measure of location that is often used is the median, the number that divides the total number of ordered observations in half. The median provides the numerical value of a variable for the middle or most typical case and for clinical data the proper statistic is the median. The median, if *n* is odd, is the numerical value of the (*n*+1)/2 ordered observation and if *n* is even the median is the mean of the *n/2* and *(n/2*)+1 observations.

The second most useful statistical number for describing a set of observations is one that gives the variability or dispersion of the distribution of observations. The sample variance is defined as the sum of squares of the differences between each observation in the sample and the sample mean divided by *n-1*. The variance of the sample is usually denoted by s^2 and the formula is:

$$s^2 = \frac{\sum(X - \bar{X})^2}{n-1} \tag{6.2}$$

The square root of the variance is also frequently used and named as the standard deviation:

$$s = \sqrt{\frac{\sum(X - \bar{X})^2}{n-1}} \tag{6.3}$$

Another useful measure of variation used and calculated for this study is the interquartile range (IQR). This is a safe way to obtain a type of range that utilizes observations by discarding the largest and smallest values. The interquartile range is defined as *IQR=Q3–Q1*. With this procedure three quartiles divide the distribution into four equal parts, with 25% of the distribution in each part. The first quartile (Q1) divides the lower half of the distribution into halves, and similarly the Q3 divides the upper half into halves. The second quartile (Q2) is the median. To compute the intervals Q1 and Q3 the interpolation is often required. Finally, the data tables include the maximum and minimum sample values.

First, Table 11 represents the results for the right carotid bifurcation from all volunteers (n=10) and for the two investigated head postures. The table includes the first (Q1) and the third (Q3) quartile, the median and mean value, the standard deviation (SD) and the maximum and minimum values (max, min).

Table 11: Table of geometric parameters of right carotid bifurcation.

Geometric Parameter		n	Head Position	Q1	Median	3rd	Mean	SD	max	min
Angles	Bifurcation	10	neutral	32.37	38.86	41.27	38.13	6.47	48.37	30.17
		10	prone	42.88	46.62	56.76	48.19	9.64	62.42	34.69
	ICA	10	neutral	14.80	18.06	22.58	18.41	6.00	27.41	7.19
		10	prone	21.97	23.14	33.81	26.64	9.71	41.78	12.51
	ICA Planarity	10	neutral	2.84	5.23	7.15	5.37	3.37	11.09	0.84
		10	prone	3.15	6.30	10.53	7.10	5.21	15.23	0.84
	Asymmetry	10	neutral	3.36	7.00	10.92	7.59	5.37	17.89	0.37
		10	prone	10.09	12.39	19.80	13.48	7.00	22.06	0.63
Tortuosity	CCA	10	neutral	0.00	0.01	0.01	0.01	0.01	0.02	0.00
		10	prone	0.01	0.01	0.01	0.01	0.01	0.02	0.00
	ICA	10	neutral	0.01	0.01	0.01	0.01	0.01	0.02	0.00
		10	prone	0.01	0.02	0.04	0.03	0.02	0.06	0.01
	ECA	10	neutral	0.01	0.01	0.01	0.01	0.01	0.03	0.00
		10	prone	0.01	0.01	0.03	0.02	0.02	0.06	0.01
Curvature	CCA	10	neutral	0.04	0.04	0.04	0.04	0.01	0.08	0.03
		10	prone	0.03	0.04	0.04	0.04	0.02	0.09	0.02
	ICA	10	neutral	0.03	0.05	0.05	0.04	0.01	0.06	0.02
		10	prone	0.02	0.06	0.08	0.06	0.04	0.13	0.02
	ECA	10	neutral	0.04	0.05	0.06	0.05	0.02	0.09	0.02
		10	prone	0.05	0.07	0.09	0.08	0.04	0.20	0.05
AREA RATIOS	BF Area Ratio	10	neutral	1.11	1.26	1.36	1.23	0.16	1.44	0.98
		10	prone	1.16	1.22	1.37	1.25	0.22	1.67	0.84
	ICA/CCA	10	neutral	0.76	0.79	0.81	0.80	0.06	0.90	0.73
		10	prone	0.75	0.82	0.88	0.81	0.08	0.93	0.71
	ECA/CCA	10	neutral	0.68	0.75	0.86	0.76	0.12	0.92	0.56
		10	prone	0.67	0.76	0.84	0.76	0.10	0.90	0.59
	ECA/ICA	10	neutral	0.81	0.98	1.09	0.96	0.19	1.26	0.69
		10	prone	0.85	0.98	1.02	0.94	0.15	1.17	0.70

The next table (Table 12) represents the same parameters for the same volunteers but for the left carotid bifurcation.

Table 12: Table of geometric parameters of left carotid bifurcation.										
Geometric Parameter		**n**	**Head Position**	**1st**	**Median**	**3rd**	**Mean**	**SD**	**max**	**min**
Angles	**Bifurcation**	10	neutral	38.46	47.93	54.14	47.79	10.66	64.91	33.42
		10	prone	31.20	33.80	38.69	36.04	7.54	50.60	27.69
	ICA	10	neutral	19.46	26.33	30.25	24.76	7.40	34.50	14.29
		10	prone	9.07	14.64	23.09	16.66	11.06	38.61	3.26
	ICA Planarity	10	neutral	1.38	3.93	10.01	6.13	6.31	19.36	0.04
		10	prone	3.17	5.12	10.45	6.20	4.88	13.40	0.06
	Asymmetry	10	neutral	3.70	6.08	12.04	7.66	5.01	15.43	2.04
		10	prone	4.99	14.80	21.95	14.42	10.16	29.22	1.49
Tortuosity	**CCA**	10	neutral	0.01	0.01	0.01	0.01	0.01	0.03	0.00
		10	prone	0.01	0.01	0.01	0.01	0.01	0.02	0.00
	ICA	10	neutral	0.01	0.02	0.02	0.02	0.02	0.05	0.00
		10	prone	0.01	0.01	0.02	0.02	0.01	0.03	0.01
	ECA	10	neutral	0.01	0.01	0.02	0.01	0.01	0.02	0.00
		10	prone	0.01	0.01	0.02	0.01	0.01	0.03	0.00
Curvature	**CCA**	10	neutral	0.03	0.04	0.04	0.04	0.01	0.06	0.03
		10	prone	0.03	0.04	0.04	0.04	0.01	0.05	0.02
	ICA	10	neutral	0.03	0.05	0.07	0.05	0.02	0.08	0.02
		10	prone	0.04	0.04	0.06	0.05	0.02	0.08	0.03
	ECA	10	neutral	0.04	0.06	0.08	0.06	0.03	0.11	0.03
		10	prone	0.05	0.06	0.08	0.07	0.02	0.10	0.04
AREA RATIOS	**BF Area Ratio**	10	neutral	1.17	1.30	1.41	1.30	0.16	1.53	1.05
		10	prone	1.10	1.14	1.32	1.19	0.15	1.43	0.96
	ICA/CCA	10	neutral	0.78	0.81	0.85	0.83	0.08	0.99	0.74
		10	prone	0.77	0.81	0.84	0.80	0.08	0.94	0.67
	ECA/CCA	10	neutral	0.70	0.77	0.81	0.77	0.10	0.95	0.64
		10	prone	0.66	0.69	0.81	0.73	0.10	0.89	0.62
	ECA/ICA	10	neutral	0.88	0.91	1.03	0.95	0.18	1.23	0.67
		10	prone	0.81	0.88	0.98	0.92	0.18	1.32	0.71

The last table (Table 13) represents synoptically the results for both carotid bifurcations combined.

Table 13: Table of geometric parameters of both right and left carotid bifurcations.										
Geometric Parameter		**n**	**Head Position**	**1st**	**Median**	**3rd**	**Mean**	**SD**	**max**	**min**
Angles	**Bifurcation**	20	neutral	35.03	41.09	48.91	42.96	9.91	64.91	30.17
		20	prone	34.01	41.09	47.80	42.11	10.48	62.42	27.69
	ICA	20	neutral	15.42	20.85	26.62	21.58	7.32	34.50	7.19
		20	prone	13.82	22.15	28.23	21.65	11.35	41.78	3.26
	ICA Planarity	20	neutral	1.75	4.49	7.68	5.75	4.94	19.36	0.04
		20	prone	3.05	5.85	11.43	6.65	4.94	15.23	0.06
	Asymmetry	20	neutral	3.40	6.66	11.58	7.62	5.06	17.89	0.37
		20	prone	8.64	13.79	20.34	13.95	8.50	29.22	0.63
Tortuosity	**CCA**	20	neutral	0.01	0.01	0.01	0.01	0.01	0.03	0.00
		20	prone	0.01	0.01	0.01	0.01	0.01	0.02	0.00
	ICA	20	neutral	0.01	0.01	0.02	0.02	0.01	0.05	0.00
		20	prone	0.01	0.01	0.02	0.02	0.01	0.06	0.01
	ECA	20	neutral	0.01	0.01	0.02	0.01	0.01	0.03	0.00
		20	prone	0.01	0.01	0.02	0.02	0.01	0.06	0.00
Curvature	**CCA**	20	neutral	0.04	0.04	0.04	0.04	0.01	0.08	0.03
		20	prone	0.03	0.04	0.04	0.04	0.02	0.09	0.02
	ICA	20	neutral	0.03	0.05	0.06	0.05	0.02	0.08	0.02
		20	prone	0.03	0.05	0.07	0.05	0.03	0.13	0.02
	ECA	20	neutral	0.04	0.05	0.07	0.06	0.03	0.11	0.02
		20	prone	0.05	0.06	0.08	0.07	0.03	0.20	0.04
AREA RATIOS	**BF Area Ratio**	20	neutral	1.16	1.27	1.38	1.26	0.16	1.53	0.98
		20	prone	1.13	1.21	1.36	1.22	0.19	1.67	0.84
	ICA/CCA	20	neutral	0.77	0.80	0.85	0.81	0.07	0.99	0.73
		20	prone	0.76	0.81	0.86	0.81	0.08	0.94	0.67
	ECA/CCA	20	neutral	0.68	0.76	0.85	0.77	0.11	0.95	0.56
		20	prone	0.66	0.74	0.84	0.74	0.10	0.90	0.59
	ECA/ICA	20	neutral	0.82	0.94	1.06	0.95	0.18	1.26	0.67
		20	prone	0.82	0.95	1.01	0.93	0.16	1.32	0.70

The comparison between the two investigated head positions is not very easily done from the tables above so the use of histograms is necessary. For bifurcation angle and ICA angle the comparison of the two head positions is presented in the following histograms (Fig. 30). It is evident that head rotation to the right affects bifurcation and ICA angles of both carotids. It seems, however, that head rotation alters the ICA angle more than the bifurcation angle in relative values. The results for both angles are in accordance with similar findings from a much larger sample of volunteers (n=50) [175].

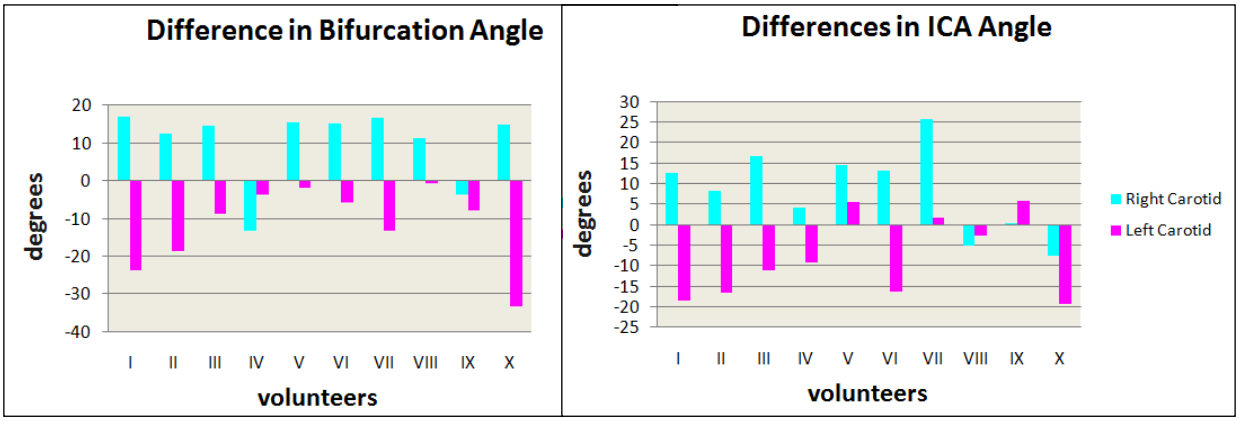

Figure 30: Differences for the Bifurcation and ICA angle between supine and rotation postures of both carotids and for all volunteers. Positive and negative values signify increase and decrease respectively with head rotation.

From existed data from all individuals and both left and right carotids (n=40), a small study took place to calculate the mean and median value for the lumen radius of all CB. The highlighted results (Table 14) indicate that the results for median values obey Murray's law which was defined in the introduction, paragraph 2.2.3.1.

Table 14: Results for Murray's and Square Law (n=40).

	Mean			Median			STDEV		
	CCA3	ICA5	ECA1	CCA3	ICA5	ECA1	CCA3	ICA5	ECA1
	3.22	2.60	2.43	3.21	2.61	2.44	0.21	0.27	0.34
Murray's Law	33.464 = 32.052			32.922 = 32.204					
Square Law	10.385 = 12.698			10.272 = 12.740					

Regression and Correlation

In this section, the relationship between geometric parameters is investigated to estimate whether there are any relations between them. Firstly, the simplest and probably the most useful graphical technique for displaying the relation between two variables is the scatter diagram. The first step in making a scatter plot is to decide which variable is the dependent variable (outcome) and which is the independent variable (predictor). The scatter diagrams are useful in indicating the relationship between the predictor and outcome variables and whether the relationship between the two variables is positive or negative. After plotting the scatter diagram, a straight line or a curve is fitted to the data points [176]. The line which best fits to the data in this study is the least-squares regression line. The equation of the line is:

$$\hat{Y} = a + bX \tag{6.4}$$

where $\hat{Y}$ the value of Y on the regression line for a given X
a interception of the line
b the slope of the line

Correlation Coefficient

The correlation coefficient always lies between -1 and +1. A correlation coefficient of 0 means that there is no linear relation, and if all the data points lie precisely on a straight line the correlation coefficient is exactly -1 for negative slope or +1 for positive slope.

The definition of the correlation coefficient (rho) is:

$$rho = \frac{\sum(X-\bar{X})(Y-\bar{Y})}{\sqrt{\sum(X-\bar{X})^2 \sum(Y-\bar{Y})^2}} \tag{6.5}$$

Figure 31 shows the scatter plots for the bifurcation and ICA angle changes in both carotids. Correlation analysis results that for RCB, there was moderate correlation (rho=0.69) between the percentage changes of the bifurcation and ICA angle with head rotation. For the LCB no correlation was found (rho=0.26). Also no correlation (rho=0.07) was found for bifurcation angle between the two carotids. Regarding tortuosity and curvatures, also no correlation was found for either carotid. The statistical analyses were performed by R statistical package [177].

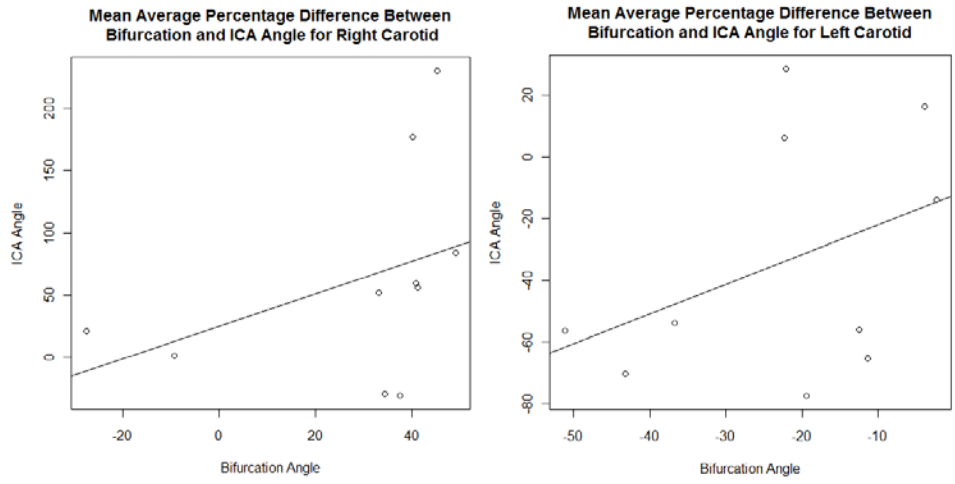

Figure 31: Scatter plots for correlation values of Bifurcation and ICA angle for the right and left carotid (n=10).

Box plots

Apart from histograms for displaying the observations, another commonly used graph is the box plot which is a convenient of graphically depicting groups of numerical data through their five-number summaries: a) the sample minimum, b) the lower quartile (Q_1), c) the median (Q_2), d) the upper quartile (Q_3) and e) the sample maximum. A box plot may also indicate which observations might be considered outliers or extreme values. The length of the box is the IQR range and the vertical lines above and below the box are the "whiskers". The horizontal lines at the whiskers ends are called "fences". The upper fence is at (Q_3+1.5(IQR)) and the lower fence is at (Q_3-1.5(IQR)).

The Wilcoxon Test

The Wilcoxon signed test is a nonparametric test which is used when the data are in pairs. The nonparametric tests can be used when the data are not from a normal distribution or any other known distribution and are what is called distribution-free. In this study it is not sure what distribution the data followed, as the sample was too small.

First, the null hypotheses must be tested and that says that the bifurcation angle distribution for supine position is the same as the distribution for prone position. Although the bifurcation values in prone position (RCB) tend to be higher, there was no prior theory to tell us what to expect so the two-sided test was necessary. Here, the Wilcoxon signed-rank test was performed between the two investigated head postures using the R statistical package [177].

Figure 32 represents synoptically the median values and interquartile ranges of the geometric parameters estimated in the case of all volunteers. For the RCB, the bifurcation and ICA angles increase significantly with head rotation to the right, while both angles of the LCB decrease in prone position. Median values for tortuosity and curvature do not differentiate substantially with head rotation, while ICA and ECA vessels typically exhibit higher curvature in comparison to CCA independently of head posture. Computed median values of area and diameter ratios also suggest that there is no strong dependence due the head posture. Comparison between the RCB and LCB

revealed a significantly (p=0.04) higher bifurcation angle in the supine position, as well as a significantly (p=0.04) lower ICA angle in the prone position, for the LCB. For both bifurcation and ICA angles, head rotation to the left seems to inflict a change toward the same direction (i.e., increase or decrease) as that effected by head rotation to the right, for both carotids.

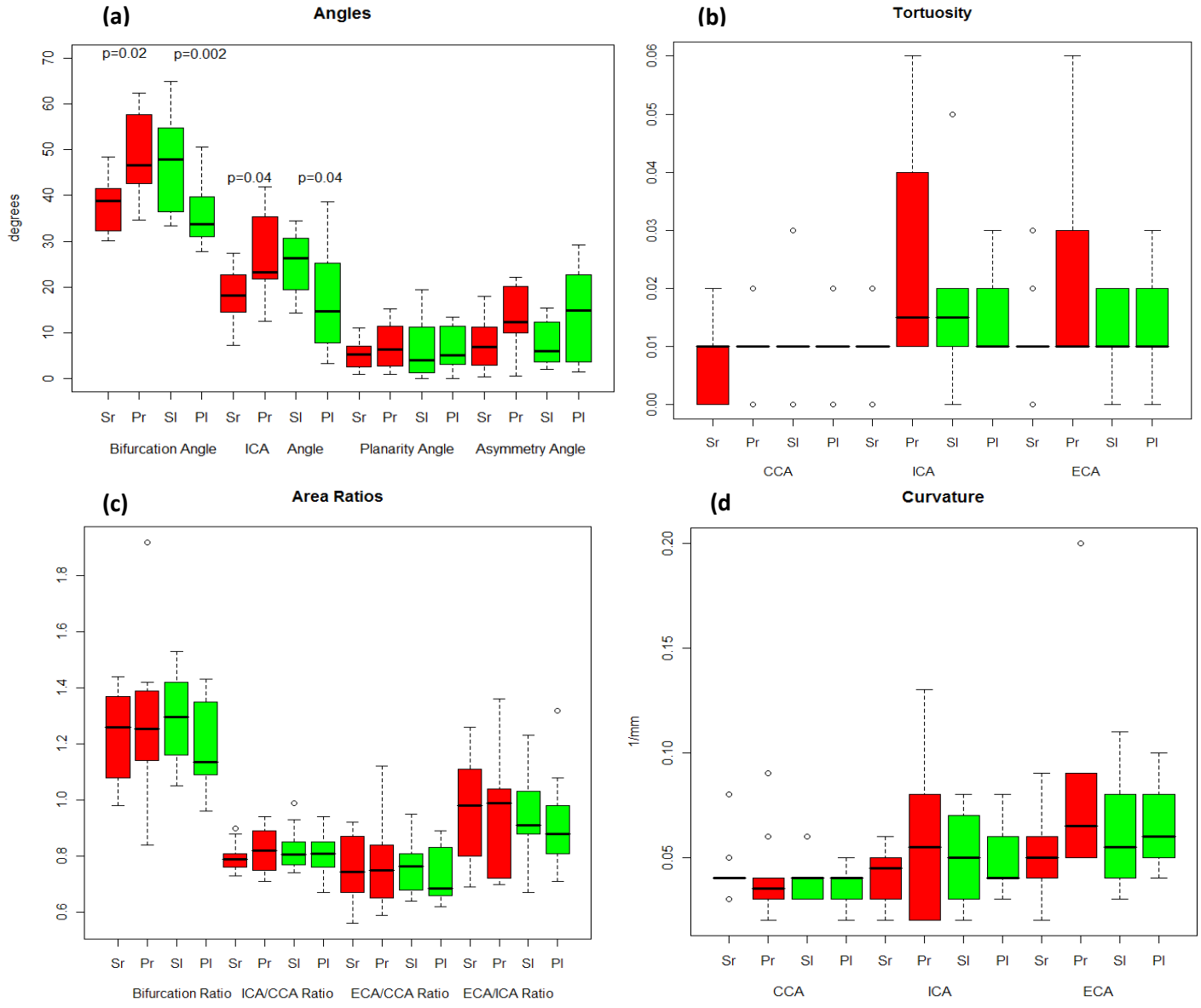

Figure 32: Box plots showing the median values horizontal line and interquartile ranges (IQR) of the geometric parameters estimated. Dashed lines connect the nearest observations within 1.5 of the IQR of the lower and upper quartiles. Unfilled circles indicate possible outliers with values beyond the ends of the 1.5xIGR. Data are shown for both right (red, r) and left (green, l) carotids in supine (S) and prone (P) head postures. p<0.05 values in the Wilcoxon signed-rank test between the two head postures are also shown.

The results for the geometric differences confirm previous findings [75, 102, 123, 159, 175, 178, 179] with regard to the considerable inter-individual variability in the geometry of the CB and also document that there is substantial variability in the geometric features of the LCB and RCB for the same individual. The results show that for all volunteers there are significant changes in the geometric parameters of the CB when the head is rotated. These changes are random and there is no predisposition to a specific direction of change for any of the parameters extracted. The variable pattern change demonstrated might be due to the considerable variability observed in the baseline geometry among subjects. Nevertheless, head rotation toward a specific direction can have a different effect on the same geometric feature for the two carotid arteries of the same volunteer. The fact that no significant correlation was seen in percentage changes either between different angles of the same bifurcation or between the same angle of the two carotids also predicates the variable effect that head rotation incurs on both the magnitude and the direction of angular change. In most volunteers, the results also show some curvature changes for the CCA as well as for the branches (ICA and ECA). In addition, the head rotation is not associated with a significant alteration in relevant area and diameter ratios, suggesting that any potential alterations in the local flow fields are not due to significant cross-sectional changes.

To conclude here, despite the reduced accuracy in the calculation of some of the geometric parameters, the results of the present study suggest that head rotation may cause significant variation in bifurcation, ICA, planarity, and asymmetry angle, as well as in vessel tortuosity and curvature. It seems, however, that these changes are random and depend on the geometry and elasticity of the whole neck arterial tree and there is no consistency regarding the direction and extent of change.

6.3 Quantification and Comparison of Geometric Parameters Between Supine Position and the Prone position with Rightward and Leftward Head Rotation

So far the study focused on two head postures and for further investigation on the geometric changes in the CB geometry the next step was to calculate the geometric

parameters for another head posture, the prone position with leftward rotation (~80^{o}). Two healthy young volunteers, from the group of ten, were imaged for the new head posture and the same procedure was followed as described earlier at paragraph 5.3. The changes in bifurcation, ICA, planarity and asymmetry angle for each head position with respect to the supine position is represented in the histograms in Fig. 33.

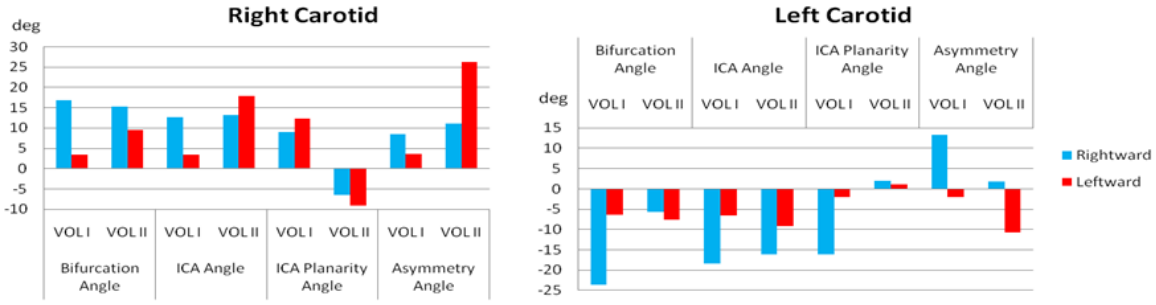

Figure 33: Angle difference values from supine head position. Data are shown for both carotids.

Figure 34 shows the quantitative results, of the two volunteers for the three investigated head postures and the qualitative results represented in Table 15.

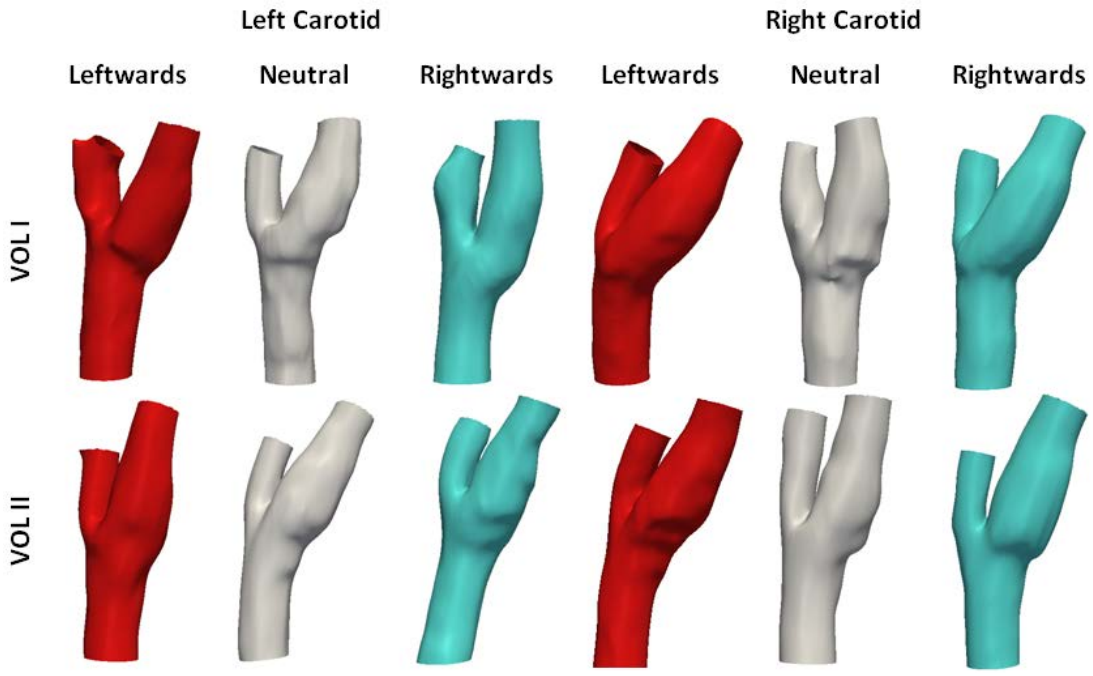

Figure 34: Reconstructed solid models for two volunteers of both carotid bifurcations for the three head postures, neutral (white), prone leftwards rotation (red) and prone rightwards rotation (cyan).

Table 15: Table of the actual value of each geometric parameter corresponding to the three postures.					
Geometric Parameter	**Head Position**	**Volunteer I**		**Volunteer II**	
		RC	**LC**	**RC**	**LC**
Bifurcation Angle	Rightwards	57.57	31.04	46.37	39.67
	Supine	40.74	54.65	31.09	45.34
	Leftwards	44.14	48.34	40.62	37.68
ICA Angle	Rightwards	35.73	7.86	28.93	12.69
	Supine	22.73	26.3	15.73	28.88
	Leftwards	26.21	24.2	33.65	19.71
Planarity Angle	Rightwards	15.23	3.16	2.73	3.2
	Supine	6.22	19.35	9.25	1.23
	Leftwards	18.62	12.85	0.1	2.32
Asymmetry Angle	Rightwards	13.3	15.31	11.48	14.28
	Supine	4.72	2.04	0.37	12.42
	Leftwards	8.27	0.06	26.68	1.74
Bifurcation Area Ratio	Rightwards	1.23	0.94	1.21	1.11
	Supine	1.34	1.21	1	1.14
	Leftwards	1.19	1.18	1.35	1.01
ICA/CCA Diameter Ratio	Rightwards	0.82	0.72	0.89	0.81
	Supine	0.76	0.82	0.77	0.85
	Leftwards	0.84	0.75	0.89	0.77
ECA/ICA Diameter Ratio	Rightwards	0.75	0.65	0.64	0.67
	Supine	0.87	0.74	0.63	0.64
	Leftwards	0.7	0.78	0.75	0.65
ECA/ICA Diameter Ratio	Rightwards	0.92	0.9	0.72	0.82
	Supine	1.14	0.9	0.82	0.75
	Leftwards	0.84	1.04	0.85	0.84

There are significant quantitative changes in bifurcation angle ICA angle, planarity angle and asymmetry angle, but not significant changes in curvature, tortuosity, area and diameter ratios with posture change. Fig. 34 shows that Bifurcation and ICA angles increase for bilateral head rotation for the right carotid and decrease for the left carotid.

The present results show that there are random and frequently significant changes in geometric parameters at the prone position with leftward or rightward head rotation. This is a frequent sleeping posture for many subjects and patients. The effects of such changes to the flow field in the carotid bulb and the development of carotid disease are unknown. The effects of such geometric changes on the structural integrity of carotid stents and the stress distribution on unstable plaque are also unknown and need to be investigated further.

6.4 Quantification and Comparison of Geometric Parameters of the Stenotic Carotid Bifurcation Between the Supine and the Prone Position with Leftwards Head Rotation

In this study, a group of four patients with atherosclerotic disease in the carotid arteries was investigated at two head postures, a) the supine and b) the prone with leftwards rotation up to 80^{o}, to investigate the level of stenosis and the changes in geometric parameters. All patients presented a stenosis hemodynamically moderate to significant at the origin of the left internal carotid artery (60-75 %).

Figure 35 shows from left to right the MIP image, the segmented model, the plaque distribution and the final smoothed model. It also represents the qualitative changes at the stenotic left ICA of volunteer III at the supine and prone head rotation postures.

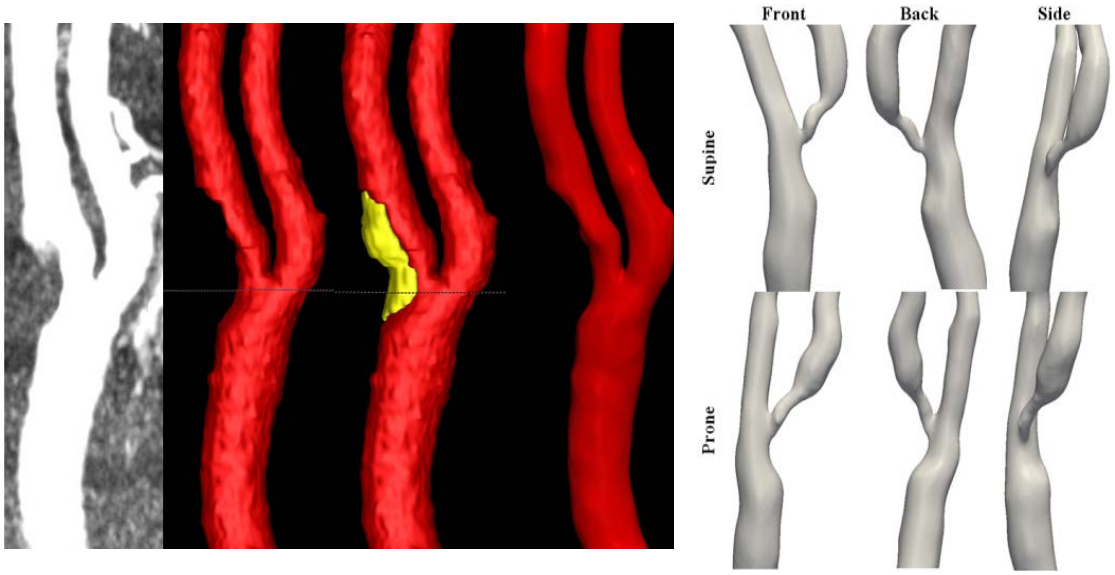

Figure 35: (Left) The MIP image, the segmented model, the segmented model with the plaque distribution, and the final smoothed model. (Right) The left carotid of volunteer III at the investigated postures (Supine, Prone) in three views (Front, Back, Side).

The quantitative results for the geometric parameters for all patient volunteers are represented in Fig. 36 and Table 16.

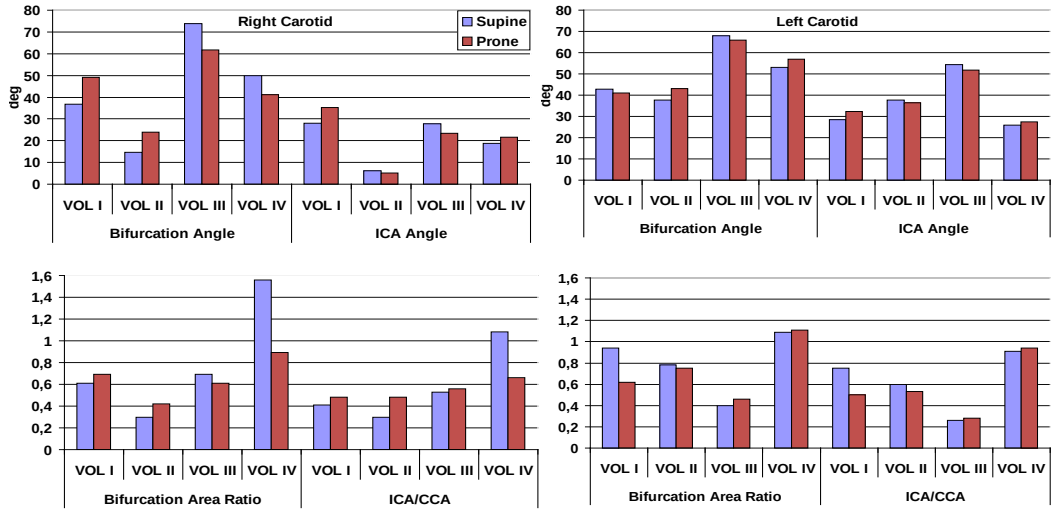

Figure 36: Quantitative results for the geometric parameters for the two investigated head positions. Data are shown for both carotids.

Table 16: Table of geometric parameters of right and left carotid.

				Right Carotid			Left Carotid			Both Carotids		
Geometric Parameter		n	Head Position	Median	Mean	Std	Median	Mean	Std	Median	Mean	Std
Angles	Bifurcation	4	neutral	36,67	41,73	30,01	47,91	50,39	13,37	42,82	46,68	20,27
		4	prone	49,22	44,90	19,27	43,01	49,93	13,85	46,12	47,42	15,26
	ICA	4	neutral	27,78	20,67	12,53	37,71	40,14	13,07	28,24	30,41	15,64
		4	prone	23,29	21,23	15,04	36,50	40,26	10,27	33,77	30,75	15,53
	ICA Planarity	4	neutral	22,90	17,09	14,56	2,55	3,09	1,98	3,92	10,09	12,05
		4	prone	13,62	15,10	6,60	5,93	7,27	4,97	11,07	11,18	6,76
	Asymmetry	4	neutral	18,38	13,30	9,68	38,05	30,87	14,58	18,89	22,09	14,67
		4	prone	15,07	16,47	4,06	29,99	30,60	7,00	22,48	23,53	9,28
Tortuosity	CCA	4	neutral	0,01	0,01	0,00	0,01	0,01	0,01	0,01	0,01	0,00
		4	prone	0,01	0,01	0,00	0,02	0,02	0,02	0,01	0,02	0,01
	ICA	4	neutral	0,01	0,03	0,05	0,02	0,02	0,02	0,01	0,02	0,03
		4	prone	0,01	0,02	0,02	0,03	0,03	0,02	0,02	0,02	0,02
	ECA	4	neutral	0,02	0,02	0,01	0,01	0,01	0,00	0,01	0,02	0,01
		4	prone	0,01	0,01	0,01	0,01	0,01	0,01	0,01	0,01	0,01
Curvature	CCA	4	neutral	0,05	0,05	0,02	0,06	0,06	0,01	0,06	0,05	0,01
		4	prone	0,06	0,07	0,03	0,09	0,08	0,04	0,08	0,08	0,03
	ICA	4	neutral	0,08	0,15	0,14	0,14	0,19	0,14	0,11	0,17	0,12
		4	prone	0,09	0,09	0,07	0,14	0,19	0,12	0,12	0,14	0,10
	ECA	4	neutral	0,12	0,11	0,02	0,08	0,10	0,03	0,10	0,10	0,02
		4	prone	0,07	0,08	0,01	0,09	0,10	0,02	0,09	0,09	0,02
AREA RATIOS	BF Area Ratio	4	neutral	0,61	0,53	0,21	0,78	0,71	0,28	0,65	0,62	0,24
		4	prone	0,61	0,57	0,14	0,62	0,61	0,15	0,62	0,59	0,13
	ICA/CCA	4	neutral	0,41	0,41	0,12	0,60	0,54	0,25	0,47	0,48	0,19
		4	prone	0,48	0,51	0,05	0,50	0,44	0,14	0,49	0,47	0,10
	ECA/CCA	4	neutral	0,64	0,59	0,11	0,62	0,62	0,04	0,63	0,60	0,08
		4	prone	0,54	0,55	0,12	0,62	0,64	0,04	0,62	0,60	0,09
	ECA/ICA	4	neutral	1,50	1,45	0,21	1,07	1,37	0,74	1,36	1,41	0,49
		4	prone	0,96	1,09	0,27	1,29	1,56	0,54	1,25	1,33	0,46

The changes of calculated cross sectional areas for the two head postures at the specific locations CCA3, ICA5 and ECA5 are represented in Table 17. Data from the carotid artery with the most prominent stenosis are presented for all patients ("min lumen" refers to the minimum measured lumen area in the ICA), along with data from the right carotid of the healthy volunteer obtained at the supine position.

Table 17: Surface Areas (mm^2)
Comparison areas at the two head postures at specific places

		Min Lumen	CCA3	ICA5	ECA5
Vol I	Supine	9.9	36.3	16.3	16.5
	Prone	8.4	35.5	10.0	14.2
Vol II	Supine	12.1	45.5	24.1	11.8
	Prone	10.6	52.7	27.8	11.9
Vol III	Supine	1.9	26.1	2.4	10.8
	Prone	2.2	26.8	2.2	10.4
Vol IV	Supine	11.0	26.9	25.1	10.0
	Prone	11.7	26.5	25.5	8.5
Healthy Vol.	Original	-	35.7	22.2	17.6
	Reprod.	-	36.8	24.0	20.6

The results from the patient study suggest that there are also changes in geometric parameters at the prone position with leftward head rotation. This is a frequent sleeping posture for many subjects and patients. There is not yet evidence of significant lumen area change at the stenotic location with head rotation.

Part III: Computational Fluid Dynamics (CFD)

Chapter 7:

Mesh Construction and CFD

7.1 Mesh Generation Methodology for Arterial Models

The generation of the mesh is the procedure where the 3D geometry domain is subdivided by discretization, into a numerical grid of finite subdomains, in our case, the control volumes. Basically, at these discrete locations, the solution of governing equations is performed and the various fluid variables are calculated [118]. The finite volume method (FVM) that was used in this study, supposed first the integration of the governing equations over the cell-volume to obtain the integral form of the equations, and after the summation to derive the required equations [180]. In FVM the mass and momentum equations are decoupled. Throughout this study the pressure-based segregated solver was used which means that the equations are solved sequentially taking into account one variable field in each step. The pressure-implicit with splitting of operators (PISO) algorithm was used to determine the pressure and velocity components. For the discretization the convective Navier-Stokes terms were discretized using a second-order upwind scheme. A more detailed description will follow in paragraph 7.5.

7.1.1 Types of Mesh Elements

There are many different types of mesh elements and the choice of each depends on the geometry and how the problem will be solved. The most common 3D elements are the Tetrahedron (“tet”), the pyramid, the hexahedron (“hex”) which is prism with quad base and the wedge which is prism with tri base. The 2D elements are triangle (“tri”), and the quadrilateral (“quad”). Figure 37 represents the shapes of most common 2D and 3D elements and defines the various topological properties for 2D and 3D meshes [181].

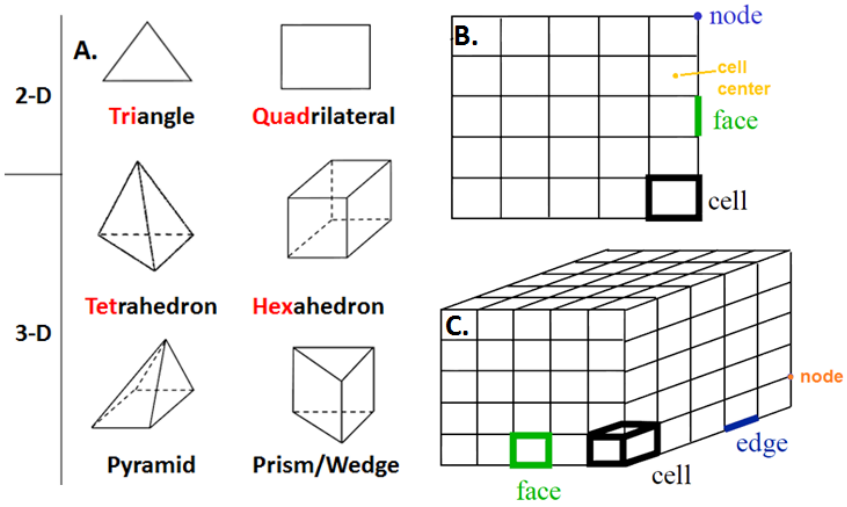

Figure 37: A. 2D and 3D elements shapes, B. 2D mesh, C. 3D mesh.

7.1.2 Type of Meshes

Several types of numerical grids exist and the selection depends of the complexity of the physical problem each time. In most biomedical problems, unstructured meshes are used. Some type of meshes are represented below:

a. **The structured mesh** is characterized by regular connectivity and has the property that the grid lines cross each other only once. This allows the lines to be numbered consecutively. Also, any mesh point is uniquely identified and has four neighbors in 2D or six in 3D which the indices of each neighbor differs by ±1. The structured mesh is equivalent to a Cartesian grid and an example is shown in Fig. 38. The structured meshes can be used only for simple geometries [118].

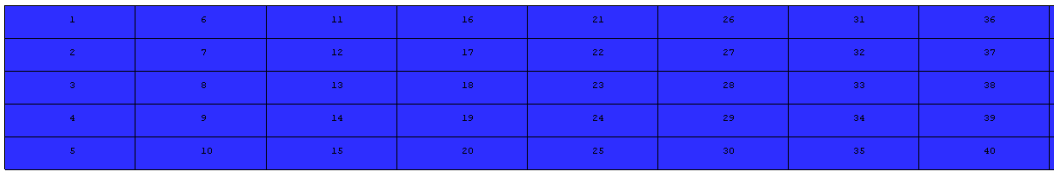

Figure 38: A 2D structured, orthogonal mesh for flow simulations in a pipe. Element identification numbers within each element.

b. **The block-structured grid**. Here, the blocks are large segments of the geometry domain and within each block a structured mesh is defined. Figure 39A shows an example of a 3D block-structured grid. This type is used in complicated shapes.

c. **The unstructured mesh.** The use of that type of mesh is preferred as it fits in any geometry and for that reason it is chosen for complex geometries. The basic difference from structured meshes is the ordering of the nodes. The mesh is described as unstructured if the indices of each neighbor node is different by ±1 [182]. Figure 39B below shows a 2D unstructured grid.

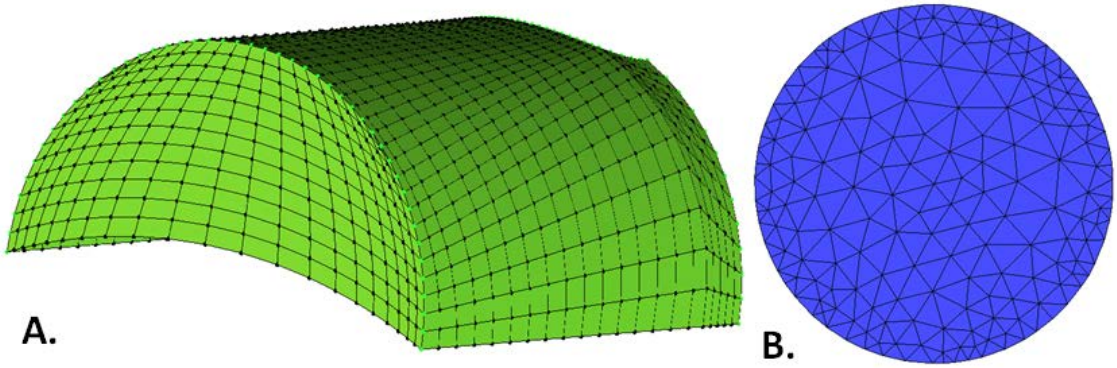

Figure 39: A. The 3D block-structured mesh for flow simulations in a pipe. B. The 2D unstructured mesh.

Although, structured grids reduces run times and have one order of magnitude less grid convergence index, the major number of studies for bifurcation and complex geometries use unstructured meshes due the complexity and effort to construct this type of grid [183].

7.2 Mesh Generation

All the meshes generated for the purposes of this study were constructed by ICEM-CFD v12.1 (Ansys Inc.). For accurate and reliable CFD results, it is essential to have a fine mesh with sufficient resolution to capture all flow features, and the characteristics of the grid related with the quality are mesh spacing, skewness, smoothness and aspect ratio [184]. For that reason, the first thing in this section is the description of two mesh quality criterions that were used to ensure that the mesh is fine and the results accurate. These significant criteria for mesh quality metrics are:

a. Normalized equilateral skewness: represents the normalized measure of skewness and can range between 0 (best) and 1 (worst). Values 0 - 0.25 are excellent, 0.25 - 0.5 good, and 0.75 - 1 indicate poor quality [185, 186].

$$Skewness = \max\left(\frac{\theta_{max}-\theta}{180-\theta}, \frac{\theta-\theta_{min}}{\theta}\right) \quad (7.1)$$

where: θ_{max} and θ_{min} the largest and smallest angle in face or cell
θ=60 (triangle, hexa), θ=90 (square, tetra) the angle for equiangular face or cell

b. Aspect ratio: this quality criterion defined as the ratio of the length of the longest edge to the shortest. The ideal aspect ratio is equal to one, and represents the equilateral triangle and square.

The computational domain was spatially discretized in around $8 \cdot 10^5$ mixed type elements, with higher grid density in the vicinity of the bifurcation and a viscous layer adjacent to the wall. This layer initiated at a distant of $0.01D_{ICA}$ from the wall, and the total height was $0.11D_{CCA}$. This layer near the wall, and the sub-layers within, are presented in Fig. 40.

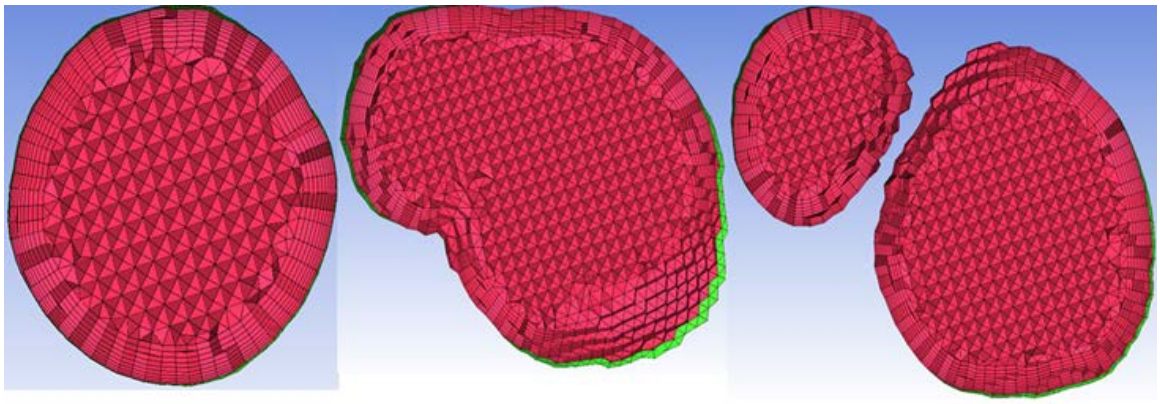

Figure 40: Fine mesh with average cell spacing 0.2 mm. From left to right, at inlet, before CB, just after CB

7.3 Independence Study

A systematic grid study is required to ensure that the grid resolution is sufficient to obtain accurate results in such a complex geometry. A systematic time step and grid size converge study has to be conducted for each patient-specific model [187] to ensure grid and time step convergence, resulting in a very time consuming procedure. On a single characteristic case the study was performed and the results were applied to all cases as the topology was the same and thus flow features in all cases were expected to be similar. On this particular case three meshes was generated with increasing mesh density (coarse, medium, fine) (Fig. 41, Table 19) and three different time steps (Δt)

were used for the simulations (Table 18). Three monitor points were placed inside the carotid bulb (Fig. 42), where the flow is characterized as complex. The results for the cycle averaged pressure (p) and velocity (u) at these points were calculated at the third flow cycle. The relative error between the computed p and u values became negligible (less than 1.65 %) between medium to fine meshes and medium and smallest time steps. The results for the third monitor point (MP3) are summarized in Table 18.

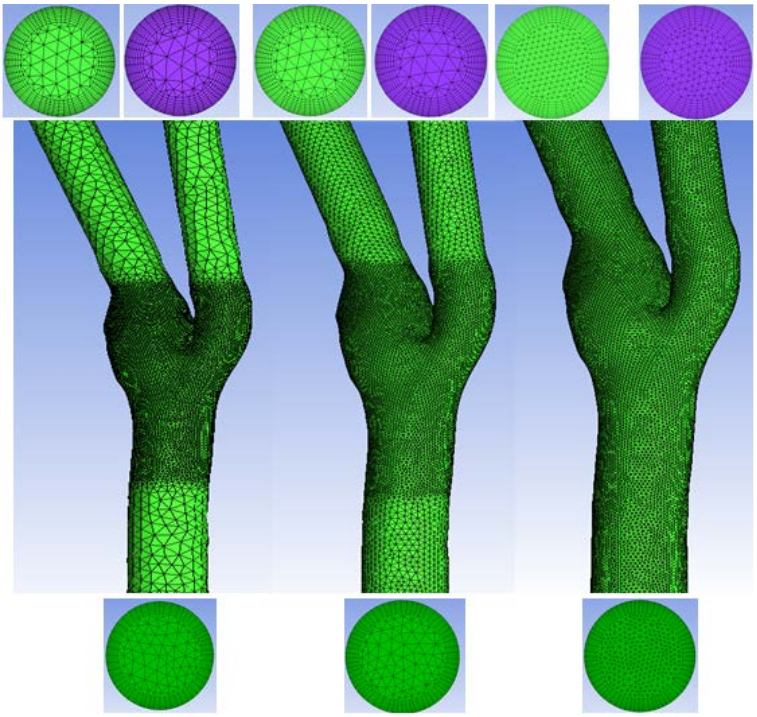

Figure 41: Three different size meshes. From left to right, the coarse, the medium and the fine.

Therefore a mesh size of ~$7.9 \cdot 10^5$ and a time step of $1.97 \cdot 10^4$ s were considered sufficient and were used in all models. A higher grid density (25% reduction in element size) was only applied in the vicinity of the CB and a refined viscous layer was added adjacent to the wall.

The relative error between the subsequent meshes is calculated by [188]:

$$\%\, error = \left|\frac{\varepsilon_{fine} - \varepsilon_{medium}}{\varepsilon_{fine}}\right| \cdot 100\ \% \qquad (7.2)$$

where % *error* the (%) relative error, ε the result for p and u at the same monitor point

Table 18: Number of Elements and Nodes				
Mesh		Coarse	Medium	Fine
Total Elements		482869	790013	1935054
Tetrahedral Elem.		216736	318360	764826
Prismatic Elem.(penta_6)		237227	421943	1049993
Total Nodes		162636	277365	683739
Max Element, Bif		1.65, 1.4	0.7, 0.42	0.63, 0.6
Velocity (mm/s) and Pressure (Pa) at Peak Systole				
Time Step (10^{-4}s)	3.95	0.45/3.24	0.47/2.40	0.48/1.97
	1.97	0.45/3.0	0.47/2.25	0.48/1.92
	1.32	0.44/2.74	0.47/2.02	0.48/1.82

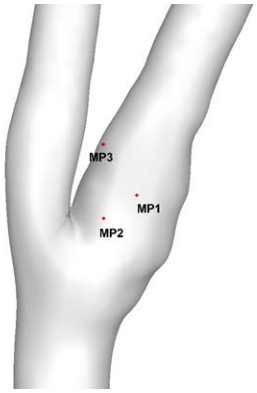

Figure 42: The three monitor points inside ICA bulb.

The table below represents the total number of nodes, the number and type of volume elements, the average node spacing (Max Element) and the minimum node spacing (Bif) for each constructed mesh.

Table 19: Characteristics of three meshes			
Mesh	Coarse	Medium	Fine
Total Elements	482869	790013	1935054
Tetrahedral Elem.	216736	318360	764826
Prismatic Elem.(penta_6)	237227	421943	1049993
Total Nodes	162636	277365	683739
Max Element, Bif (mm)	1.65, 1.4	0.7, 0.42	0.63, 0.6

Figure 43 represents the pressure at MP3 throughout the 3rd simulation cycle for the three meshes. The differences are smaller between medium and fine mesh as depicted below.

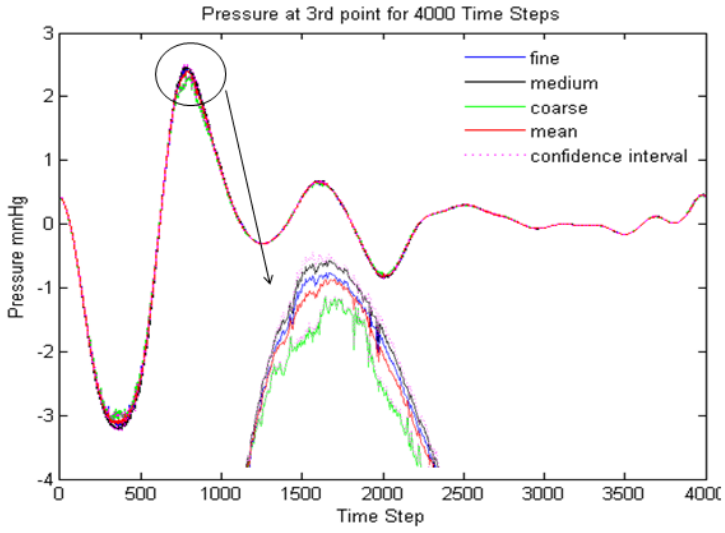

Figure 43: Mesh independent study showing the pressure convergence.

Figure 44 show the best convergence of velocity for fine and medium meshes.

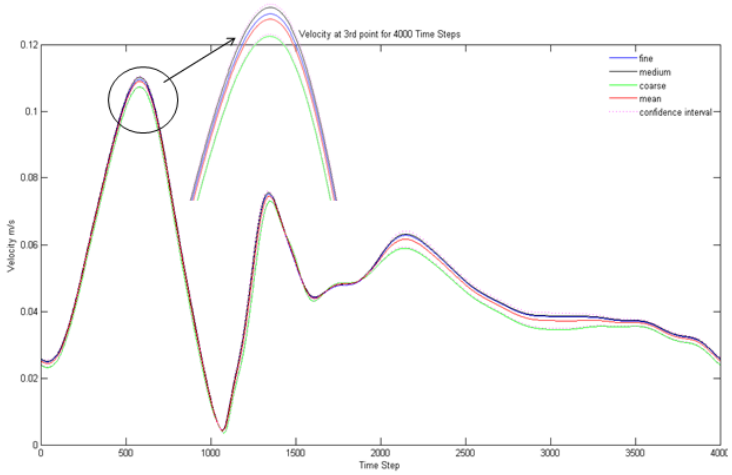

Figure 44: Mesh independent study showing the velocity convergence.

7.4 Mesh Generations for an Aneurysm

For the purposes of CFD simulations on a giant aneurysm it was necessary to construct a fine mesh from the surface file. The strategy that was followed was pretty similar as for CB meshes construction. In more detail, the computational domain (excluding flow extensions) was discretised with ~$2.1 \cdot 10^6$ hybrid, linear elements with an average cell center spacing of 0.25 mm. Near-wall layers of prism elements were used throughout the domain for boundary layer refinement with a 10^{-2} D_{inlet} distance of the center of the first element from the wall. Triangles were used to discretise the surface of the aneurysm and quads for the extensions. Pyramid and tetrahedral elements were used to fill the core of the computational domain in the aneurysm. The o-grid method was used to generate layers of hexahedral elements in the flow extensions.

For the independence study, three different meshes were constructed with mean cell center distance 0.3, 0.25, 0.18 mm and number of elements ~$1.4 \cdot 10^6$, ~$2.1 \cdot 10^6$ and ~$4 \cdot 10^6$ respectively. The results from the steady flow computations for the maximum flow case (Q=11.42 mL/s) indicated a maximum difference of less than 1% in the computed centerline pressures between the medium and fine mesh. To ensure the time

step (Δt) independence, a $\Delta t=1.25\cdot10^{-4}$ s and a $\Delta t=2.5\cdot10^{-4}$ s were selected. The latter time step was sufficient since the max difference in pressure was again less than 1%.

7.5 Boundary Conditions

To be able to perform simulations on the constructed meshes, it is necessary to apply the appropriate boundary conditions on the arterial wall, the outlet and the inlet regions. For all simulations in this study the rigid wall assumption was applied, which is a commonly accepted practice, and a reasonable approximation for large arteries. The blood was modeled as a Newtonian fluid with a constant density of 1050 kg m^3 and viscosity of 3.5 cP, as these values are commonly accepted for large arteries where the shear rates are above 100 s^{-1} (Fig. 45). A constant 0.65/0.35 ICA/ECA flow split was applied and the no-slip boundary condition was imposed on the vessel wall, i.e. the velocity of the fluid is equal to the wall velocity which is zero. The impact of these assumptions on numerical computations has been assessed in several works [189-195]. Marshall *et al.* found a ratio 0.70/0.26 ICA/ECA in a study including 14 CB of healthy young volunteers [196]. For mild stenosis (≤ 65 %) the outflow ratio remained constant 0.64/0.35 ICA/ECA and similar to the values of young healthy volunteers [197].

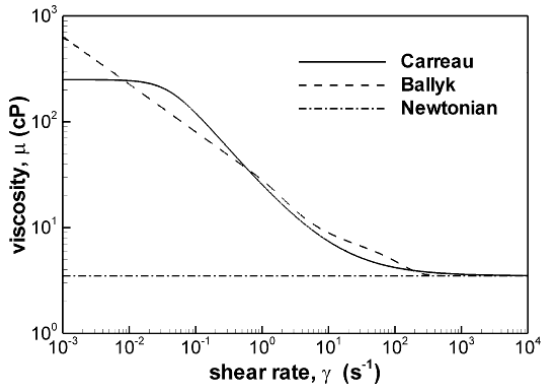

Figure 45: The viscosity of human blood for three different hemorheology models (from [189] without permission)

Although the concept of fully developed flow in CCA is dominant in biomechanical simulations, and was applied throughout this study, a recent study of Manbachi *et al.* found that this concept may be the exception rather than the rule [198]. For the purpose of this study, in order to prescribe fully developed flow it is necessary to apply

cylindrical flow extensions at the inlet and two outlets with the use of the VMTK software. When the flow is fully developed, the velocity profile remains constant and the pressure drops linearly as represented in the Fig. 46. The length of the extensions was calculated from formula (7.3), based on the approximation relation for the entrance length for steady laminar rigid pipe flow as found in any Fluid Mechanics texbook [115]. He and Ku showed that for low Womersly numbers (*α*), the maximum entrance length for pulsatile flow was very closed as in the steady flow [199]:

$$\frac{L_e}{D_i} \approx 0.06Re \tag{7.3}$$

For the idealized Poiseuille flow the entrance length is shorter and given by [116]:

$$\frac{L_e}{D_i} = 0.04Re \tag{7.4}$$

where L_e the sufficient length to fully developed velocity profile
D_i the inlet diameter
Re the Reynold number

$$Re = \frac{u\,D_i}{\nu} = \frac{\rho\,u\,D_i}{\mu} \tag{7.5}$$

where *u* the average inflow velocity
ν, μ the kinematic and dynamic viscosity of blood and *ρ* the blood density

Re number is the ratio of the inertial forces to viscous forces and a parameter that predicts if flow is laminar (Re < 2000) or turbulent (Re > 4000). For Re numbers between 2000 and 4000 the flow is in transition, and is called unstable [115].

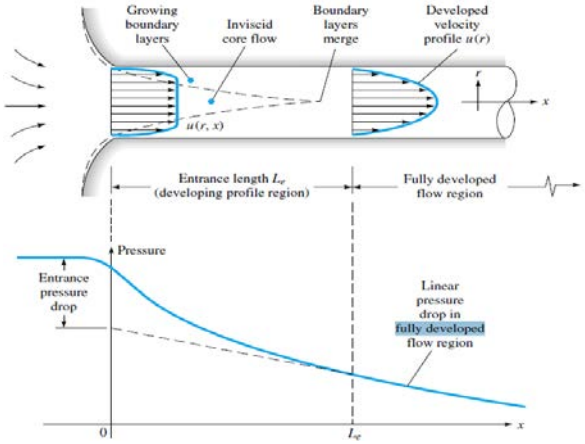

Figure 46: Entry developing velocity profile and pressure changes in a tube. The fluid near the walls influenced by the no-slip B.C. (figure from [115] without permission)

The effect of inlet length on normal CCA bifurcation was studied extensively by the Hoi *et al.* [200]. They performed simulations on twelve healthy CCA and investigated inlet lengths of one, three, five and seven inlet diameters. They recommended at least $3D_{inlet}$ for fully developed inlet profile. Furthermore, a study of Moyle *et al.* pointed out that giving sufficient length of entrance in realistic models, the simplification of fully developed axial flow may be imposed without penalty [193]. Furthermore, the traction-free boundary conditions were imposed for ICA and ECA outlets.

For the inlet boundary conditions, at the beginning of this study, the parabolic velocity profile was used, more widely known as Poiseulle flow. This velocity profile defined:

$$u(r) = u_{max}\left(1 - \frac{r^2}{R^2}\right) = 2u_{mean}\left(1 - \frac{r^2}{R^2}\right) \tag{7.6}$$

where u is the velocity, *r* is the radial distance, and *R* the radial of the circulate inlet.

The next step was the use of an MRI measured flow waveform, as a pulsatile flow boundary condition reflects the reality better. A transient solution for the velocity profile for oscillatory flow was proposed by Womersley in 1955 [201]. This solution was used as the inlet boundary condition for all the simulations for this study. The analytic mathematical solution, by Holdsworth *et al.* [202] for the pulsatile velocity flow in a straight, rigid tube is defined:

$$u(r,t) = Real\left[u_{mean,n}\left(\frac{J_0\left(a_n i^{-3/2}\right) - J_0\left(a_n r i^{-3/2}\right)}{J_0\left(a_n i^{-3/2}\right) - \frac{2J_1\left(a_n i^{-3/2}\right)}{a_n i^{-3/2}}}\right)e^{in\omega t}\right] \tag{7.7}$$

where: J_0 and J_1 the 0th and 1st Bessel function of the first kind
r the radial position normalized to the vessel radius *R*
$i = \sqrt{-1}$
$a_n = R\sqrt{\frac{n\omega}{\nu}}$ the Womersley number of the nth harmonic

The Womersley number (α) is the ratio of the unsteady forces to the viscous forces and for low α the velocity profile is parabolic as the viscous forces are dominant. When α is above ten, the velocity profile is flat due to the dominant unsteady inertia forces [52].

For the ideal case of long, straight, constant cross-section tube, the flow may be assumed fully developed. For that reason, extensions of sufficient length apply at CCA, ICA and ECA. In the absent of fully developed flow, and when the tube is curved, the velocity profile is skewed toward the outer wall under the influence of centrifugal effects. Furthermore, secondary flows are developed, as vortices with flow move toward the outer wall [52, 203]. The parameter relating skewness, is the Dean number which is defined:

$$De = \frac{1}{2} Re \left(\frac{r}{k}\right)^{0.5} \tag{7.8}$$

where, *Re* the Reynold number, *r* the tube radius and *k* the radius of curvature

The Dean number is the combination of *Re* number and the normalized tube radius to curvature. High curvature leads to high *De* numbers and strong velocity profile skewness that may separate the flow.

Finally, for two volunteers, the realistic inlet boundary conditions were imposed for both carotids and for two investigated head postures. The velocity waveform is a time-dependent signal which is reconstructed from PC-MR images that provides the blood flow rate, using the Fourier series. The methodology is described in more detail in the next paragraph. Figure 47 depicts the velocity waveform from a volunteer showing the characteristic points on it.

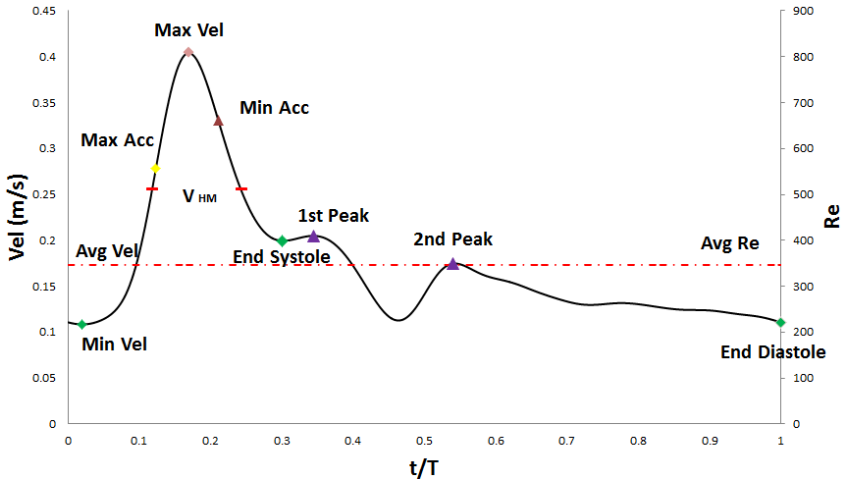

Figure 47: Average velocity waveform from CCA. Min Vel: Minimum diastolic velocity, V HM: V_HM=(V_MAX-V_MIN)/2+V_MIN, Max Acc: Maximum acceleration, Max Vel: Maximum systolic velocity, Min Acc: Minimum acceleration, 1st, 2nd Peak:

7.5.1 Fourier Analysis

The estimation of the blood flow waveform was achieved using PC-MR images from LCB and RCB, at the level $5D_i$ below CB. The blood flow is pulsatile, and therefore is a periodic function with period (T). Since it is a periodic function, the Fourier series (7.9) can be used to expand this function into an infinite sum of sines and cosines. This is the Fourier-decomposed technique, to break up an arbitrary periodic function into a set of appropriate simple terms, the Fourier coefficients. The periodic function depends on the fundamental frequency (ω_0 heart rate in rad/s) and the time (t).

$$f(t) = a_0 + \sum_{n=1}^{N}(a_n \cos(n\omega_0 t) + b_n sin(n\omega_0 t)), \qquad n = 0,1,2,\ldots \tag{7.9}$$

$$\omega_0 = 2\pi f = \frac{2\pi}{T} \tag{7.10}$$

where $f(t)$ is the signal in the time domain
n is the nth harmonic
α_n, b_n are the Fourier coefficients which calculated by the followed formulas:

$$a_0 = \frac{1}{T}\int_0^T f\,(t)dt \tag{7.11}$$

$$a_n = \frac{2}{T}\int_0^T f\,(t)\cos(n\omega_0 t)\,dt \tag{7.12}$$

$$b_n = \frac{2}{T}\int_0^T f\,(t)\sin(n\omega_0 t)\,dt \tag{7.13}$$

The complex form of Fourier series by using Euler's identity to convert the sines and cosines to exponentials is represented below:

$$\cos(n\omega_0 t) = \frac{1}{2}(e^{in\omega_0 t} + e^{-i\omega_0 t}) \tag{7.14}$$

$$\sin(n\omega_0 t) = \frac{1}{2i}(e^{in\omega_0 t} - e^{-in\omega_0 t}) \tag{7.15}$$

Substituting (6.15) into (6.9)

$$f(t) = 0.5\alpha_0 + \sum_{n=1}^{N}(0.5(a_n - ib_n)e^{in\omega_0 t} + 0.5(a_n + ib_n)e^{-in\omega_0 t}) \tag{7.16}$$

Figure 48 shows the first seven and the thirteen harmonic related with the original velocity waveform which show that the first 13 harmonics are a sufficient approximation for the original waveform. The methodology followed to calculate the Fourier coefficients for this study is represented in Appendix III.

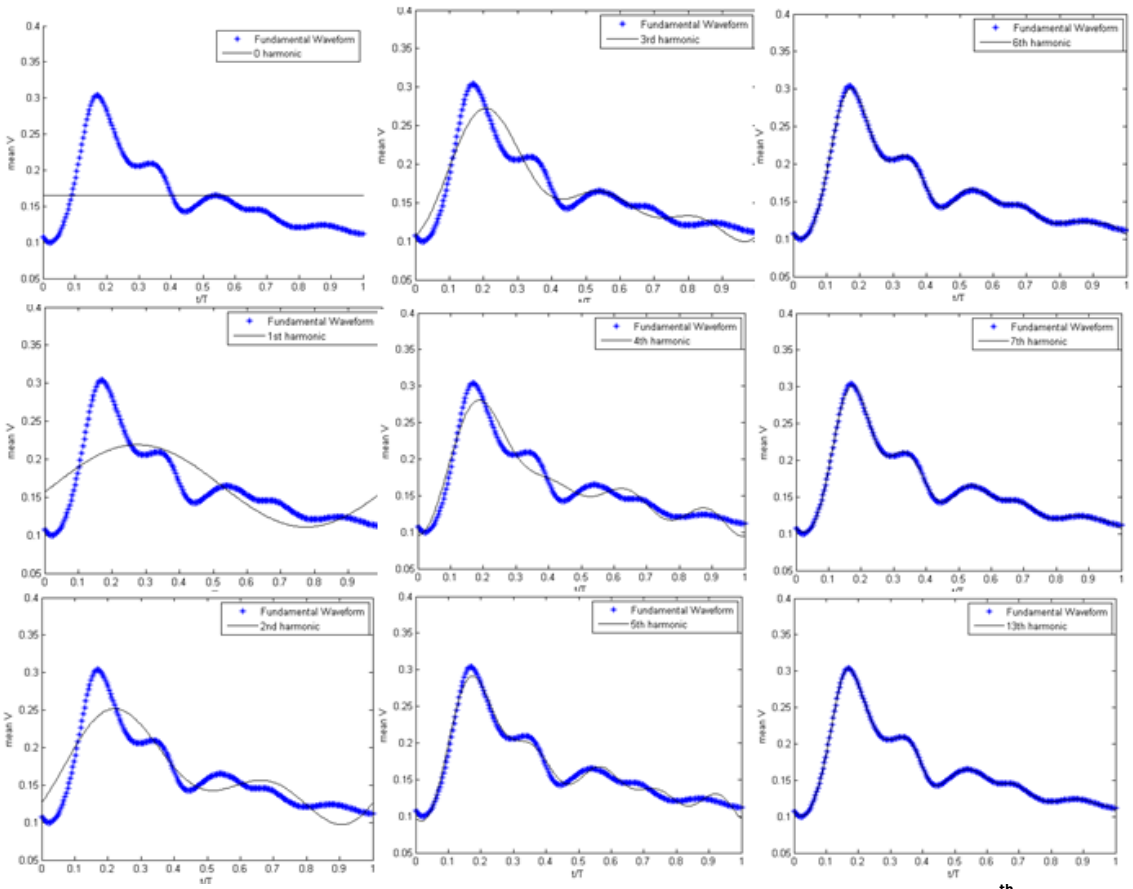

Figure 48: The total average velocity waveform (blue) and the summation of first 7 and the last 13th harmonic.

7.6 Solution of the Governing Equations

The governing equations described in paragraph 3.4 needed to be solved numerically, since they are not analytically solvable, except in special cases. First, the spatial discretization was performed as described in section 7.2 and the appropriate boundary conditions were imposed as defined in paragraph 7.5. The Fluent v12.1 (Ansys Inc.) software was used to solve the Navier-Stokes equations in the computational domain. The finite volume method was used as described earlier in 7.1. For this study, the Navier-Stokes equations were simplified for unsteady, incompressible flow as:

Continuity: $$\nabla \cdot \boldsymbol{u} = \mathbf{0} \tag{7.17}$$

Momentum: $$\rho\left(\frac{\partial \boldsymbol{u}}{\partial t} + \boldsymbol{u} \cdot \nabla \boldsymbol{u}\right) = -\nabla p + \mu \nabla^2 \boldsymbol{u} \tag{7.18}$$

where **u** and p is the blood velocity and pressure
ρ and μ the blood constant density and viscosity

For all simulations performed, Fluent was used as the finite volume commercial software to formulate and solve the governing equations. A second-order interpolation scheme was applied for pressure and a second-order upwind discretization scheme for the momentum equations. For the pressure-velocity coupling, the Pressure-Implicit with Splitting of Operators (PISO) algorithm was used. The PISO scheme is part of the Semi-Implicit Method for Pressure-Linked Equations (SIMPLE) family of algorithms. In more detail, Fluent provides the option to choose among several pressure-velocity coupling schemes, such as [204]:

1. SIMPLE: uses a relationship between **v** and p corrections to obtain the pressure field.
2. SIMPLEC (SIMPLE-Consistent): is an improvement of SIMPLE algorithm.
3. PISO: is also part of SIMPLE family and is based on the higher degree of the approximate relation between the correction for **v** and p.
4. Coupled: solves the momentum and pressure-based continuity equations together.

The description of construction of 3D surface models from MR images and therefore the construction of the corresponding meshes has been described so far. The next step of this study is to perform the numerical simulations.

Chapter 8:

Effect of Head Posture on Carotid Bifurcation Hemodynamics

The effect of head posture on the RCB and LCB of two healthy volunteers was investigated here. Notable geometric changes due to the head rotation were observed, and the next step was to perform numerical simulations in three different head postures: a) the supine position, b) the prone with rightwards rotations up to 80^o and c) the prone with leftwards rotations up to 80^o. Using MR imaging and from image-based surface models, it was able to estimate the morphological differences for the two investigated head postures compared to the supine posture and the results are represented in Table 20. The results obtained from this study and the content of this section was published in [205].

Geometric features related to the CB such as the bifurcation angle, the ICA angle, the bifurcation area ratio, the ICA/CCA, ECA/CCA and ECA/ICA area ratios were computed based on the clipped CB geometries at the CCA3, ECA5 and ICA5. The definition of these parameters can be found in paragraph 6.1. According to the results of Table 20, changes in the bifurcation and ICA angles due to head rotation are well above the reproducibility uncertainty and thus significant.

Table 20: Geometric parameters for the three different head postures (S-Supine, LR-Leftwards, RR Rightwards) and differences between LR and N (LR-S) and RR and S (RR-S).

Geometric Parameter			Volunteer I		Volunteer II	
			LCB	RCB	LCB	RCB
Angles (degrees)	Bifurcation Angle	LR-S	-6.3±0.54	3.4±0.54	-7.7±0.54	9.5±0.54
		S	54.65	40.74	45.34	31.09
		RR-S	-23.6±0.54	16.8±0.54	-5.7±0.54	15.3±0.54
	ICA Angle	LR-S	-2.1±1.19	3.5±1.19	-9.17±1.19	17.9±1.19
		S	26.3	22.73	28.88	15.73
		RR-S	-18.4±1.19	12.7±1.19	-16.2±1.19	13.2±1.19
Area Ratios	Bifurcation Area Ratio $(ICA_5+ECA_5)/CCA_3$	LR-S	-0.03±0.06	-0.15±0.06	0.13±0.06	0.35±0.06
		S	1.21	1.34	1.14	1.0
		RR-S	0.27±0.06	-0.11±0.06	0.03±0.06	0.21±0.06
	ICA_5/CCA_3	LR-S	-0.07±0.02	0.08±0.02	-0.08±0.02	0.12±0.02
		S	0.82	0.76	0.85	0.77
		RR-S	-0.1±0.02	0.06±0.02	-0.04±0.02	0.12±0.02
	ECA_5/CCA_3	LR-S	0.04±0.03	-0.17±0.03	0.01±0.03	0.12±0.03
		S	0.74	0.87	0.64	0.63
		RR-S	-0.1±0.03	-0.12±0.03	0.03±0.03	0.01±0.03
	ECA_5/ICA_5	LR-S	-0.1±0.01	-0.1±0.01	0.1±0.01	0.03±0.01
		S	0.9	1.14	0.75	0.82
		RR-S	0.0±0.01	-0.22±0.01	0.07±0.01	-0.1±0.01

Reproducibility uncertainty reported after ± symbol

In most cases, but not all, the effects of head posture change on cross sectional area ratios for CCA, ICA and ECA are considered notable. In more detail, for the RCB, an increase between 3^o and 17^o of the bifurcation angle and 3^o and 18^o of ICA angle was observed. These are significant changes considering the mean values, ~42^o and ~23^o respectively.

From the already existent 3D models the corresponding fine meshes constructed followed the procedure described above in section 6.2. A total of twelve meshes were used for CFD simulations to estimate the local hemodynamics. The prescribed PC-MRI measured inlet velocity waveform that was used for all simulations is represented below in Fig. 49. The CFD simulations were performed using Fluent and the blood was modeled as an incompressible Newtonian fluid with $\rho=1050\ kg/m^3$ and $\mu=3.5\ cP$. Paragraphs 7.5 and 7.6 describe in more detail the choice of boundary conditions and the strategy followed for the numerical solutions.

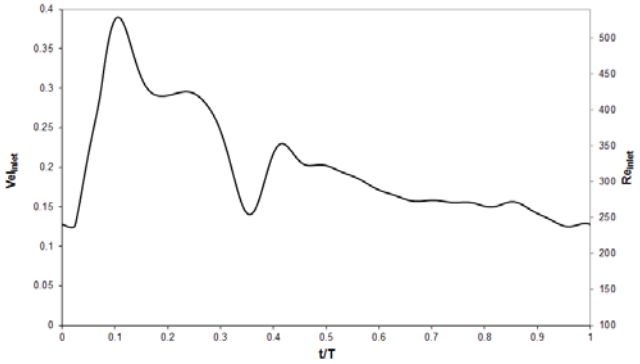

Figure 49: PC-MRI measured flow waveform imposed as inlet boundary condition for all simulations.

To quantify the impact of the local hemodynamics on the arterial wall, the calculation of the area exposed to unfavorable hemodynamics based on threshold values was essential. The threshold for TAWSS was set to 0.4 Pa based on the study by Malek *et al.* [8]. The selected crucial threshold values for high OSI are: 0.145, 0.238 and 0.3. The first two values were taken from Lee et al. [164] and the last one was added arbitrarily to assess the sensitivity of the results to the threshold. Lee *et al*. categorized their results for endothelial shear stress based on percentile group thresholds (n=50 CB) following the approach of Stone *et al.* [206]. For nOSI, a threshold value equal to 1.125 was calculated based on the respective thresholds for OSI and TAWSS and by normalizing the

TAWSS threshold with the physiological level of TAWSS in arteries, which is 1.5 Pa based on the study by Malek *et al*. [8]. The same process was used to compute threshold values for RRT and the values are 5.29, 7.14 and 9.35. The results of the impact of atherosclerotic burden associated with head posture changes are presented in Table 21.

The area exposed to unfavorable hemodynamics was calculated by dividing the exposed area to the total CB wall surface area clipped at CCA3, ECA5 and ICA5 sections as reported in Lee *et al.* [164]. The area calculations were done by Tecplot 360 v.11 (Tecplot, Inc.), performing integration over the wall elements domain. More details can be found in the user's manual [207]. Furthermore verification was done using Fluent and the compared results show that the area values are in agreement.

Reproducibility Study

To assess the significance of the results and to estimate the uncertainty in the followed methodology, from MR imaging to the hemodynamic parameters calculation, the whole process was repeated for volunteer II with the head in the supine position. The MR imaging was repeated within one month from the original scan session using exactly the same setup and imaging protocol. Imaging processing of the obtained images was performed by the same individual in a similar manner to the original procedure. The absolute value of the difference in morphologic and hemodynamic metrics between the two measurements of volunteer II is presented in Tables 20 and 21 herein (values to the right of symbol ±) as an estimation of the whole process reproducibility.

In almost all cases considered, there are differences in the magnitude of the respective metric between the supine and leftwards and rightwards head postures. Considering the whole process reproducibility, these changes represent a significant alteration in hemodynamic burden when the wall is exposed to nOSI and OSI.

Table 21: Area exposed to unfavorable hemodynamics normalised by the total surface area bounded by CCA3, ECA5, ICA5					
		Volunteer I		Volunteer II	
		LCB	RCB	LCB	RCB
WSS<0.4 (Pa)	LR-N	-0.01±0.062	-0.1±0.062	0±0.062	0.03±0.062
	N	0.28	0.36	0.29	0.27
	RR-N	-0.06±0.062	-0.01±0.062	-0.1±0.062	0.08±0.062
OSI>0.3	LR-N	-0.01±0.001	-0.01±0.001	-0.03±0.001	0.01±0.001
	N	0.03	0.02	0.04	0.02
	RR-N	-0.02±0.001	0±0.001	-0.01±0.001	0.03±0.001
OSI>0.145	LR-N	0±0.02	-0.03±0.02	-0.05±0.02	-0.02±0.02
	N	0.09	0.09	0.14	0.11
	RR-N	-0.02±0.02	-0.01±0.02	-0.01±0.02	0.05±0.02
OSI>0.238	LR-N	-0.02±0.004	-0.02±0.004	-0.04±0.004	0.01±0.004
	N	0.05	0.04	0.07	0.04
	RR-N	-0.03±0.004	-0.01±0.004	-0.01±0.004	0.05±0.004
nOSI>1.125	LR-N	-0.01±0.01	-0.02±0.01	-0.06±0.01	-0.01±0.01
	N	0.07	0.06	0.11	0.08
	RR-N	-0.02±0.01	0.01±0.01	-0.02±0.01	0.05±0.01
RRT>9.35	LR-N	-0.02±0.055	-0.03±0.055	-0.06±0.055	-0.02±0.055
	N	0.11	0.10	0.15	0.12
	RR-N	-0.03±0.055	0.01±0.055	-0.03±0.055	0.05±0.055
RRT>5.29	LR-N	-0.01±0.047	-0.09±0.047	-0.05±0.047	-0.02±0.047
	N	0.16	0.21	0.21	0.17
	RR-N	-0.03±0.047	-0.02±0.047	-0.06±0.047	0.07±0.047
RRT>7.14	LR-N	0.02±0.051	-0.06±0.051	-0.06±0.051	-0.02±0.051
	N	0.10	0.15	0.18	0.14
	RR-N	0±0.051	0±0.051	-0.05±0.051	0.07±0.051

Reproducibility uncertainty reported after ± symbol

The influence of the morphology changes on the computed flow field is qualitatively depicted in Figs. 50-53, where the contour plots of the nOSI, WSSTG, OSI, and RRT are shown for all twelve investigates cases. The contour lines for nOSI=1.125 and OSI=0.238 mark the boundaries of the wall regions exposed to high and low OSI respectively. As expected, similar distribution patterns are expressed for the nOSI and RRT indices that measure a similar hemodynamic feature. Qualitative RRT in Figs. 51 and 53 present similar distribution patterns as those for nOSI and OSI in Fig. 50and 52 and this was expected as these parameters are measures of similar hemodynamic features. Likewise, the spatial distribution for RRT as presented in Figs. 51 and 53 are not associated with significant changes in the total hemodynamic burden on the wall, as shown in Table 21. The WSSTGs in the vicinity of the CB are not strongly affected by the head rotation, and

the explanation relies on the fact that this feature is primarily sensitive to the frequency content of the flow, which was kept the same for all simulations.

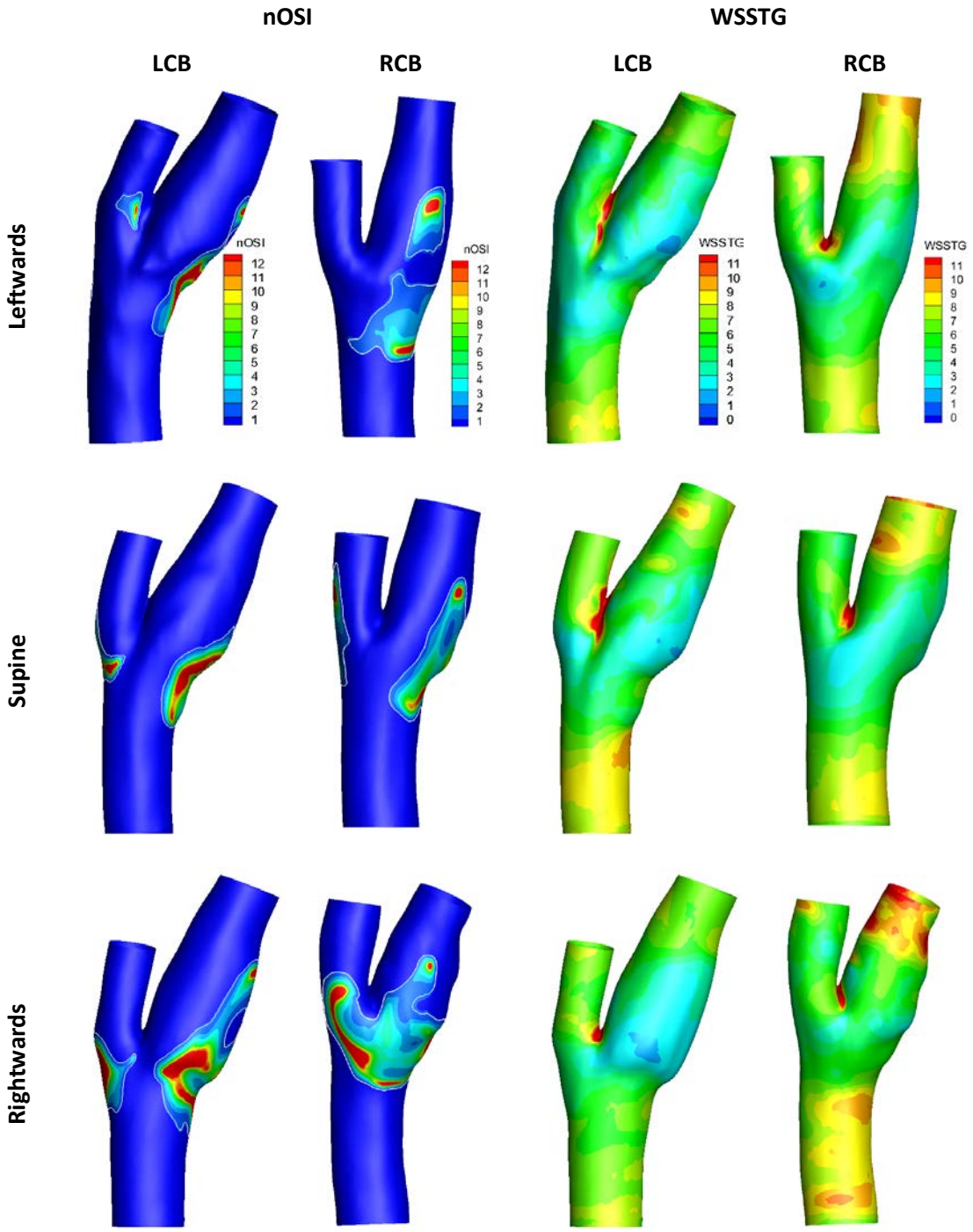

Figure 50: Contour plots of time-averaged nOSI and WSSTG for the Right and Left Carotid in the Neutral, Leftward and Rightward rotated head position for the subject I. nOSI=1.125 contour lines are shown.

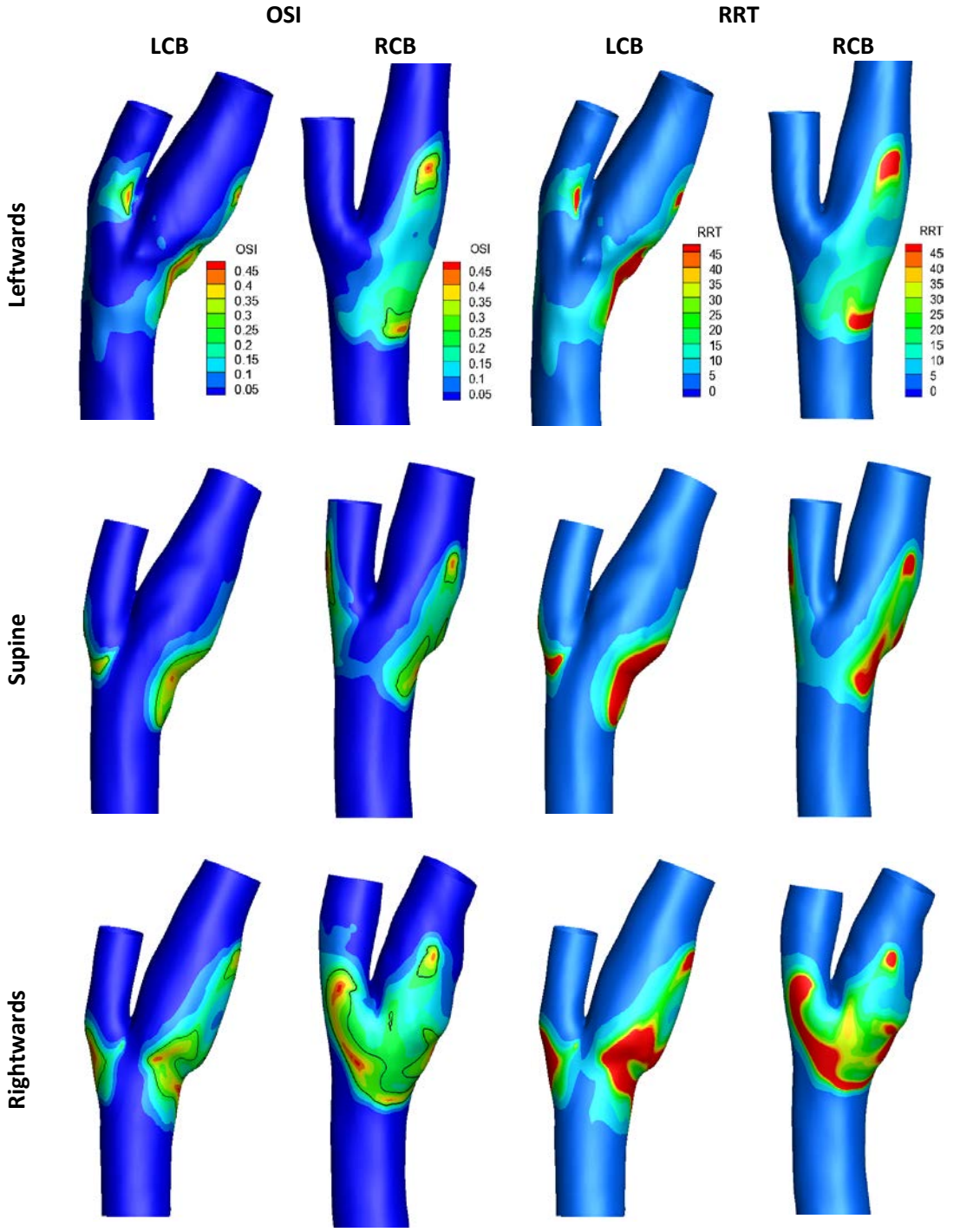

Figure 51: Contour plots of time-averaged OSI and RRT for the Right and Left Carotid in the Neutral, Leftward and Rightward rotated head position for subject I. OSI=0.238 contour lines are shown.

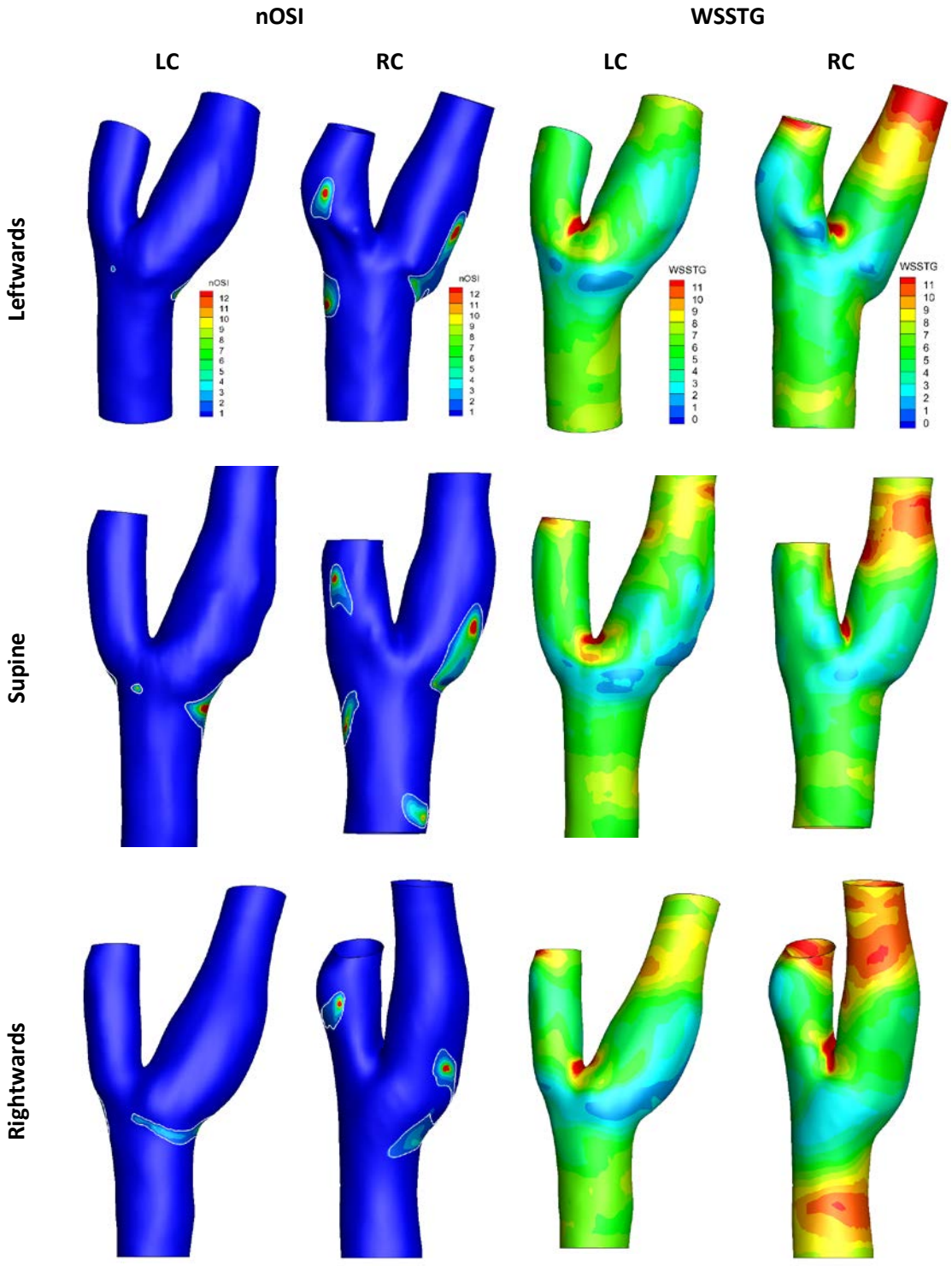

Figure 52: Contour plots of time-averaged nOSI and WSSTG for the Right and Left Carotid in the Neutral, Leftward and Rightward rotated head position for subject II. nOSI=1.125 contour lines are shown.

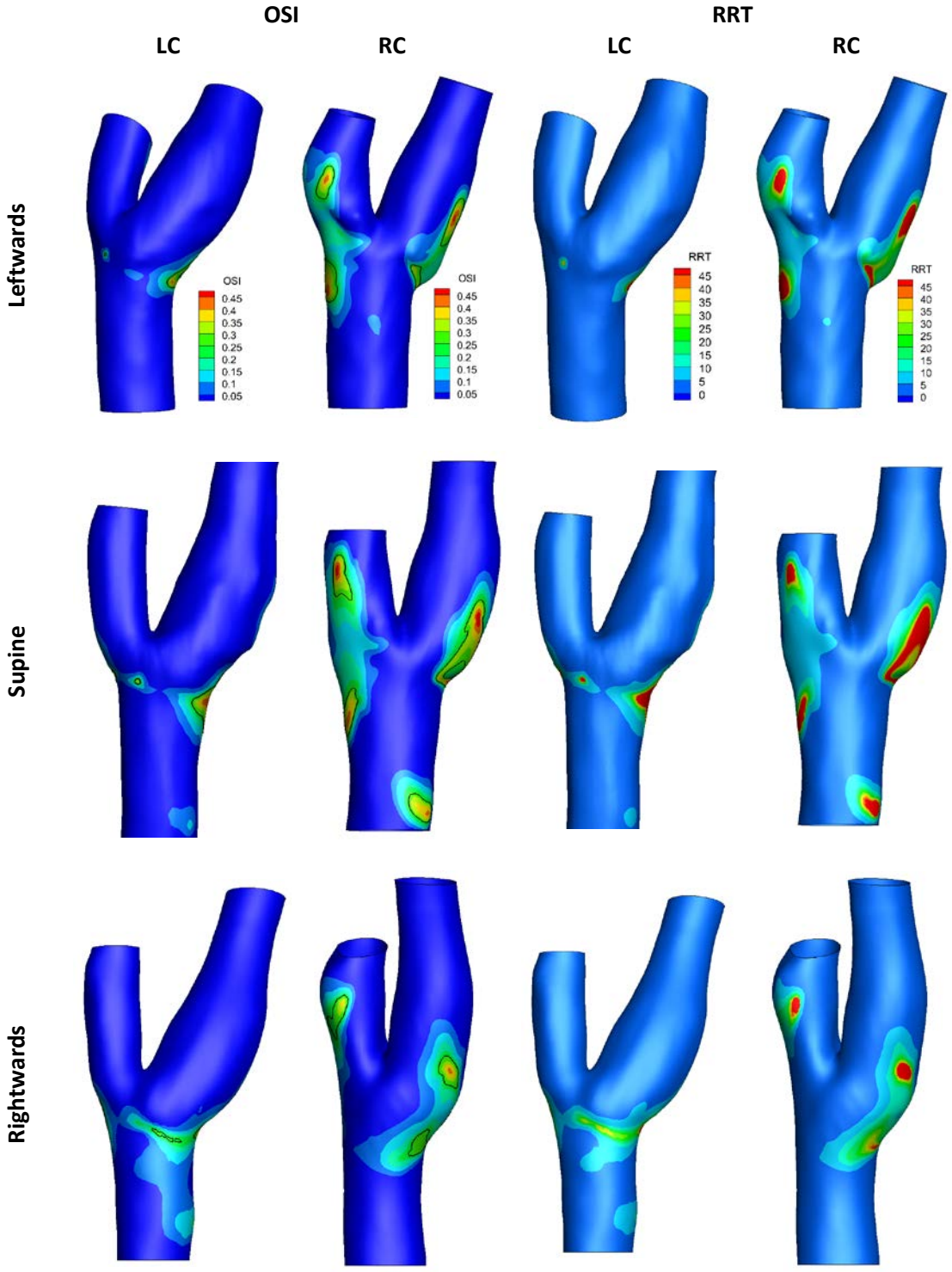

Figure 53: Contour plots of time-averaged OSI and RRT for the Right and Left Carotid in the Neutral, Leftward and Rightward rotated head position for subject II. OSI=0.238 contour lines are shown.

The results present significant changes in CB morphology due to head rotation, and alterations on various hemodynamic parameters. However, a correlation between patterns of geometric changes with changes in the hemodynamic environment was not found. A study of Zhang *et al.* [169] showed a correlation between expansion of the bifurcation, measured from the ICA angle with local CB hemodynamics. Keeping in mind the results observed here, and the results from Zhang *et al.* someone could expect that head rotation causes significant changes in the local CB hemodynamics, but taking into account the complexity and uncertainties of MR imaging, of image processing and numerical simulation, then the results of Table 21 are to be expected.

Furthermore, the influence of the morphology changes in other hemodynamic characteristics is qualitatively depicted in Figs. 54-57. These parameters included plots of: a) the streamlines, and in several location along the CB, b) the skewness of the velocity profile, c) the secondary flows occurred (tangential velocity), and d) the axial velocity.

The results presented in Figs. 54 and 56 indicate that the streamline direction seems to compress toward the flow divider and the inner wall of the ICA, something which Zarins *et al.* also noticed in an experimental study [21]. The Re number was 400 in their study and here the mean Re is 305 at inlet region. Due to the absence of a corresponding experimental flow visualization in this study, it is difficult to know if the computed pathlines and velocities reflect the reality. It should be noted however that several studies combining particle image velocimetry (PIV) and CFD confirmed the experimental and numerical results [208-210].

The velocity skewness represented below is in agreement with the definition of the Dean number (De), according to which high curvature leads to a high De number and strong velocity profile skewness, which may finally separate the flow. Also, the vortices which appear in the carotid bulb are represented in Figs. 55 and 57.

The hemodynamic analyses will be continued in the next section where CFD simulations were performed on the same volunteers, using the realistic inlet waveforms.

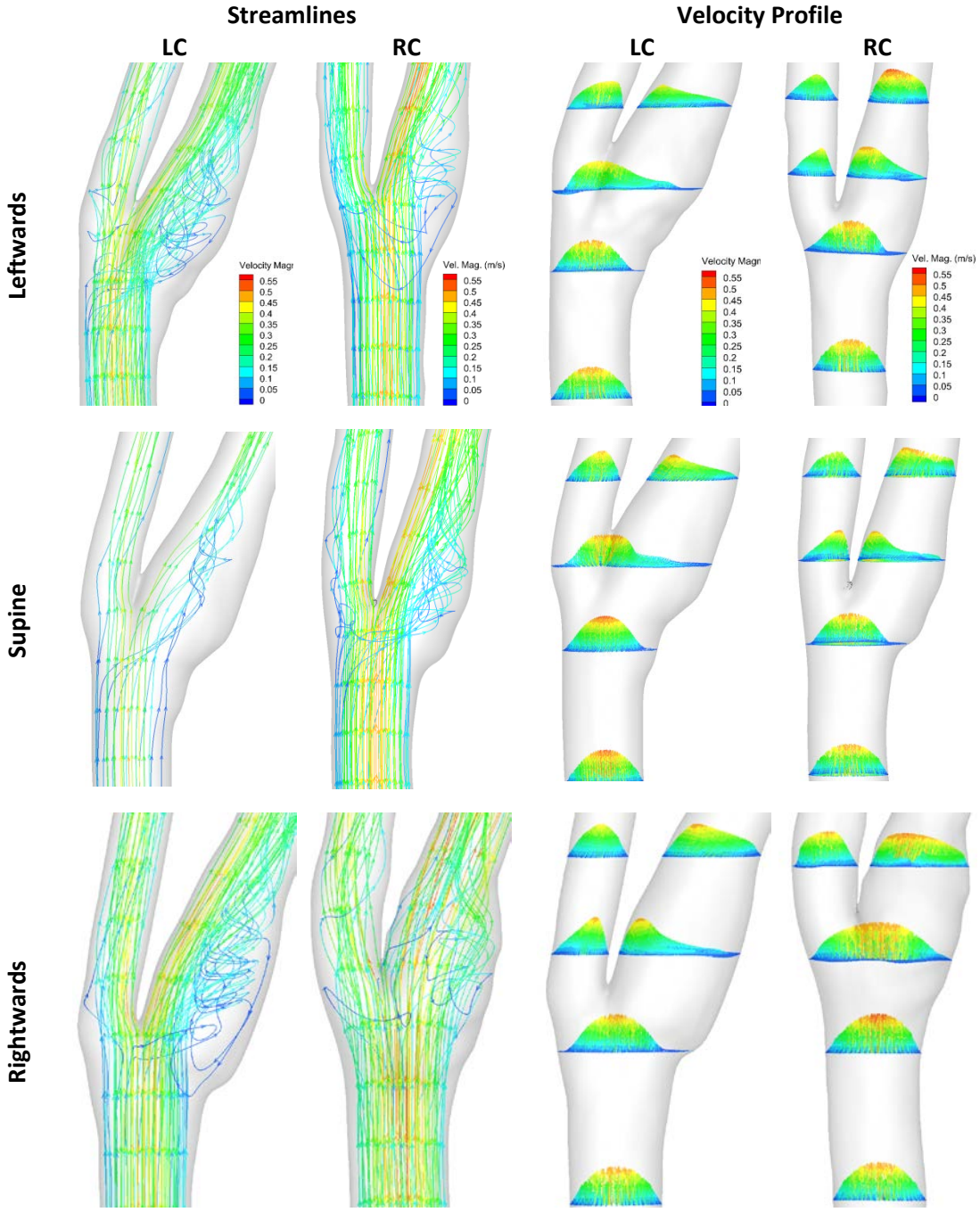

Figure 54: Volunteer I. Time-averaged streamline plots and the velocity profile representing the skewness variation for the three investigated postures and the LCA and RCA.

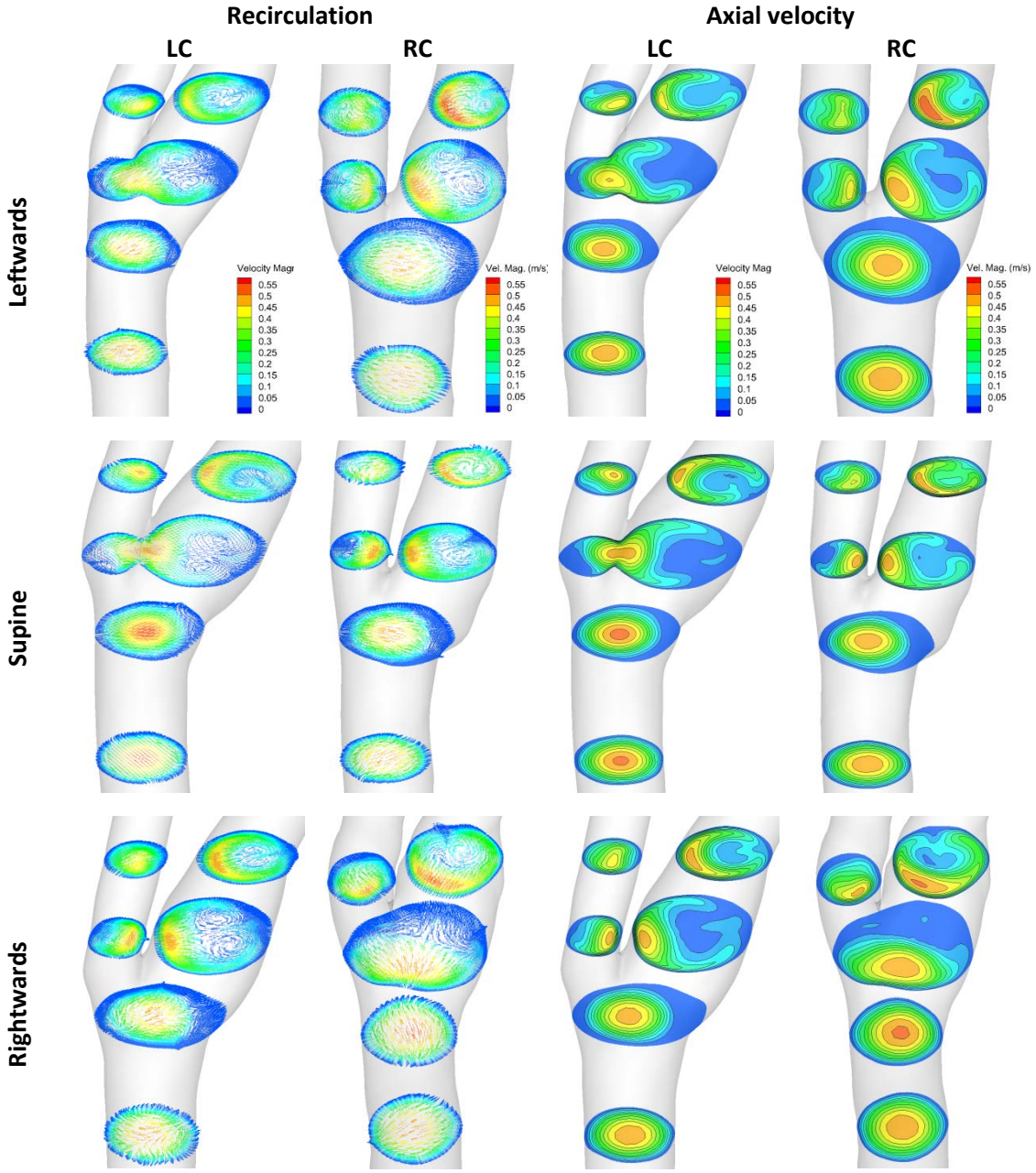

Figure 55: Volunteer I. Time-averaged secondary velocities and contour plots of the averaged velocity magnitude for the two investigated postures and both CB.

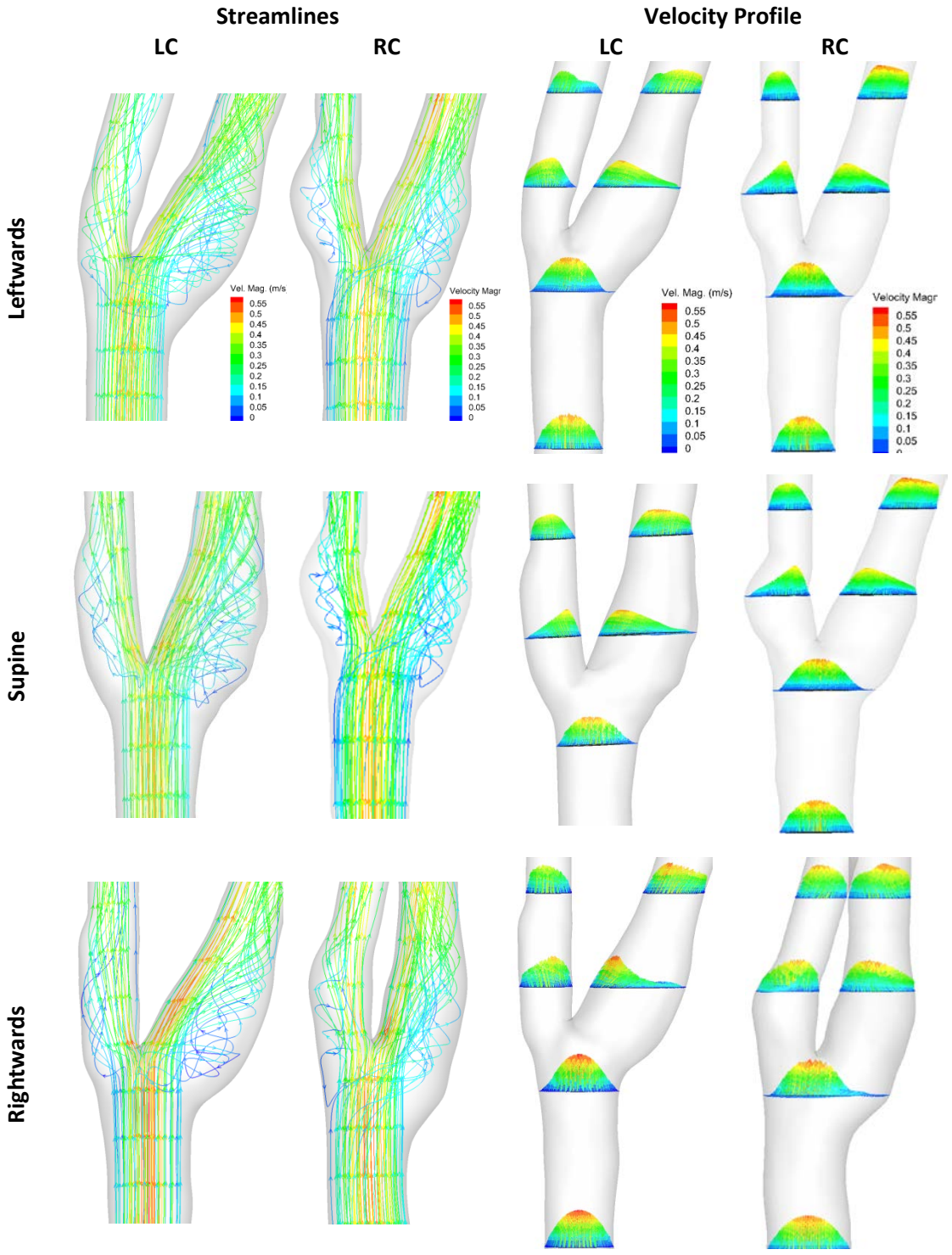

Figure 56: Volunteer II. Time-averaged streamline plots and the velocity profile representing the skewness variation for the three investigated postures and the LCA and RCA.

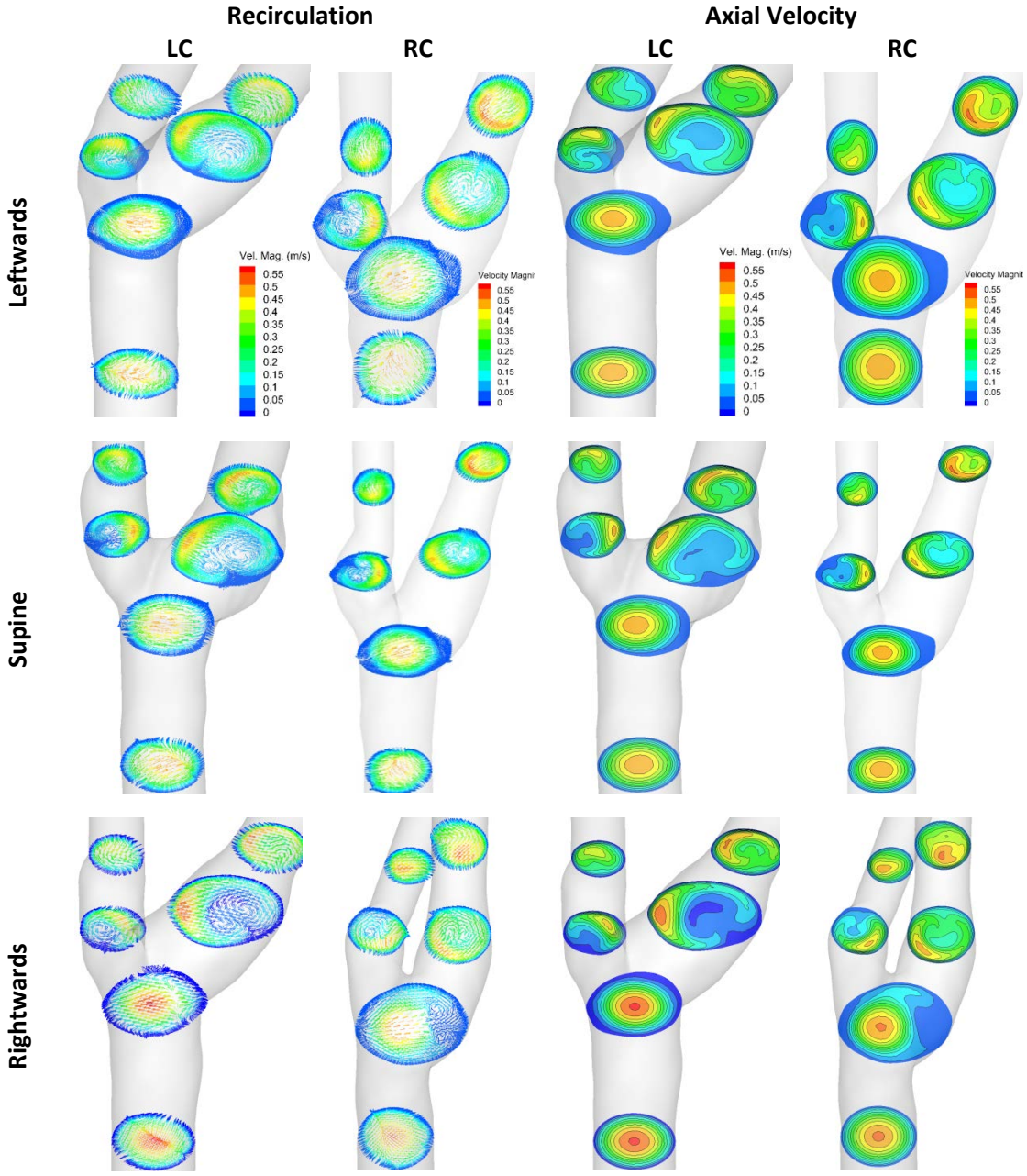

Figure 57: Volunteer II. Time-averaged secondary velocities and contour plots of the averaged velocity magnitude for the two investigated postures and both CB.

Chapter 9:

Impact of Head Rotation on the Patient-Specific Carotid Flow

This chapter of the study aims at evaluating, on a subject-specific basis, the alterations that head rotation poses on the blood flow characteristics of the carotid bifurcation. To approach the atherosclerosis disease from the personalized medicine point of view, novel markers associated with gene factors, environmental factors, and gene-by-environment interactions must be validated [77]. The methodology that was followed, from MR images to CFD simulations, was described earlier, and is also well-established and widely applied and can be found in several studies [20, 56, 57, 59, 60, 63].

In this study, six healthy volunteers were MR-scanned in two head postures: supine neutral and prone with rightward head rotation. Cross-sectional flow velocity distribution was obtained using PC-MRI at the level of approximately $3D_i$ (~20mm) below the CB. The flow data acquired spread in 20 phases over the cardiac cycle. In Appendix IV a small comparison study is carried out, in order to estimate the impact in flow data using 40 instead 20 cardiac phases. The results indicated that peak systolic flow rate is reduced at prone position in most cases for both CCAs. Morphological MR images were used to segment and construct the CB models. Numerical simulations were performed and areas were exposed to high helicity or unfavorable hemodynamics was calculated.

9.1 Blood Flow

The blood flow time history was obtained by PC-MRI and for further process and analyses the Segment v1.9 R2178 and Matlab R2012b software were used. The image data were decomposed in 13 harmonics with FFT as described previously in paragraph 7.5.1. The averaged inlet blood flow waveforms from all volunteers and histograms for each volunteer independently are represented in Fig. 58.

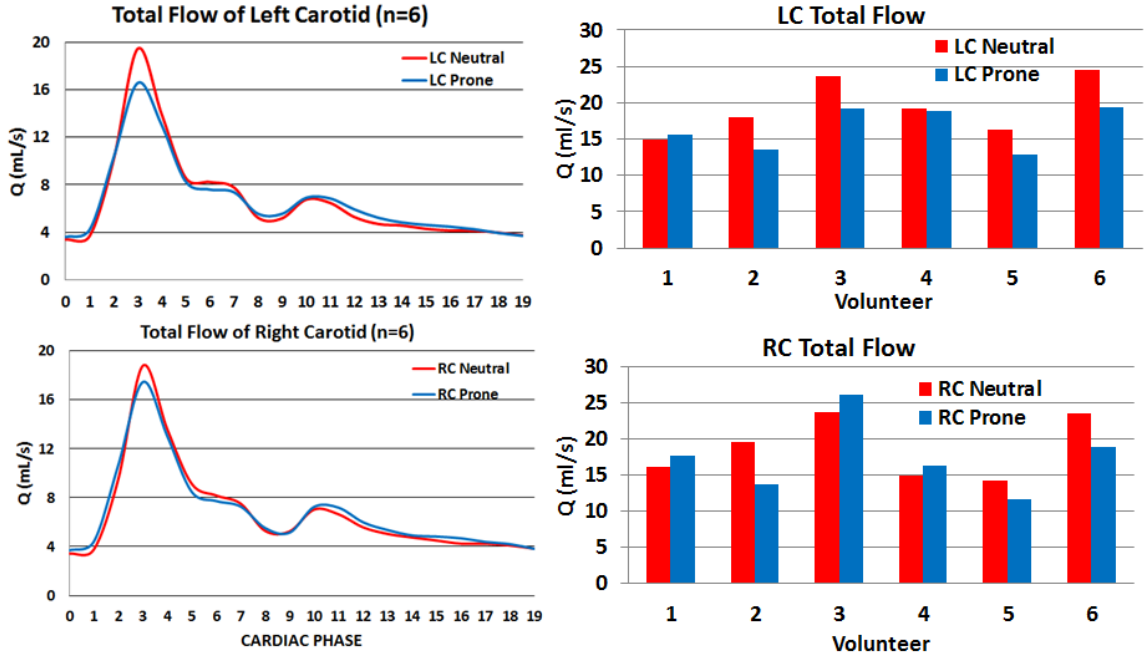

Figure 58: Comparison between the two head postures of total blood flow from all volunteers together (left), and separately (right).

The blood flow index (BFI), a modification of the arterial resistive (resistance) index (RI), was calculated for better assessment of the impact of head rotation on blood flow. The RI is defined as $(S-D)/S$ where S is the height of the systolic peak and D the end-diastolic [211, 212]. The BFI for all volunteers is represented below in Fig. 59. The BFI in this study is defined by:

$$BFI = \frac{Q_{sys}}{Q_{dia}} \tag{9.1}$$

where Q_{sys} is the blood flow at peak systole and Q_{dia} the flow at end diastole.

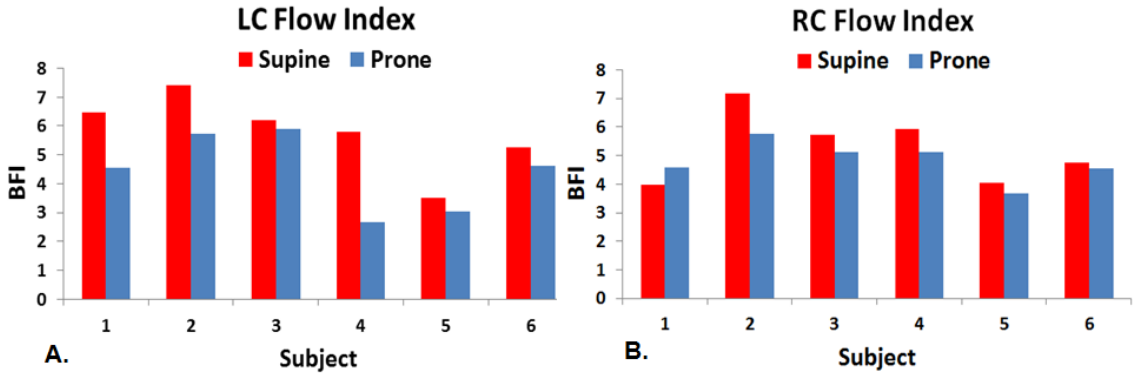

Figure 59: Blood flow Index (BFI) for the left (A) and right (B) CCA, for each volunteer and for both investigated head postures.

The results from Figs. 58 and 59 depicted the significant reduction in blood flow rate at peak systole with rightward head rotation. BFI was reduced in all cases, whilst a similar reduction was seen for the RCB in 5 out of 6 volunteers (Fig. 58). This may be due to changes in the downstream impedance with head rotation that could cause reduction of peak systolic blood flow. It may also be related to slight alterations in the heart rate of volunteers between the two scanning sessions. In addition, rightward head rotation seems to slightly increase total CCA flow at end diastole, which in combination with the reduced peak systolic flow results in the observed BFI changes. Nevertheless, the shape of the flow waveform remains unaffected as indicated in Fig. 61 and also indicates that head posture affects the cross sectional distribution of peak systolic velocities. Rightward rotation seems to extenuate the occurrence of high velocities at the periphery of the lumen and accentuate the velocity distribution skewness. Interestingly enough, CCA flow seems, as well as CCA diameter, to be associated with ischemic stroke independently of carotid atherosclerosis and CVD risk factors [212].

9.2 Computational Simulations

For the CFD simulations the individualized blood flow of two healthy volunteers was used as the inlet boundary condition at the subject-specific geometry models. A total of 16 computational simulations were performed, 8 for each volunteer. In more detail, 4 simulations for realistic inlet waveforms on both CBs and the two head postures, and other 4 simulations using the second postural position inlet waveforms to estimate the impact of inlet waveform. The numerical simulations were performed using Fluent to solve the Navier-Stroke equations as described earlier, with the physiological characteristics represented in Table 22.

Table 22: Physiological characteristics of inlet at CCA. S: Supine position (normal head posture), P: Prone position (rightwards head posture)								
	Volunteer I				Volunteer II			
	LCB		RCB		LCB		RCB	
	S	P	S	P	S	P	S	P
HR (bpm)	69	72	69	72	70	66	70	66
T (ms)	826	789	826	789	820	865	820	865
A_{inlet} (cm^2)	0.38	0.37	0.39	0.4	0.38	0.39	0.34	0.34
$A_{clipped}$ (cm^2)	9.8	9.34	8.76	8.57	9.33	10.1	7.62	7.6
R (mm)	3.48	3.43	3.52	3.57	3.48	3.52	3.29	3.29
$R_{rec.}$ (mm)	3.24	3.46	3.36	3.25	3.31	3.36	3.13	3.30
V_{max} (mm/s)	44.7	38.0	43.4	40.6	36.8	34.2	36.3	35.3
V_{avg} (mm/s)	20.5	18.7	20.5	20.4	18.1	16.2	16.9	15.9
Re_{avg}	398	387	413	398	360	311	317	316
α	4.89	5.35	5.07	5.02	5.02	4.72	4.74	4.87
Δt (μs)	207	197	207	197	205	2016	205	216
ρ (kg/m^3)	1050							
μ (kg/m·s)	0.0035							

HR: heart rate, T: time period (RR interval), A_{inlet}: Surface area at inlet, $A_{clipped}$: Surface area of clipped model, R: realistic radius from MRI at inlet, R_{rec}: inlet radius from reconstructed model, V_{max}: maximum velocity at inlet, V_{avg}: averaged velocity at inlet, Re_{avg}: averaged Reynolds number at inlet, α: Womersley number, Δt: time step for each simulation to achieve 4000 iterations per cycle, ρ: blood density, μ: blood dynamic viscosity

The inlet blood waveforms used for inlet boundary condition for each subject independently are shown in Fig. 60.

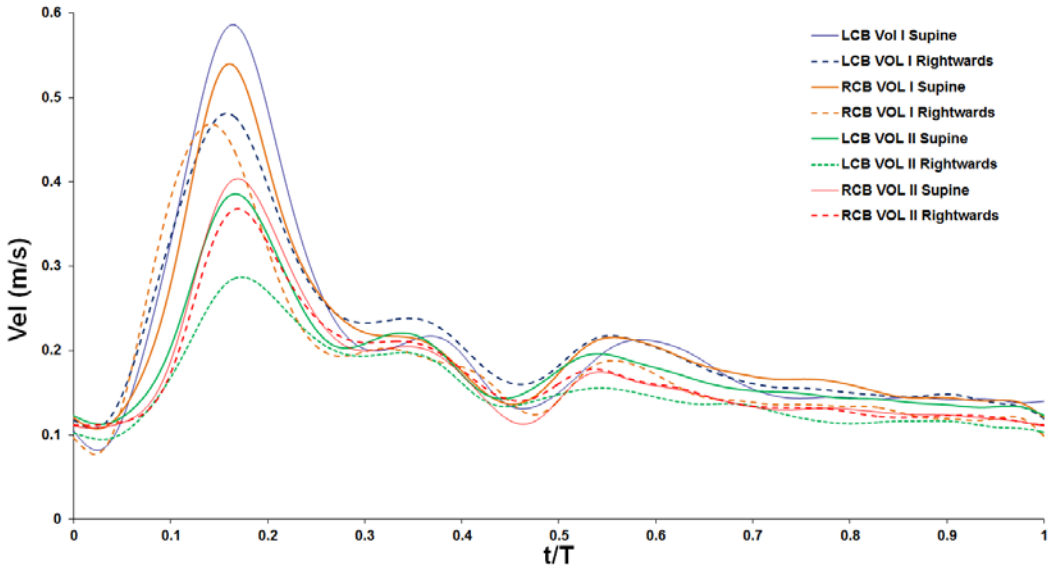

Figure 60: The six subject-specific inlet waveforms used as inlet boundary conditions.

Table 23 shows the peak velocity and the cycle-averaged flow rate and velocity for the two volunteers. It also contains the main results for all six volunteers and the mean values and the corresponding values from other researchers.

Table 23: Blood flow parameters for the six volunteers and measurements from previous studies.											
	Posture	Vol. I		Vol. II		Mean	n=6		Mean	Studies	
	Carotid	RC	LC	RC	LC		RC	LC			
$Q_{cyc,}$ (mL/s)	**neutral**	8.3	7.9	5.9	7.0	7.3	6.7	6.7	6.7	6.0[202]	6.5[213]
	prone	8.1	7.2	5.5	6.4	6.8	6.8	6.7	6.8	-	-
V_{cyc} (cm/s)	**neutral**	43.4	44.7	35.3	36.8	40.1	37.1	37.3	37.2	38.8[202]	40.9[214]
	prone	40.6	38.0	35.3	34.1	37	37.7	33.9	35.8	-	-
V_{peak} (cm/s)	**neutral**	103.4	97.5	66.4	65	83	81.8	83.6	83	108.2[202]	77.5[213]
	prone	84.6	83.7	55.1	65.9	72.3	84.5	72.8	78.7	-	-

[202] Holdsworht et al. (n=17), [213] Vannimen et al. (n=10), [214] Schoning et al. (n=48)

Figure 61 represents the velocity waveforms and the cross-sectional of peak systolic velocities for volunteer I (A) and volunteer II (B).

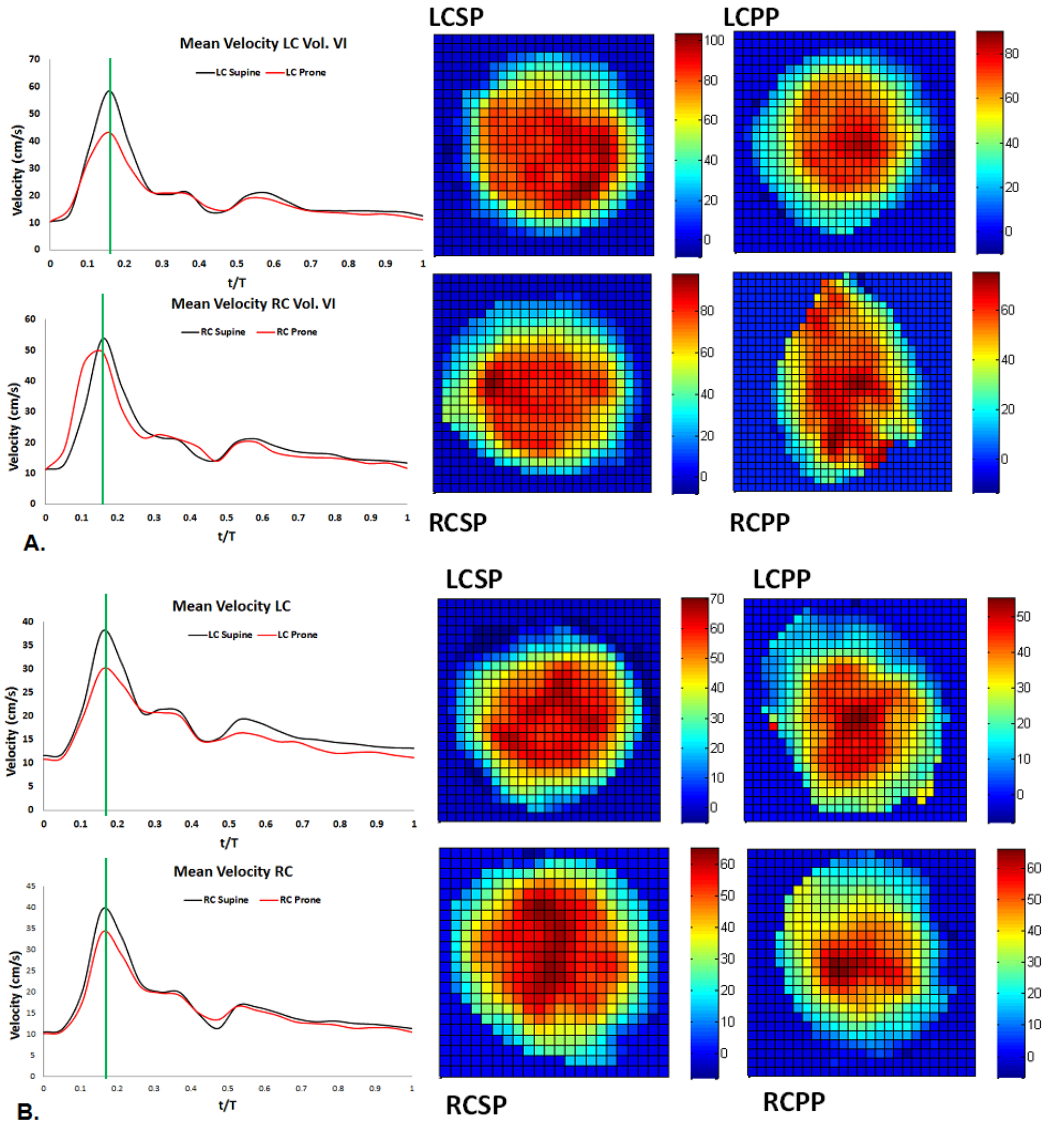

Figure 61: Inlet velocity waveforms (left) and lumen velocity distribution at peak systole (right) for volunteer I (A) and volunteer II (B).

Figure 62 illustrates the isosurfaces of LNH averaged over the cardiac cycle which indicate a significant region of high intensity. Bidirectional helical structures are represented by blue (clockwise) and red (counterclockwise) regions. The threshold of 0.8 has been chosen to highlight high amount of helicity [144].

These flow structures originated at the bifurcation region and developed within the ICA and ECA. These patterns were conserved for both head postures in the left CB, but have shown variation in the LNH direction and spatial extent in the right CB. The comparison of the instantaneous LNH at peak systole and end diastole shows differences in direction and spatial extent for almost all cases demonstrating that geometric changes combined with dynamic changes in the pressure distribution cause instantaneous changes in the helical structure distribution. Overall, LNH revealed a strong subject and vessel dependency. Head rotation does not seem to favor clockwise or counterclockwise blood rotation, although it significantly affects the instantaneous spatial extent of the LNH.

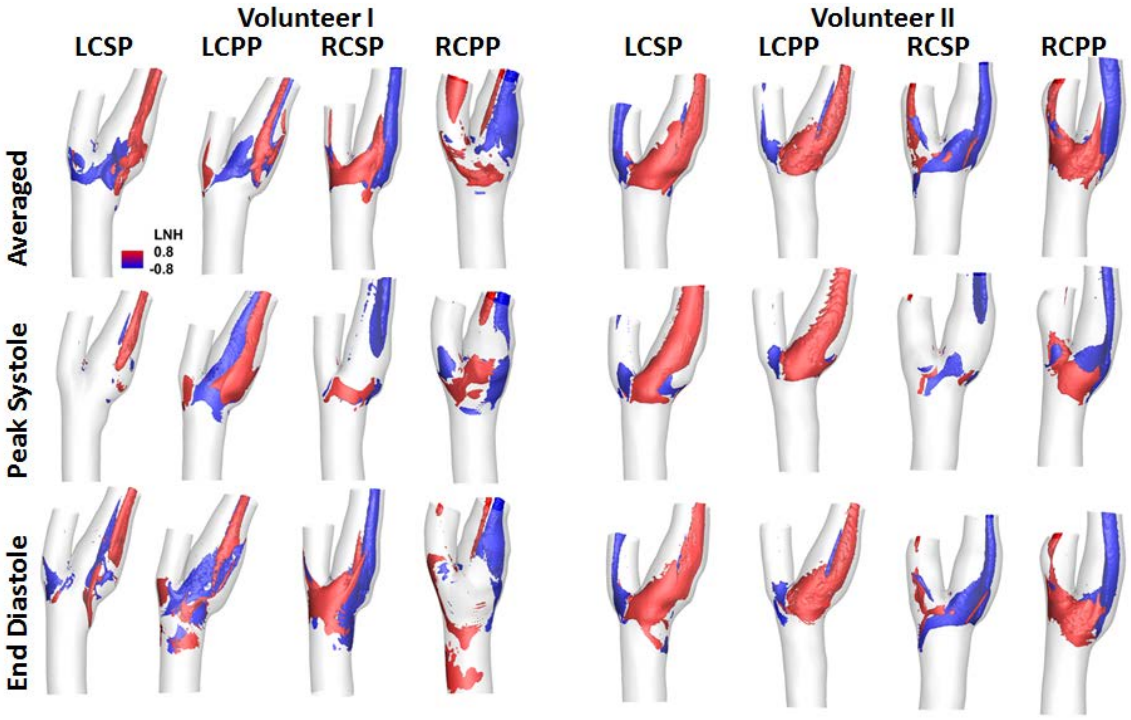

Figure 62: Localized normalized helicity (LNH) isosurfaces for the two investigated head postures: averaged throughout the cardiac cycle (top), instantaneous at peak systole (middle) and instantaneous at end diastole. LNH=0.8 indicates clockwise blood rotation and LNH=-0.8 counterclockwise rotation.

As outlined by Gallo *et al.* [144], helicity of high intensity may suppress flow disturbances and, thus, prevent plaque deposition [142]. Likewise, helicity and vorticity, are primarily responsible for particle transport and mixing of low diffusivity fluids like blood [215].

The comparison of nOSI, RRT and WSSTG distribution is performed in Figs. 63, 64 and 65, respectively. The evaluation dependency on geometry and inlet flow waveform shows that when the geometry is kept constant and the inlet waveform changes (horizontal comparison), the pattern of the atherosclerosis susceptible wall regions is very similar. However, the quantitative results of nOSI have differences.

These results are in good agreement with those of Campell *et al.* [216], who investigated the effect of inlet waveform on CFD simulations using various inlet profiles such as blunt, parabolic, Womersley or the real subject profile, and Moyle *et al.* [193] that found that geometric parameters influence the hemodynamic features more significantly than the inlet waveform. Figures 63-65 (diagonal comparison) show the results for the inlet waveform when this is kept constant, as well as the wall regions susceptible to atherosclerosis which alter notable both qualitatively and quantitatively.

However, when the realistic conditions are taken into account (vertical comparison between the first pair in each category), it appears that the rotation-derived changes in the “sensitive” carotid wall regions are extenuated. This may indicate that the interrelation between geometry and flow waveform tends to autoregulate disturbed flow fields and moderate unfavorable conditions. These suggestions are quantitatively supported by data presented in Table 24.

As highlighted by the difference in corresponding calculated wall regions between the two head postures, the adoption of a common inlet flow waveform can significantly differentiate the carotid wall region potentially prone to plaque development. It is proposed, therefore, to use a posture-specific inlet waveform in CFD simulations related to postural effects.

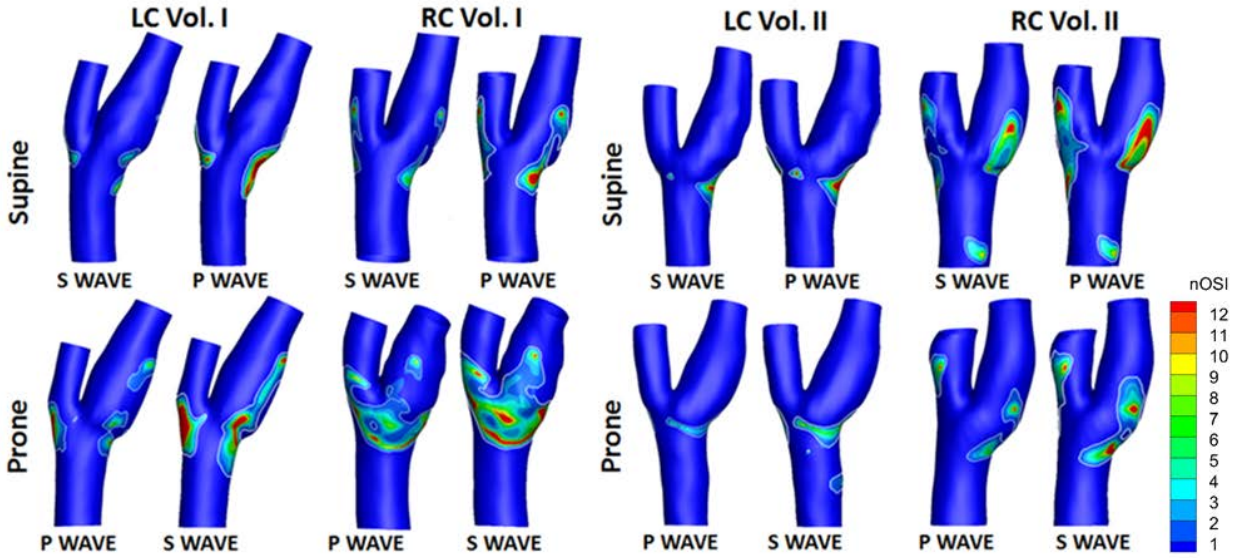

Figure 63: Contour plots of nOSI for the left (LCA) and right carotid artery (RCA) for volunteers I and II. The first row represents the supine normal head position and the second row the prone position with rightwards head rotation. S WAVE corresponds to CFD results obtained using the inlet waveform obtained from the supine position, while P WAVE corresponds to CFD results using the prone position waveform. nOSI=1.125 is shown as a white contour line.

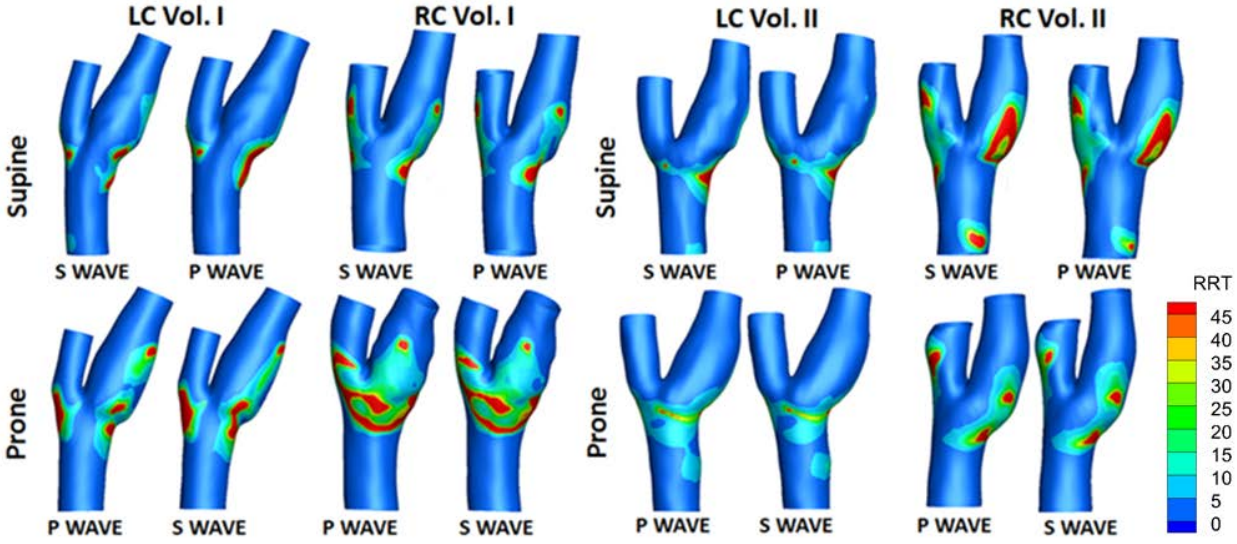

Figure 64: Contour plots of RRT for the left (LCA) and right carotid artery (RCA) for volunteers I and II. The first row represents the supine normal head position and the second row the prone position with rightwards head rotation. S WAVE corresponds to CFD results obtained using the inlet waveform obtained from the supine position, while P WAVE corresponds to CFD results using the prone position waveform.

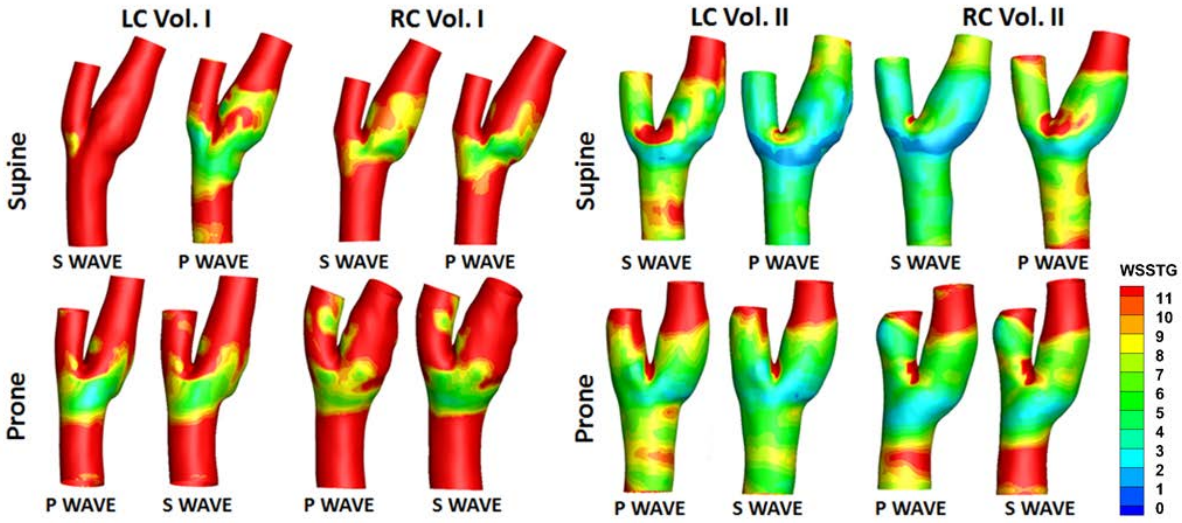

Figure 65: Contour plots of WSSTG for the left (LCA) and right carotid artery (RCA) for volunteers I and II. The first row represents the supine normal head position and the second row the prone position with rightwards head rotation. S WAVE corresponds to CFD results obtained using the inlet waveform obtained from the supine position, while P WAVE corresponds to CFD results using the prone position waveform.

The same hemodynamic parameters can be mapped using VMTK and presented as patched and patched flattened surfaces [155]. This helps to make possible the robust and quantitative comparison among similar models in the parametric space [174]. To achieve this, first the CB surface must be clipped at the three main branches. Each branch is topologically equivalent to a cylinder and mapped onto a rectangular parametric space in which the one coordinate is periodic. Figure 66 shows the decomposed and batched/flattened surfaces with the longitudinal distance at every 1.26 mm and the angular at every $2\pi/15$.

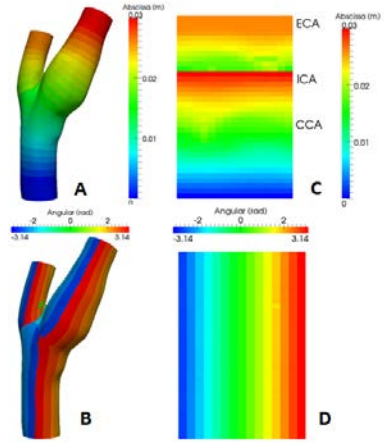

Figure 66: Longitudinal (A) and angular (B) decomposition of CB surface and the corresponded flattened images, patch size (1.26 mm, $2\pi/15$).

The batched surfaces define a finite number of rectangular regions in which the hemodynamic quantities of interest are averaged. The flattened images contribute to compare quantitatively the parameters from 3D into the 2D plane.

Figures 67 and 68 depict the time-averaged OSI, nOSI and RRT as patched and patched flattened images for the comparison between the investigated head postures.

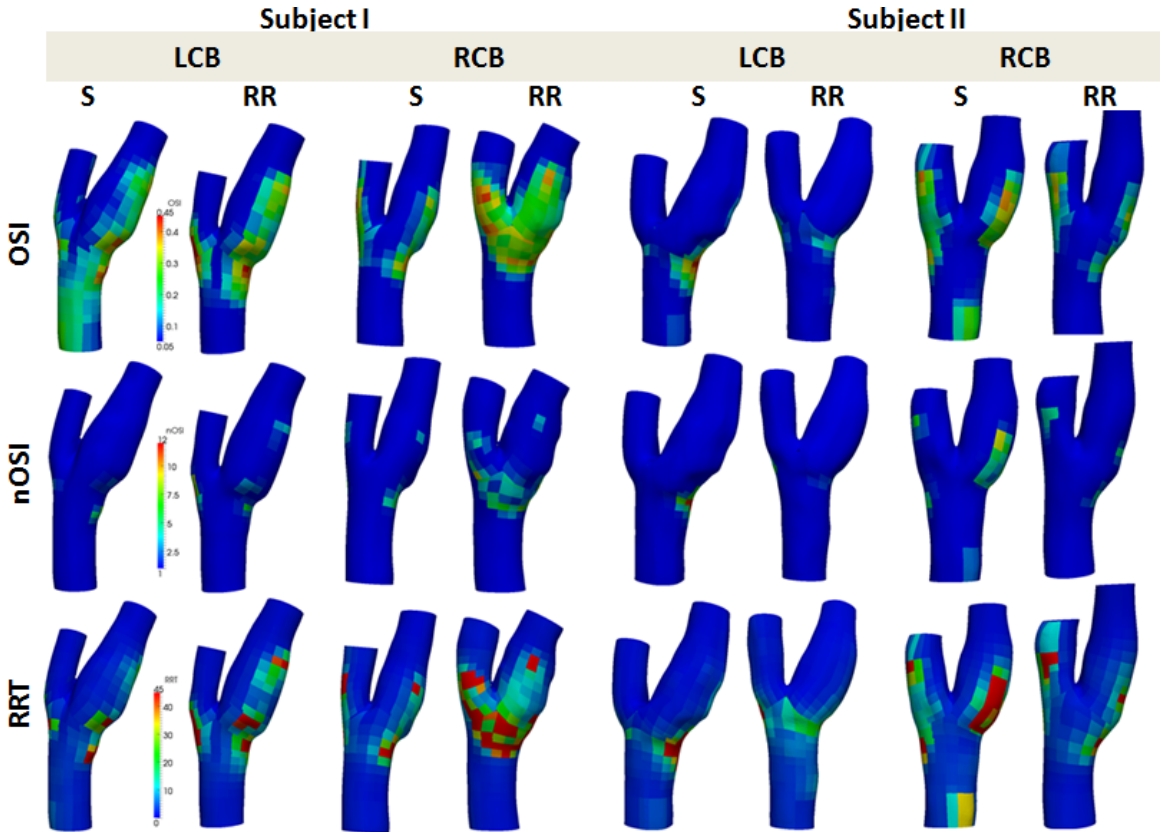

Figure 67: Patched images of time-averaged OSI, nOSI and RRT.

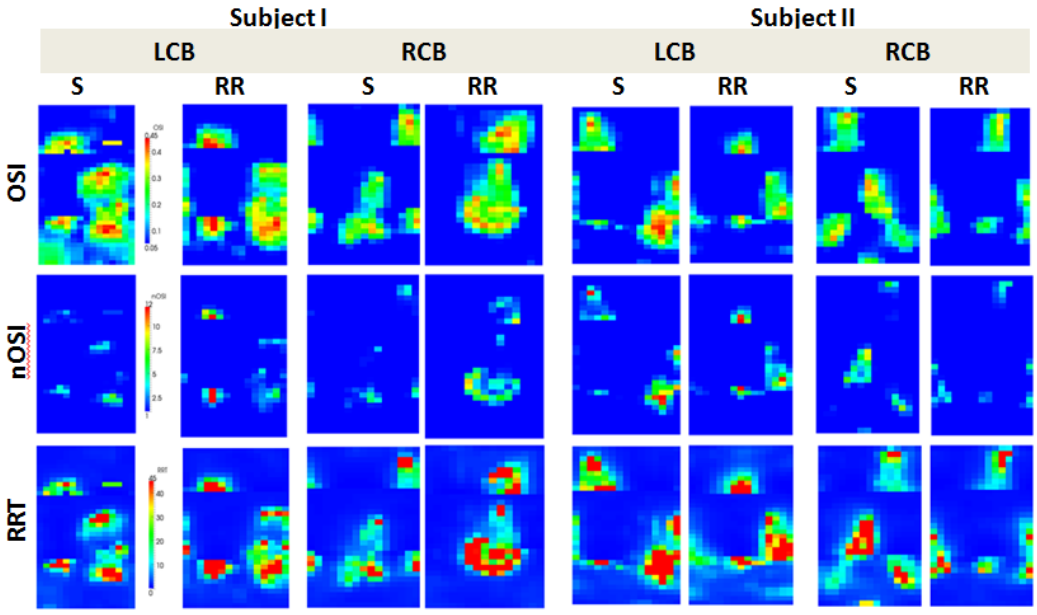

Figure 68: Patched Flattened images of time-averaged OSI, nOSI and RRT.

Figure 69 represents the variations of TAWSS and WSSTG due to head rotation. It also shown the WSS and WSSTG at peak systole and finally the WSS at the end diastole.

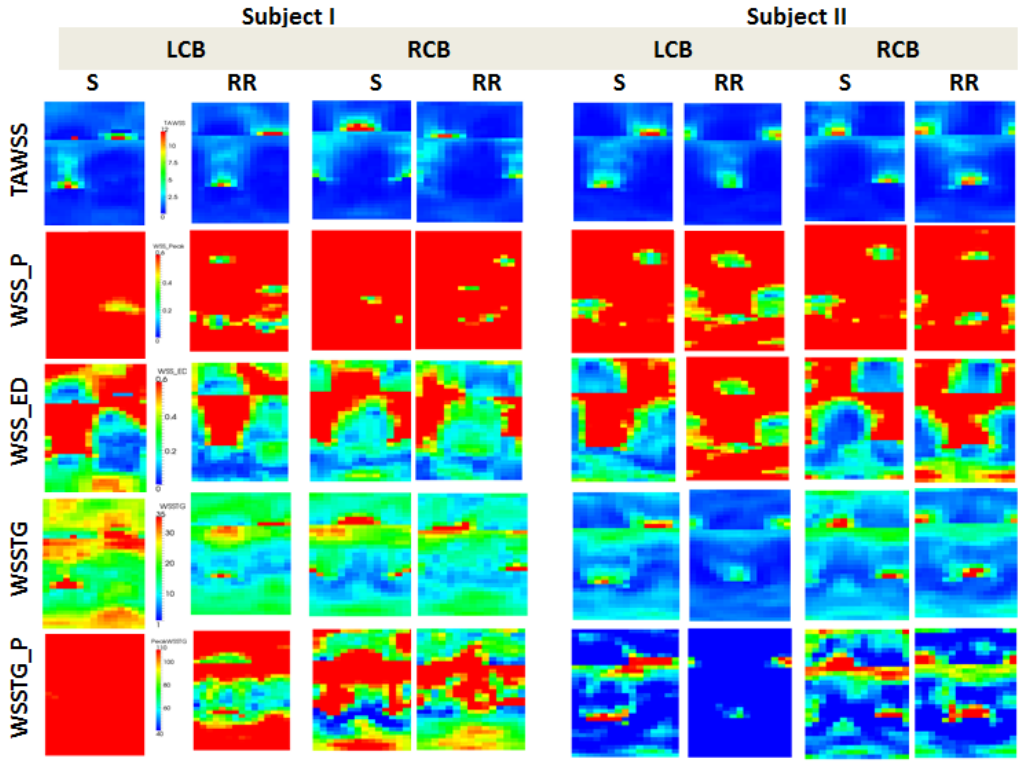

Figure 69: Patched flattened images of (from top row to bottom) TAWSS, WSS at peak systole, WSS at end diastole, WSSTG and WSSRG at peak systole.

Table 24: Area exposed to unfavorable hemodynamics normalised by the total surface area bounded by CCA3, ECA5, ICA5									
		Volunteer I				Volunteer II			
		LCB		RCB		LCB		RCB	
		Phys.	Alt.	Phys.	Alt.	Phys.	Alt.	Phys.	Alt
TAWSS < 32 (Pa)	N	0.28	0.37	0.37	0.32	0.16	0.23	0.22	0.21
	RR-N	0.11	-0.06	-0.14	-0.09	0.08	0.05	0	-0.02
TAWSS < 0.4 (Pa)	N	0.36	0.45	0.46	0.4	0.21	0.26	0.26	0.27
	RR-N	0.16	-0.06	-0.19	-0.12	0.09	0.08	-0.06	-0.05
TAWSS < 0.48 (Pa)	N	0.43	0.54	0.52	0.48	0.27	0.3	0.31	0.33
	RR-N	0.14	-0.06	-0.21	-0.15	0.08	0.09	-0.05	-0.09
OSI > 0.3	N	0.04	0.04	0.05	0.02	0.09	0.06	0.04	0.05
	RR-N	-0.03	-0.01	-0.03	0	0.01	0.02	0.02	0.01
OSI > 0.238	N	0.12	0.11	0.19	0.13	0.33	0.15	0.15	0.16
	RR-N	-0.03	0.02	-0.09	0	-0.08	0.07	0.05	0.03
OSI > 0.238	N	0.07	0.06	0.1	0.05	0.16	0.09	0.08	0.09
	RR-N	-0.03	0	-0.06	0	-0.01	0.03	0.04	0.02
nOSI > 1.125	N	0.1	0.15	0.12	0.02	0.06	0.15	0.19	0.13
	RR-N	0	0	-0.05	0.11	0.04	0.03	-0.09	0.03
RRT > 9.35	N	0.14	0.16	0.18	0.14	0.11	0.13	0.11	0.1
	RR-N	0.01	-0.03	-0.07	-0.03	0.04	0.02	0.02	0.03
RRT > 5.29	N	0.21	0.24	0.28	0.23	0.18	0.19	0.17	0.17
	RR-N	0.04	-0.03	-0.11	-0.06	0.04	0.03	0.01	0.01
RRT > 7.14	N	0.17	0.2	0.22	0.18	0.14	0.16	0.14	0.13
	RR-N	0.02	-0.03	-0.09	-0.05	0.04	0.02	0.02	0.02

The influence of the morphology changes in other hemodynamic characteristics such as streamlines, skewness of the velocity profile, secondary flows and axial velocity is qualitatively illustrated in Figs. 70-73. The qualitative results indicated that the pathlines density compressed toward the flow divider and inner wall of the ICA, as reported earlier.

The velocity skewness also represented, is in good agreement with the results presented earlier related with the Dean number. Finally, as expected, the vortices in the carotid bulb are shown in the cross-sections along the CB.

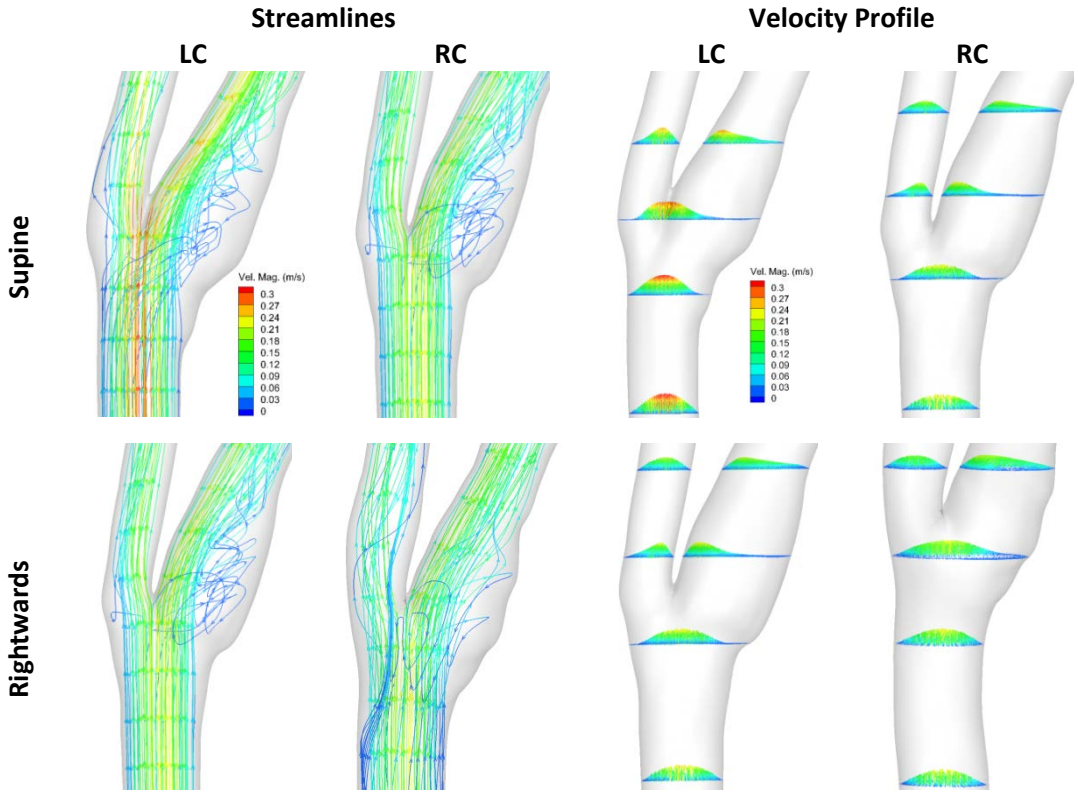

Figure 70: Volunteer I. Time-averaged streamline plots and the velocity profile representing the skewness variation for the two investigated postures and the LCA and RCA.

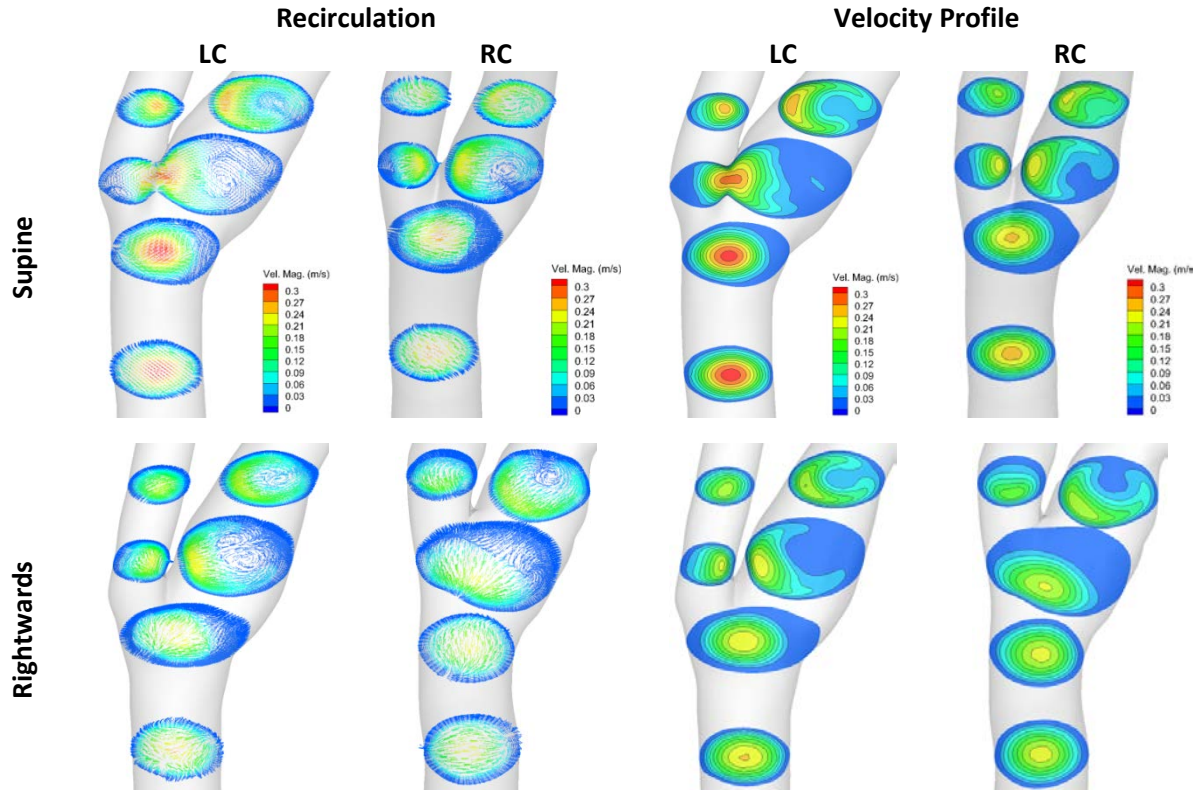

Figure 71: Volunteer I. Time-averaged secondary velocities and contour plots of the averaged velocity magnitude for the two investigated postures and both CB.

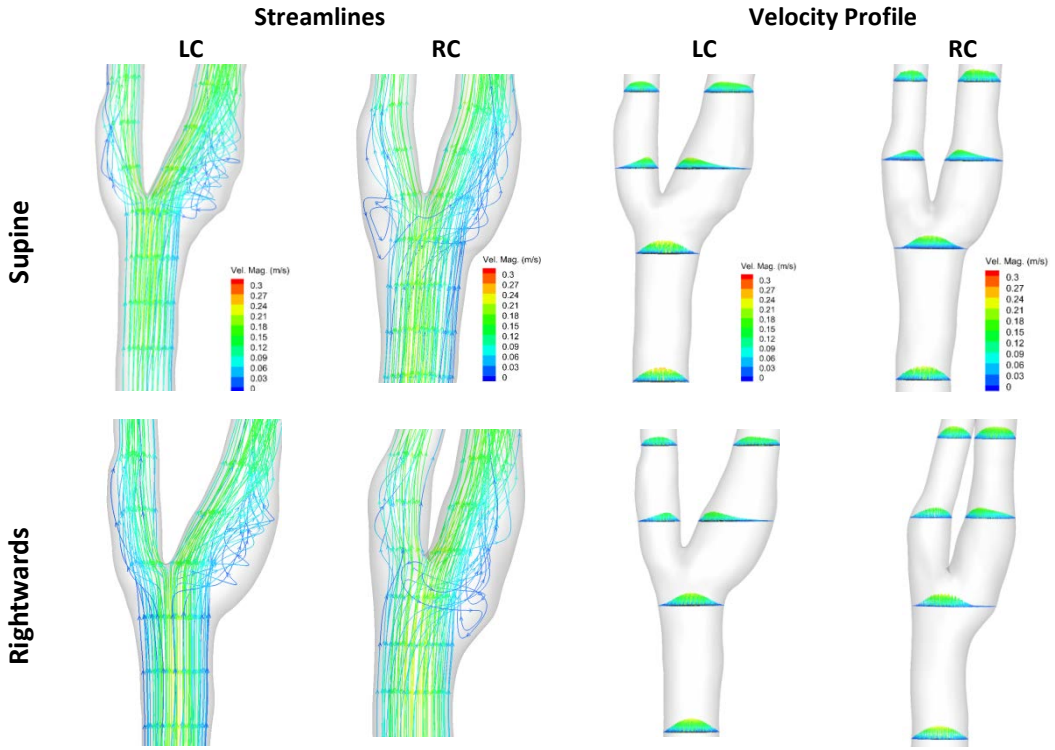

Figure 72: Volunteer II. Time-averaged streamline plots and the velocity profile representing the skewness variation for the two investigated postures and the LCA and RCA.

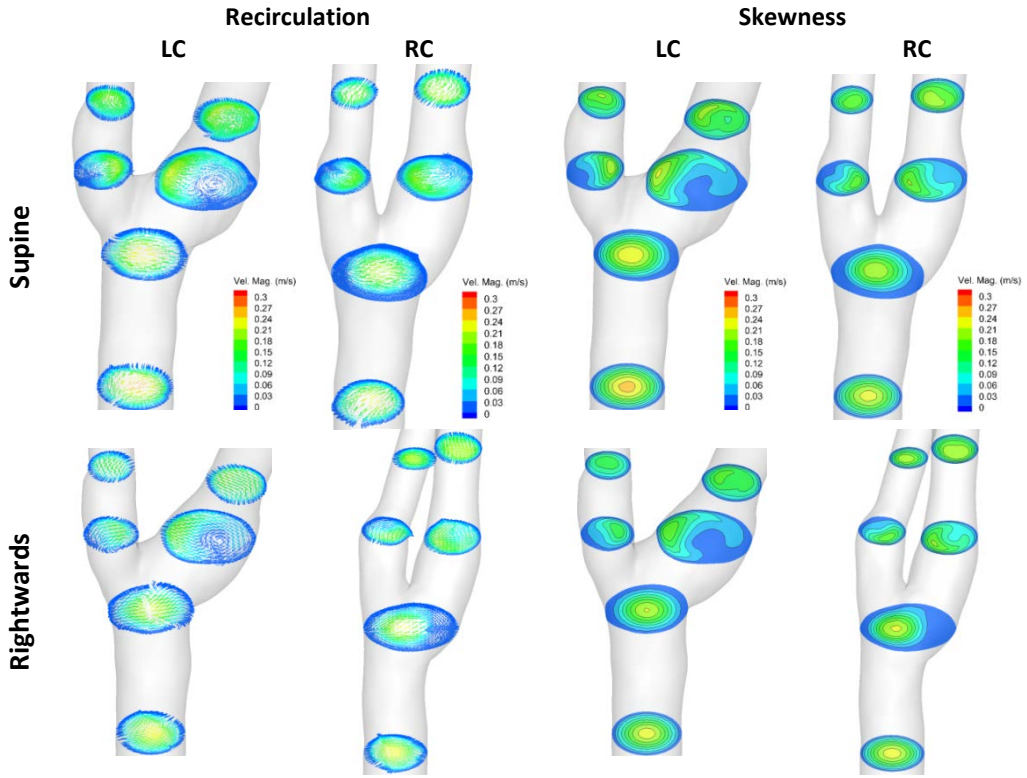

Figure 73: Volunteer II. Time-averaged secondary velocitie s and contour plots of the averaged velocity magnitude for the two investigated postures and both CB.

Part IV: Summary

Chapter 10:

Implications, Conclusions, Limitations and Future Work

10.1 Implications

The significance of this study lies on the geometric changes on human carotid bifurcations as a result of the head rotation. These alterations have consequences on the hemodynamic flow field within the bifurcations. Many individuals during either the daytime or sleep, spend a long time with head posture in the prone rotated position. This may alter the flow field within the carotid artery and influence the process of atherosclerosis. The clinical implications obtained from this study are reported below in more detail.

First, in Chapter 6, the results indicated that for all volunteers there are significant changes in the geometric parameters of both carotid bifurcations when the head is rotated. These changes are random and there is no predisposition to a specific direction of change for any of the parameters extracted. Next, in Chapter 8, the results show that torsion of the neck associated with head rotation, may cause significant hemodynamic alterations in the distribution patterns of RRT, OSI and nOSI on the CB wall. Finally, in Chapter 9 notable decrease in the blood flow at peak systole with rightward rotation is represented and also alterations on the significant hemodynamic features related with atherosclerotic disease.

The effect of head rotation observed in healthy volunteers, may also influence atherosclerotic stenotic patients. As the prone position is a frequent sleeping posture, the morphology and hemodynamic alterations may have significant consequences in the tensile stress distribution around unstable atherosclerotic plaques. The importance of large cyclic stress/strain variations and the interaction between flow and arterial wall is crucial for the understanding of the role of flow-induced mechanism that may lead to artery fatigue and possible plaque rupture [114, 217-221]. This becomes even more important in cases of thin plaque cap and locations with plaque cap weakness that are more closely related to plaque rupture risk [222, 223]. Furthermore, the presence of stenosis alters the already disturbed hemodynamic field in the artery which may increase the risk for thromboembolic complications [224]. Tang *et al.* [225] reported

that large lipid pools and thin plaque caps are associated with both extreme maximum (stretch) and minimum stress/strain levels.

In addition, in the stenotic vessel the WSS developed high values because of flow acceleration as the result of lumen area reduction, and in combination with the turbulent flow may lead to endothelium layer damage [226, 227]. Likewise, high levels of WSS for a long time lead to cellular remodeling (vasculogenesis, angiogenesis and arteriogenesis) that includes cell proliferation, apoptosis and matrix degradations and synthesis [32, 228].

Another clinical implication comes from the area of stents implantation or the performance of endarterectomy. Stent implantation in carotid arteries is not common, but it is performed in about 20-30% of patients when endarterectomy is not possible such as in patients with highly calcified lesions or in carotids with complicated geometries [229]. Previous studies such as those by Valibhoy *et al.* [230] and Diehm *et al*. [231] have reported that carotid stents fracture in some occasions. In this region, it may be beneficial to use the prior knowledge of the hemodynamics and stress distributions for all possible postures, in order to optimize device, placement and minimize the possibility of restenosis [232]. Nitinol stent fractures at the carotid bifurcation have been previously reported, however the role of the head motion in the mechanics of fracture is unknown to a great degree [229, 230].

All these questions could be answered by extended healthy subject and patient studies at different head postures and under various physiologic and pathologic conditions.

10.2 Conclusions

This thesis aimed to present that the head rotation influence the geometry and hemodynamics of the human carotid bifurcation. The methodology followed here, from MR images, the construction of 3D surface models, the definition and quantification of important geometric features and the computational calculations is well established.

The first part of this thesis dealt with medical and engineering research in the area of human carotid bifurcation and the various parameters that correlate with the development of atherosclerosis at this region. The specific aims of this study have been represented and a general literature review has been provided.

Chapter 2 dealt with the human cardiovascular system and more specifically with the carotid bifurcation physiology and functionality. The next chapter reviews the very basics of the hemodynamics.

A brief review of Magnetic Resonance Imaging was done in Chapter 4. An introduction and a description were performed for this modern non-invasive imaging technique, which was used to acquire the information from MR images to construct the surface models.

Chapter 5 dealt with MR imaging processing and the 3D surface construction. At this point the methodology and the optimization of various techniques took place and was followed for the rest of the study. This was done trying different software for image processing to discover the most suitable for our purposes and also to evaluate the accuracy of results by a reproducibility study.

In Chapter 6 a broad description of geometric parameters that were measured on carotid bifurcations was done. Also, the results from all the volunteers were represented for all the investigated head postures. These results for all geometric parameters, various angles, tortuosity, curvature and area ratios was found to be in accordance with similar findings from a much larger sample of volunteers [6, 157, 165, 178]. Our results show that for all volunteers there are significant changes in the geometric parameters of the carotid bifurcation when the head is rotated. This was observed for both the left and right carotid bifurcations. These changes are random and there is no predisposition to a specific direction of change for any of the parameters extracted. The variable pattern change demonstrated might be due to the considerable variability observed in the baseline geometry among subjects. Nevertheless, head

rotation towards a specific direction could have different effect on the same geometric feature for the two CBs of the same volunteer.

In the third part, and more specifically in Chapter 7, the description of the methodology to construct accurate meshes from the existing 3D models and to perform numerical simulations was described. The results of an extensive meshing independence study were presented and the boundary conditions used throughout this study were explained.

In Chapters 8 and 9 the results of the CFD simulations and the effect of head posture on CB hemodynamics head were represented. In Chapter 8, the investigation includes three head postures and the use of the same inlet waveform. The next chapter involves a patient-specific study, where for each case the realistic inlet waveform was applied as the inlet boundary condition.

To conclude, head rotation inflicts changes on the geometric and hemodynamic characteristics of the carotid bifurcation. These alterations affect and influence the exposure of the arterial wall to hemodynamic features related with atherosclerotic disease. The prominent intersubject variability of these changes warrant an individualized approach for the evaluation of the potential risks that head posture may pose on atherosclerotic plaque deposition and/or rupture of existent vulnerable lesions as well as on potential fractures of stents with carotid bifurcations.

10.3 Limitations

The number of individuals included in the present study is small and a larger number is required for statistically significant results and true clinical impact. The observed large dispersion of the results warrants the examination of a large cohort in order to disambiguate if there are definite trends in the change of bifurcation geometric parameters with posture alteration. In addition, the fact that a fixation system was not possible to be used during the scanning procedure has led to a varying degree of head rotation, thus contributing to a possible large dispersion of acquired results.

The segmentation method and the smoothing technique may be optimized using alternative methods like the use of automate segmentation based in intensity thresholds. This ensures the non-existence of errors related to the human factor. Also, a different MRI protocol could be used for limited inaccuracies in the identification of the arterial wall and arterial lumen in each segment. These inaccuracies are due to low signal to noise ratio (SNR) and flow voids.

Finally, simplification assumptions used in CFD simulations such as: a) the blood modeled as a Newtonian fluid; b) the wall assumed to be rigid; and c) the fully developed flow assumption at inlet and outlets, lead to less accuracy of numerical results.

10.4 Future Work

The methodology that was followed, from MR images to CFD analysis, is well established and used to calculate the notable changes in hemodynamic features, previously cited to correlate with the development of atherogenesis and atherosclerosis. Some in-between steps of the whole procedure chain can be improved for faster and more robust results. In more detail, the first step involves the MR imaging. Better spatial resolution will help the segmentation part to construct more realistic 3D models. Also, by the end of MRI exam, if we were able to have information for both blood flow rate and geometry it would help for more accurate patient-specific modeling.

Better resolution images would make feasible the use of automate segmentation techniques based on intensity thresholds. This would improve several parameters such as: a) more realistic geometry models, b) more consistency in the extracted models, as the manual segmentation depended exclusively on the user; and c) the time would be significantly reduced.

The automated meshing, using pre-existing meshing blocks, would help in time reduction spending for each model independently. This technique would use the already estimated parameters such as: a) the mesh size, b) the element size/type, c) the mesh density on the vicinity, and d) the number of layers near wall, and with minor

adjustments it would be in position to construct fine meshes. The next part involves the CFD simulations. It would be preferable to use compliance walls rather than solid/rigid walls to reflect the reality better. Likewise, the consideration of blood as a non-Newtonian fluid would lead to more accurate results, however assuming it as Newtonian was sufficient enough for our case.

These considerations focus in the area of more accurate numerical results. Another direction for future investigation is to extend the existent research in patients with severe carotid stenosis, and in patients with renal disease who need hemodialysis therapy. The complex hemodynamics in stenotic arteries and in the area of vascular access need robust and accurate simulations in order to help towards the optimization of the design of cardiovascular implants and devices.

Bibliography

[1] J. Gillard, M. Graves, T. Hatsukami, and C. Yuan, *Carotid Disease The Role of Imaging in Diagnosis and Management*, 2007.

[2] V. L. Roger, A. S. Go, D. M. Lloyd-Jones, R. J. Adams, J. D. Berry, T. M. Brown*, et al.*, "Heart disease and stroke statistics--2011 update: a report from the American Heart Association," *Circulation,* vol. 123, pp. e18-e209, Feb 1 2011.

[3] A. S. Go, D. Mozaffarian, V. L. Roger, E. J. Benjamin, J. D. Berry, W. B. Borden*, et al.*, "Executive summary: heart disease and stroke statistics--2013 update: a report from the American Heart Association," *Circulation,* vol. 127, pp. 143-52, Jan 1 2013.

[4] M. Nichols, N. Townsend, P. Scarborough, R. Luengo-Fernandez, J. Leal, A. Gray*, et al.*, "European cardiovascular disease statistics 2012," European Society of Cardiology, Sophia Antipolis, Brussels2012.

[5] R. A. White, G. A. Sicard, R. M. Zwolak, A. N. Sidawy, M. L. Schermerhorn, R. J. Shackelton*, et al.*, "Society of vascular surgery vascular registry comparison of carotid artery stenting outcomes for atherosclerotic vs nonatherosclerotic carotid artery disease," *J Vasc Surg,* vol. 51, pp. 1116-23, May 2010.

[6] M. Fisher and S. Fieman, "Geometric factors of the bifurcation in carotid atherogenesis," *Stroke,* vol. 21, pp. 267-71, Feb 1990.

[7] U. G. R. Schulz and P. M. Rothwell, "Major Variation in Carotid Bifurcation Anatomy: A Possible Risk Factor for Plaque Development?," *Stroke,* vol. 32, pp. 2522-2529, 2001.

[8] A. M. Malek, S. L. Alper, and S. Izumo, "Hemodynamic shear stress and its role in atherosclerosis," *JAMA,* vol. 282, pp. 2035-42, Dec 1 1999.

[9] E. Cecchi, C. Giglioli, S. Valente, C. Lazzeri, G. F. Gensini, R. Abbate*, et al.*, "Role of hemodynamic shear stress in cardiovascular disease," *Atherosclerosis,* vol. 214, pp. 249-56, Feb 2011.

[10] D. L. Fry, "Acute vascular endothelial changes associated with increased blood velocity gradients," *Circ Res,* vol. 22, pp. 165-97, Feb 1968.

[11] C. G. Caro, J. M. Fitz-Gerald, and R. C. Schroter, "Atheroma and arterial wall shear. Observation, correlation and proposal of a shear dependent mass transfer mechanism for atherogenesis," *Proc R Soc Lond B Biol Sci,* vol. 177, pp. 109-59, Feb 16 1971.

[12] I. M. van der Meer, A. Iglesias del Sol, A. E. Hak, M. L. Bots, A. Hofman, and J. C. Witteman, "Risk factors for progression of atherosclerosis measured at multiple sites in the arterial tree: the Rotterdam Study," *Stroke,* vol. 34, pp. 2374-9, Oct 2003.

[13] R. Ross, "Mechanism of Disease Atherosclerosis An Inflammatory Disease," *The New England Journal of Medicine,* vol. 340, 1999.

[14] M. H. Friedman, G. M. Hutchins, C. B. Bargeron, O. J. Deters, and F. F. Mark, "Correlation between intimal thickness and fluid shear in human arteries," *Atherosclerosis,* vol. 39, pp. 425-436, 1981.

[15] D. N. Ku, D. P. Giddens, C. K. Zarins, and S. Glagov, "Pulsatile Flow and Atherosclerosis in the Human Carotid Bifurcation - Positive Correlation between Plaque Location and Low and Oscillating Shear-Stress," *Arteriosclerosis,* vol. 5, pp. 293-302, 1985.

[16] C. Cheng, D. Tempel, R. van Haperen, A. van der Baan, F. Grosveld, M. J. Daemen*, et al.*, "Atherosclerotic lesion size and vulnerability are determined by patterns of fluid shear stress," *Circulation,* vol. 113, pp. 2744-53, Jun 13 2006.

[17] R. S. Reneman, T. Arts, and A. P. Hoeks, "Wall shear stress--an important determinant of endothelial cell function and structure--in the arterial system in vivo. Discrepancies with theory," *J Vasc Res,* vol. 43, pp. 251-69, Feb 2006.

[18] C. G. Caro, "Discovery of the role of wall shear in atherosclerosis," *Arterioscler Thromb Vasc Biol,* vol. 29, pp. 158-61, Feb 2009.

[19] L. Goubergrits, K. Affeld, J. Fernandez-Britto, and L. Falcon, "Atherosclerosis and flow in carotid arteries with authentic geometries," *Biorheology,* vol. 39, pp. 519-24, 2002.

[20] Q. Long, X. Y. Xu, B. Ariff, S. A. Thom, A. D. Hughes, and A. V. Stanton, "Reconstruction of blood flow patterns in a human carotid bifurcation: a combined CFD and MRI study," *J Magn Reson Imaging,* vol. 11, pp. 299-311, Mar 2000.

[21] C. K. Zarins, D. P. Giddens, B. K. Bharadvaj, V. S. Sottiurai, R. F. Mabon, and S. Glagov, "Carotid bifurcation atherosclerosis. Quantitative correlation of plaque localization with flow velocity profiles and wall shear stress," *Circ Res,* vol. 53, pp. 502-14, Oct 1983.

[22] R. Ross, "The pathogenesis of atherosclerosis: a perspective for the 1990s," *Nature,* vol. 362, pp. 801-9, Apr 29 1993.

[23] R. Salonen and J. T. Salonen, "Progression of carotid atherosclerosis and its determinants: a population-based ultrasonography study," *Atherosclerosis,* vol. 81, pp. 33-40, Feb 1990.

[24] R. Ross, "Atherosclerosis is an inflammatory disease," *American Heart Journal,* vol. 138, pp. S419-S420, Nov 1999.

[25] P. Libby, P. M. Ridker, and A. Maseri, "Inflammation and Atherosclerosis," *Circulation,* vol. 105, pp. 1135-1143, 2002.

[26] L. Goubergrits, K. Affeld, J. Fernandez-Britto, and L. Falcon, "Atherosclerosis in the human common carotid artery. A morphometric study of 31 specimens," *Pathol Res Pract,* vol. 197, pp. 803-9, 2001.

[27] K. S. Cunningham and A. I. Gotlieb, "The role of shear stress in the pathogenesis of atherosclerosis," *Lab Invest,* vol. 85, pp. 9-23, Jan 2005.

[28] J. J. Chiu and S. Chien, "Effects of disturbed flow on vascular endothelium: pathophysiological basis and clinical perspectives," *Physiol Rev,* vol. 91, pp. 327-87, Jan 2011.

[29] M. A. Gimbrone, Jr., J. N. Topper, T. Nagel, K. R. Anderson, and G. Garcia-Cardena, "Endothelial dysfunction, hemodynamic forces, and atherogenesis," *Ann N Y Acad Sci,* vol. 902, pp. 230-9; discussion 239-40, May 2000.

[30] K. J. Moore and I. Tabas, "Macrophages in the pathogenesis of atherosclerosis," *Cell,* vol. 145, pp. 341-55, Apr 29 2011.

[31] P. Libby, "Inflammation in atherosclerosis," *Nature,* vol. 420, pp. 868-74, 2002.

[32] N. Resnick, H. Yahav, A. Shay-Salit, M. Shushy, S. Schubert, L. C. M. Zilberman*, et al.*, "Fluid shear stress and the vascular endothelium: for better and for worse," *Progress in Biophysics and Molecular Biology,* vol. 81, pp. 177-199, 2003.

[33] O. Ogunrinade, G. T. Kameya, and G. A. Truskey, "Effect of Fluid Shear Stress on the Permeability of the Arterial Endothelium," *Ann Biomed Eng,* vol. 30, pp. 430-446, 2002.

[34] D. Liepsch, "An introduction to biofluid mechanics--basic models and applications," *J Biomech,* vol. 35, pp. 415-35, Apr 2002.

[35] C. Zhang, S. Xie, S. Li, F. Pu, X. Deng, Y. Fan*, et al.*, "Flow patterns and wall shear stress distribution in human internal carotid arteries: the geometric effect on the risk for stenoses," *J Biomech,* vol. 45, pp. 83-9, Jan 3 2012.

[36] J. Knight, U. Olgac, S. C. Saur, D. Poulikakos, W. Marshall, Jr., P. C. Cattin*, et al.*, "Choosing the optimal wall shear parameter for the prediction of plaque location-A

patient-specific computational study in human right coronary arteries," *Atherosclerosis,* vol. 211, pp. 445-50, Aug 2010.

[37] F. Rikhtegar, J. A. Knight, U. Olgac, S. C. Saur, D. Poulikakos, W. Marshall, Jr*., et al.*, "Choosing the optimal wall shear parameter for the prediction of plaque location-A patient-specific computational study in human left coronary arteries," *Atherosclerosis,* vol. 221, pp. 432-7, Apr 2012.

[38] M. R. Kaazempur-Mofrad, A. G. Isasi, H. F. Younis, R. C. Chan, D. P. Hinton, G. Sukhova*, et al.*, "Characterization of the atherosclerotic carotid bifurcation using MRI, finite element modeling, and histology," *Annals of Biomedical Engineering,* vol. 32, pp. 932-946, Jul 2004.

[39] V. Peiffer, S. J. Sherwin, and P. D. Weinberg, "Does low and oscillatory wall shear stress correlate spatially with early atherosclerosis? A systematic review," *Cardiovasc Res,* Apr 4 2013.

[40] P. S. Tsao, N. P. Lewis, S. Alpert, and J. P. Cooke, "Exposure to shear stress alters endothelial adhesiveness. Role of nitric oxide," *Circulation,* vol. 92, pp. 3513-9, Dec 15 1995.

[41] O. Araim, A. Chen, and B. Sumpio, "Hemodynamic Forces Effects on Atherosclerosis," *Eurekah Bioscience,* vol. 1, pp. 39-46, 2005.

[42] S. J. L. Bakker and R. O. B. Gans, "About the role of shear stress in atherogenesis," *Cardiovascular Research,* vol. 45, pp. 270-272, Jan 14 2000.

[43] J. P. Cooke and V. J. Dzau, "Nitric oxide synthase: role in the genesis of vascular disease," *Annu Rev Med,* vol. 48, pp. 489-509, 1997.

[44] E. Metaxa, H. Meng, S. R. Kaluvala, M. P. Szymanski, R. A. Paluch, and J. Kolega, "Nitric oxide-dependent stimulation of endothelial cell proliferation by sustained high flow," *Am J Physiol Heart Circ Physiol,* vol. 295, pp. H736-42, Aug 2008.

[45] X. Bao, C. Lu, and J. A. Frangos, "Temporal Gradient in Shear But Not Steady Shear Stress Induces PDGF-A and MCP-1 Expression in Endothelial Cells : Role of NO, NF B, and egr-1," *Arteriosclerosis, Thrombosis, and Vascular Biology,* vol. 19, pp. 996-1003, 1999.

[46] J. F. Polak, S. D. Person, G. S. Wei, A. Godreau, D. R. Jacobs, Jr., A. Harrington*, et al.*, "Segment-specific associations of carotid intima-media thickness with cardiovascular risk factors: the Coronary Artery Risk Development in Young Adults (CARDIA) study," *Stroke,* vol. 41, pp. 9-15, Jan 2010.

[47] F. Eichler, O. Ipsiroglu, T. Arif, C. Popow, H. Heinzl, M. Urschitz*, et al.*, "Position dependent changes of cerebral blood flow velocities in premature infants," *Eur J Pediatr,* vol. 160, pp. 633-9, Oct 2001.

[48] G. Dimitriou, A. Greenough, L. Pink, A. McGhee, A. Hickey, and G. F. Rafferty, "Effect of posture on oxygenation and respiratory muscle strength in convalescent infants," *Arch Dis Child Fetal Neonatal Ed,* vol. 86, pp. F147-50, May 2002.

[49] F. P. Glor, B. Ariff, A. D. Hughes, P. R. Verdonck, D. C. Barratt, A. D. Augst*, et al.*, "Influence of head position on carotid hemodynamics in young adults," *Am J Physiol Heart Circ Physiol,* vol. 287, pp. H1670-81, Oct 2004.

[50] C. G. Caro, D. J. Doorly, M. Tarnawski, K. T. Scott, Q. Long, and D. C. L., "Non-planar curvature and branching of arteries and non-planar-type flow," *Proceedings Mathematical, Physical and Engineering Science,* vol. 452, pp. 185-197, 1996.

[51] A. S. Anayiotos, S. A. Jones, D. P. Giddens, S. Glagov, and C. K. Zarins, "Shear-Stress at a Compliant Model of the Human Carotid Bifurcation," *Journal of Biomechanical Engineering-Transactions of the Asme,* vol. 116, pp. 98-106, Feb 1994.

[52] D. N. Ku, "Blood flow in arteries," *Annual Review of Fluid Mechanics,* vol. 29, pp. 399-434, 1997.

[53] K. Perktold and G. Rappitsch, "Computer simulation of local blood flow and vessel mechanics in a compliant carotid artery bifurcation model," *J Biomech,* vol. 28, pp. 845-56, Jul 1995.

[54] K. Perktold, R. O. Peter, M. Resch, and G. Langs, "Pulsatile non-Newtonian blood flow in three-dimension carotid bifurcation models: a numerical study of flow phenomena under different bifurcation angles," *J Biomed Eng,* vol. 13, pp. 507-515, May 1991.

[55] K. Perktold, M. Resch, and R. O. Peter, "Three-dimensional numerical analysis of pulsatile flow and wall shear stress in the carotid artery bifurcation," *J Biomech,* vol. 24, pp. 409-20, 1991.

[56] C. A. Taylor and D. A. Steinman, "Image-based modeling of blood flow and vessel wall dynamics: applications, methods and future directions: Sixth International Bio-Fluid Mechanics Symposium and Workshop, March 28-30, 2008 Pasadena, California," *Ann Biomed Eng,* vol. 38, pp. 1188-203, Mar 2010.

[57] D. A. Steinman and C. A. Taylor, "Flow imaging and computing: large artery hemodynamics," *Ann Biomed Eng,* vol. 33, pp. 1704-9, Dec 2005.

[58] C. A. Taylor and M. T. Draney, "Experimental and Computational Methods in Cardiovascular Fluid Mechanics," *Annual Review of Fluid Mechanics,* vol. 36, pp. 197-231, 2004.

[59] L. Antiga, M. Piccinelli, L. Botti, B. Ene-Iordache, A. Remuzzi, and D. A. Steinman, "An image-based modeling framework for patient-specific computational hemodynamics," *Med Biol Eng Comput,* vol. 46, pp. 1097-112, Nov 2008.

[60] D. A. Steinman, J. B. Thomas, H. M. Ladak, J. S. Milner, B. K. Rutt, and J. D. Spence, "Reconstruction of carotid bifurcation hemodynamics and wall thickness using computational fluid dynamics and MRI," *Magn Reson Med,* vol. 47, pp. 149-59, Jan 2002.

[61] S. Z. Zhao, X. Y. Xu, A. D. Hughes, S. A. Thom, A. V. Stanton, B. Ariff*, et al.*, "Blood fow and vessel mechanics in a physiologically realistic model of a human carotid arterial bifurcation," *Journal of Biomechanics,* vol. 33, pp. 975-984, Feb 2000.

[62] I. Marshall, S. Zhao, P. Papathanasopoulou, P. Hoskins, and Y. Xu, "MRI and CFD studies of pulsatile flow in healthy and stenosed carotid bifurcation models," *J Biomech,* vol. 37, pp. 679-87, May 2004.

[63] M. R. Kaazempur-Mofrad, M. Bathe, H. Karcher, H. F. Younis, H. C. Seong, E. B. Shim*, et al.*, "Role of simulation in understanding biological systems," *Computers & Structures,* vol. 81, pp. 715-726, May 2003.

[64] H. F. Younis, M. R. Kaazempur-Mofrad, R. C. Chan, A. G. Isasi, D. P. Hinton, A. H. Chau*, et al.*, "Hemodynamics and wall mechanics in human carotid bifurcation and its consequences for atherogenesis: investigation of inter-individual variation," *Biomech Model Mechanobiol,* vol. 3, pp. 17-32, Sep 2004.

[65] P. B. Bijari, L. Antiga, B. A. Wasserman, and D. A. Steinman, "Scan-Rescan reproducibility of carotid bifurcation geometry from routine contrast-enhanced MR angiography," *J Magn Reson Imaging,* vol. 33, pp. 482-9, Feb 2011.

[66] J. B. Thomas, J. S. Milner, B. K. Rutt, and D. A. Steinman, "Reproducibility of Image-Based Computational Fluid Dynamics Models of the Human Carotid Bifurcation," *Ann Biomed Eng,* vol. 31, pp. 132-141, 2003.

[67] J. A. Moore, D. A. Steinman, D. W. Holdsworth, and C. R. Ethier, "Accuracy of computational hemodynamics in complex arterial geometries reconstructed from magnetic resonance imaging," *Ann Biomed Eng,* vol. 27, pp. 32-41, Jan-Feb 1999.

[68] J. R. Cebral, P. J. Yim, R. Lohner, O. Soto, and P. L. Choyke, "Blood flow modeling in carotid arteries with computational fluid dynamics and MR imaging," *Acad Radiol,* vol. 9, pp. 1286-99, Nov 2002.

[69] D. A. Steinman, "Image-based computational fluid dynamics modeling in realistic arterial geometries," *Ann Biomed Eng,* vol. 30, pp. 483-97, Apr 2002.

[70] J. S. Milner, J. A. Moore, B. K. Rutt, and D. A. Steinman, "Hemodynamics of human carotid artery bifurcations: computational studies with models reconstructed from magnetic resonance imaging of normal subjects," *J Vasc Surg,* vol. 28, pp. 143-56, Jul 1998.

[71] L. Goubergrits, U. Kertzscher, B. Schoneberg, E. Wellnhofer, C. Petz, and H. C. Hege, "CFD analysis in an anatomically realistic coronary artery model based on non-invasive 3D imaging: comparison of magnetic resonance imaging with computed tomography," *Int J Cardiovasc Imaging,* vol. 24, pp. 411-21, Apr 2008.

[72] S. Z. Zhao, P. Papathanasopoulou, Q. Long, I. Marshall, and X. Y. Xu, "Comparative study of magnetic resonance imaging and image-based computational fluid dynamics for quantification of pulsatile flow in a carotid bifurcation phantom," *Ann Biomed Eng,* vol. 31, pp. 962-71, Sep 2003.

[73] R. Botnar, G. Rappitsch, M. B. Scheidegger, D. Liepsch, K. Perktold, and P. Boesiger, "Hemodynamics in the carotid artery bifurcation: a comparison between numerical simulations and in vitro MRI measurements," *Journal of Biomechanics,* vol. 33, pp. 137-144, Feb 2000.

[74] F. P. Glor, B. Ariff, A. D. Hughes, L. A. Crowe, P. R. Verdonck, D. C. Barratt*, et al.*, "Image-based carotid flow reconstruction: a comparison between MRI and ultrasound," *Physiological Measurement,* vol. 25, pp. 1495-1509, Dec 2004.

[75] F. P. Glor, B. Ariff, L. A. Crowe, A. D. Hughes, P. L. Cheong, S. A. M. Thom*, et al.*, "Carotid geometry reconstruction: a comparison between MRI and ultrasound," *Medical Physics,* vol. 30, pp. 3251-3261, Dec 2003.

[76] F. P. Glor, Q. Long, A. D. Hughes, A. D. Augst, B. Ariff, S. A. M. Thom*, et al.*, "Reproducibility Study of Magnetic Resonance Image-Based Computational Fluid Dynamics Prediction of Carotid Bifurcation Flow," *Annals of Biomedical Engineering,* vol. 31, pp. 142-151, 2003.

[77] D. T. Miller, P. M. Ridker, P. Libby, and D. J. Kwiatkowski, "Atherosclerosis: the path from genomics to therapeutics," *J Am Coll Cardiol,* vol. 49, pp. 1589-99, Apr 17 2007.

[78] C. A. Taylor and J. D. Humphrey, "Open Problems in Computational Vascular Biomechanics: Hemodynamics and Arterial Wall Mechanics," *Comput Methods Appl Mech Eng,* vol. 198, pp. 3514-3523, Sep 15 2009.

[79] S. Hyun, C. Kleinstreuer, and J. P. Archie, Jr., "Computational particle-hemodynamics analysis and geometric reconstruction after carotid endarterectomy," *Comput Biol Med,* vol. 31, pp. 365-84, Sep 2001.

[80] M. Khakpour and K. Vafai, "Critical assessment of arterial transport models," *International Journal of Heat and Mass Transfer,* vol. 51, pp. 807-822, Feb 2008.

[81] H. Gray, *Anatomy of the human body*, 22d ed. Phila., N.Y., 1930.

[82] Guyton and Hall, *Textbook Of Medical Physiology* 11th ed.: Elsevier Inc, 2006.

[83] C. R. Ethier, C. A. Simmons, and Knovel (Firm). (2007). *Introductory biomechanics from cells to organisms*. Available: http://www.knovel.com/knovel2/Toc.jsp?BookID=2341

[84] J. D. Bronzino, *The biomedical engineering handbook*, 2nd ed. Boca Raton, FL: CRC Press, 2000.

[85] N. Yang and K. Vafai, "Modeling of low-density lipoprotein (LDL) transport in the artery—effects of hypertension," *International Journal of Heat and Mass Transfer,* vol. 49, pp. 850-867, 2006.
[86] M. Zamir, "On fractal properties of arterial trees," *Journal of Theoretical Biology,* vol. 197, pp. 517-526, Apr 21 1999.
[87] J. K.-J. Li, *Dynamics of the vascular system*. River Edge, N.J.: World Scientific, 2004.
[88] T. F. Sherman, "On Connecting Large Vessels to Small The Meaning of Murrays Law," *J. Gen. Physiol.,* vol. 78, pp. 431-453, Oct 1981.
[89] C. D. Murray, "The Physiological Principle of Minimum Work Applied to the Angle of Branching of Arteries," *J Gen Physiol,* vol. 9, pp. 835-41, Jul 20 1926.
[90] C. D. Murray, "The Physiological Principle of Minimum Work: I. The Vascular System and the Cost of Blood Volume," *Proc Natl Acad Sci U S A,* vol. 12, pp. 207-14, Mar 1926.
[91] M. Zamir and N. Brown, "Arterial branching in various parts of the cardiovascular system," *Am J Anat,* vol. 163, pp. 295-307, Apr 1982.
[92] R. J. Beare, G. Das, M. Ren, W. Chong, M. D. Sinnott, J. E. Hilton*, et al.*, "Does the principle of minimum work apply at the carotid bifurcation: a retrospective cohort study," *BMC Med Imaging,* vol. 11, p. 17, 2011.
[93] C. Cheng, F. Helderman, D. Tempel, D. Segers, B. Hierck, R. Poelmann*, et al.*, "Large variations in absolute wall shear stress levels within one species and between species," *Atherosclerosis,* vol. 195, pp. 225-35, Dec 2007.
[94] M. H. Friedman, "Variability of arterial wall shear stress, its dependence on vessel diameter and implications for Murray's Law," *Atherosclerosis,* vol. 203, pp. 47-8, Mar 2009.
[95] R. P. Vito and S. A. Dixon, "Blood vessel constitutive models-1995-2002," *Annu Rev Biomed Eng,* vol. 5, pp. 413-39, 2003.
[96] A. V. Kamenskiy, Y. A. Dzenis, J. N. MacTaggart, T. G. Lynch, S. A. Jaffar Kazmi, and Pipinos, II, "Nonlinear mechanical behavior of the human common, external, and internal carotid arteries in vivo," *J Surg Res,* vol. 176, pp. 329-36, Jul 2012.
[97] D. F. Moore, G. Altarescu, R. Pursley, U. Campia, J. A. Panza, E. Dimitriadis*, et al.*, "Arterial wall properties and Womersley flow in Fabry disease," *BMC Cardiovasc Disord,* vol. 2, p. 1, Jan 2002.
[98] V. Kasyanov, I. Ozolanta, B. Purinya, A. Ozols, and V. Kancevich, "Compliance of a biocomposite vascular tissue in longitudinal and circumferential directions as a basis for creating artificial subsitutes," *Mechanics of Composite materials,* vol. 39, pp. 347-358, 2003.
[99] N. Westerhof, N. Stergiopulos, and M. I. M. Noble, *Snapshots of hemodynamics : an aid for clinical research and graduate education*. New York, NY: Springer, 2005.
[100] T. E. Carew, R. N. Vaishnav, and D. J. Patel, "Compressibility of the arterial wall," *Circ Res,* vol. 23, pp. 61-8, Jul 1968.
[101] N. Westerhof, J. W. Lankhaar, and B. E. Westerhof, "The arterial Windkessel," *Med Biol Eng Comput,* vol. 47, pp. 131-41, Feb 2009.
[102] J. Seong, B. B. Lieber, and A. K. Wakhloo, "Morphological age-dependent development of the human carotid bifurcation," *J Biomech,* vol. 38, pp. 453-65, Mar 2005.
[103] Z. Ding, K. Wang, J. Li, and X. Cong, "Flow field and oscillatory shear stress in a tuning-fork-shaped model of the average human carotid bifurcation," *J Biomech,* vol. 34, pp. 1555-62, Dec 2001.

[104] V. A. Kumar, L. P. Brewster, J. M. Caves, and E. L. Chaikof, "Tissue Engineering of Blood Vessels: Functional Requirements, Progress, and Future Challenges," *Cardiovasc Eng Technol,* vol. 2, pp. 137-148, Sep 1 2011.

[105] M. Etesami, Y. Hoi, D. A. Steinman, S. K. Gujar, A. E. Nidecker, B. C. Astor*, et al.*, "Comparison of carotid plaque ulcer detection using contrast-enhanced and time-of-flight MRA techniques," *AJNR Am J Neuroradiol,* vol. 34, pp. 177-84, Jan 2013.

[106] J. M. Cai, T. S. Hatsukami, M. S. Ferguson, R. Small, N. L. Polissar, and C. Yuan, "Classification of human carotid atherosclerotic lesions with in vivo multicontrast magnetic resonance imaging," *Circulation,* vol. 106, pp. 1368-73, Sep 10 2002.

[107] L. Wagenknecht, B. Wasserman, L. Chambless, J. Coresh, A. Folsom, T. Mosley*, et al.*, "Correlates of carotid plaque presence and composition as measured by MRI: the Atherosclerosis Risk in Communities Study," *Circ Cardiovasc Imaging,* vol. 2, pp. 314-22, Jul 2009.

[108] T. Saam, J. Cai, L. Ma, Y. Q. Cai, M. S. Ferguson, N. L. Polissar*, et al.*, "Comparison of symptomatic and asymptomatic atherosclerotic carotid plaque features with in vivo MR imaging," *Radiology,* vol. 240, pp. 464-72, Aug 2006.

[109] L. Waite and J. Fine, *Applied Biofluid Mechanics*: Mc-Graw Hill, 2007.

[110] I. Chatziprodromou, A. Tricoli, D. Poulikakos, and Y. Ventikos, "Haemodynamics and wall remodelling of a growing cerebral aneurysm: a computational model," *J Biomech,* vol. 40, pp. 412-26, 2007.

[111] H. Meng, Z. Wang, Y. Hoi, L. Gao, E. Metaxa, D. D. Swartz*, et al.*, "Complex hemodynamics at the apex of an arterial bifurcation induces vascular remodeling resembling cerebral aneurysm initiation," *Stroke,* vol. 38, pp. 1924-31, Jun 2007.

[112] H. Meng, D. D. Swartz, Z. Wang, Y. Hoi, J. Kolega, E. M. Metaxa*, et al.*, "A model system for mapping vascular responses to complex hemodynamics at arterial bifurcations in vivo," *Neurosurgery,* vol. 59, pp. 1094-100; discussion 1100-1, Nov 2006.

[113] B. L. Zaret, M. Marvin, and L. S. C., *Yale Heart Book* 1 st edition ed.: William Morrow & Co, 1992.

[114] M. Lawrence-Brown, B. M. Stanley, Z. Sun, J. B. Semmens, and K. Liffman, "Stress and strain behaviour modelling of the carotid bifurcation," *ANZ J Surg,* vol. 81, pp. 810-6, Nov 2011.

[115] F. M. White, *Fluid Mechanics*, 4th ed.: McGraw-Hill 1998.

[116] M. Zamir, *The Physics of Pulsatile Flow*: Springer, 2000.

[117] M. Zamir, *The Physics of Coronary Blood Flow*: Springer, 2005.

[118] M. P. J. H. Ferziger, "Computational Methods for Fluid Dynamics," 3rd ed: Springer, 2002.

[119] J. M. Dolan, J. Kolega, and H. Meng, "High wall shear stress and spatial gradients in vascular pathology: a review," *Ann Biomed Eng,* vol. 41, pp. 1411-27, Jul 2013.

[120] H. A. Himburg and M. H. Friedman, "Correspondence of low mean shear and high harmonic content in the porcine iliac arteries," *J Biomech Eng,* vol. 128, pp. 852-6, Dec 2006.

[121] H. A. Himburg, S. E. Dowd, and M. H. Friedman, "Frequency-dependent response of the vascular endothelium to pulsatile shear stress," *Am J Physiol Heart Circ Physiol,* vol. 293, pp. H645-53, Jul 2007.

[122] S. W. Lee, L. Antiga, and D. A. Steinman, "Correlations among indicators of disturbed flow at the normal carotid bifurcation," *J Biomech Eng,* vol. 131, p. 061013, Jun 2009.

[123] S. Z. Zhao, B. Ariff, Q. Long, A. D. Hughes, S. A. Thom, A. V. Stanton*, et al.*, "Inter-individual variations in wall shear stress and mechanical stress distributions at the

carotid artery bifurcation of healthy humans," *Journal of Biomechanics,* vol. 35, pp. 1367-1377, Oct 2002.

[124] S. Hodis and M. Zamir, "Mechanical events within the arterial wall: The dynamic context for elastin fatigue," *J Biomech,* vol. 42, pp. 1010-6, May 29 2009.

[125] E. P. Efstathopoulos, G. Patatoukas, I. Pantos, O. Benekos, D. Katritsis, and N. L. Kelekis, "Wall shear stress calculation in ascending aorta using phase contrast magnetic resonance imaging. Investigating effective ways to calculate it in clinical practice," *Phys Med,* vol. 24, pp. 175-81, Dec 2008.

[126] J. Pantos, E. Efstathopoulos, and D. G. Katritsis, "Vascular wall shear stress in clinical practice," *Curr Vasc Pharmacol,* vol. 5, pp. 113-9, Apr 2007.

[127] A. M. Masaryk, R. Frayne, O. Unal, E. Krupinski, and C. M. Strother, "In vitro and in vivo comparison of three MR measurement methods for calculating vascular shear stress in the internal carotid artery," *AJNR Am J Neuroradiol,* vol. 20, pp. 237-45, Feb 1999.

[128] B. D. Gelfand, F. H. Epstein, and B. R. Blackman, "Spatial and spectral heterogeneity of time-varying shear stress profiles in the carotid bifurcation by phase-contrast MRI," *J Magn Reson Imaging,* vol. 24, pp. 1386-92, Dec 2006.

[129] J. L. Carvalho, J. F. Nielsen, and K. S. Nayak, "Feasibility of in vivo measurement of carotid wall shear rate using spiral Fourier velocity encoded MRI," *Magn Reson Med,* vol. 63, pp. 1537-47, Jun 2010.

[130] A. M. Shaaban and A. J. Duerinckx, "Wall shear stress and early atherosclerosis: A review," *American Journal of Roentgenology,* vol. 174, pp. 1657-1665, Jun 2000.

[131] S. P. Wu, S. Ringgaard, S. Oyre, M. S. Hansen, S. Rasmus, and E. M. Pedersen, "Wall shear rates differ between the normal carotid, femoral, and brachial arteries: an in vivo MRI study," *J Magn Reson Imaging,* vol. 19, pp. 188-93, Feb 2004.

[132] S. K. Samijo, J. M. Willigers, R. Barkhuysen, P. J. E. H. M. Kitslaar, R. S. Reneman, P. J. Brands*, et al.*, "Wall shear stress in the human common carotid artery as function of age and gender," *Cardiovascular Research,* vol. 39, pp. 515-522, Aug 1998.

[133] S. Oyre, S. Ringgaard, S. Kozerke, W. P. Paaske, M. Erlandsen, P. Boesiger*, et al.*, "Accurate noninvasive quantitation of blood flow, cross-sectional lumen vessel area and wall shear stress by three-dimensional paraboloid modeling of magnetic resonance imaging velocity data," *J Am Coll Cardiol,* vol. 32, pp. 128-34, Jul 1998.

[134] M. Ojha, "Wall shear stress temporal gradient and anastomotic intimal hyperplasia," *Circ Res,* vol. 74, pp. 1227-31, Jun 1994.

[135] M. A. Haidekker, C. R. White, and J. A. Frangos, "Analysis of temporal shear stress gradients during the onset phase of flow over a backward-facing step," *J Biomech Eng,* vol. 123, pp. 455-63, Oct 2001.

[136] M. Lei, C. Kleinstreuer, and G. A. Truskey, "A focal stress gradient-dependent mass transfer mechanism for atherogenesis in branching arteries," *Med Eng Phys,* vol. 18, pp. 326-32, Jun 1996.

[137] S. Hyun, C. Kleinstreuer, and J. P. Archie, Jr., "Hemodynamics analyses of arterial expansions with implications to thrombosis and restenosis," *Med Eng Phys,* vol. 22, pp. 13-27, Jan 2000.

[138] M. Lei, J. P. Archie, and C. Kleinstreuer, "Computational design of a bypass graft that minimizes wall shear stress gradients in the region of the distal anastomosis," *Journal of Vascular Surgery,* vol. 25, pp. 637-646, Apr 1997.

[139] Y. Papaharilaou, D. J. Doorly, and S. J. Sherwin, "The influence of out-of-plane geometry on pulsatile flow within a distal end-to-side anastomosis," *J Biomech,* vol. 35, pp. 1225-39, Sep 2002.

[140] H. A. Himburg, D. M. Grzybowski, A. L. Hazel, J. A. LaMack, X. M. Li, and M. H. Friedman, "Spatial comparison between wall shear stress measures and porcine arterial endothelial permeability," *Am J Physiol Heart Circ Physiol,* vol. 286, pp. H1916-22, May 2004.

[141] P. P. Ma, X. M. Li, and D. N. Ku, "Convective mass transfer at the carotid bifurcation," *Journal of Biomechanics,* vol. 30, pp. 565-571, Jun 1997.

[142] U. Morbiducci, R. Ponzini, M. Grigioni, and A. Redaelli, "Helical flow as fluid dynamic signature for atherogenesis risk in aortocoronary bypass. A numeric study," *J Biomech,* vol. 40, pp. 519-34, 2007.

[143] H. K. Moffatt and A. Tsinober, "Helicity in Laminar and Turbulent-Flow," *Annual Review of Fluid Mechanics,* vol. 24, pp. 281-312, 1992.

[144] D. Gallo, D. A. Steinman, P. B. Bijari, and U. Morbiducci, "Helical flow in carotid bifurcation as surrogate marker of exposure to disturbed shear," *J Biomech,* vol. 45, pp. 2398-404, Sep 21 2012.

[145] L. Shtilman, E. Levich, S. A. Orszag, R. B. Pelz, and A. Tsinober, "On the Role of Helicity in Complex Fluid-Flows," *Physics Letters A,* vol. 113, pp. 32-37, 1985.

[146] Y. Shimogonya, T. Ishikawa, Y. Imai, N. Matsuki, and T. Yamaguchi, "Can temporal fluctuation in spatial wall shear stress gradient initiate a cerebral aneurysm? A proposed novel hemodynamic index, the gradient oscillatory number (GON)," *J Biomech,* vol. 42, pp. 550-4, Mar 11 2009.

[147] Δ. Κουτσούρης, Κ. Νικήτα, and Σ. Παυλόπουλος, *Ιατρικά Απεικονιστικά Συστήματα*: Τζιόλα, 2004.

[148] P. C. Lauterbur, "Image formation by induced local interactions. Examples employing nuclear magnetic resonance. 1973," *Clin Orthop Relat Res,* pp. 3-6, Jul 1989.

[149] P. K. Grannell and P. Mansfield, "Microscopy in vivo by nuclear magnetic resonance," *Phys Med Biol,* vol. 20, pp. 477-82, May 1975.

[150] R. Damadian, M. Goldsmith, and L. Minkoff, "NMR in cancer: XVI. FONAR image of the live human body," *Physiol Chem Phys,* vol. 9, pp. 97-100, 108, 1977.

[151] C. Constantinides, *Introduction to Magnetic Resonance Course Lecture Booklet, Version 2.0*: Department of Mechanical and Manufacturing Engineering, University of Cyprus, 2006.

[152] M. Lombardi and C. Bartolozzi, *MRI of the Heart and Vessels*: Springer, 2004.

[153] M. Xavie, A. Lalande, P. M. Walker, C. Boichot, A. Cochet, O. Bouchot*, et al.*, "Dynamic 4D Blood Flow Representation in the Aorta and Analysis from Cine-MRI in Patients," *Computers in Cardiology,* vol. 34, pp. 375-378, 2007.

[154] P. A. Yushkevich, J. Piven, H. C. Hazlett, R. G. Smith, S. Ho, J. C. Gee*, et al.*, "User-guided 3D active contour segmentation of anatomical structures: significantly improved efficiency and reliability," *Neuroimage,* vol. 31, pp. 1116-28, Jul 1 2006.

[155] L. Antiga and D. A. Steimman, "Robust and Objective Decompositionand Mapping of Bifurcating Vessels," *IEEE Trans Med Imaging,* vol. 23, pp. 704-713, Jun 2004.

[156] E. Heiberg, J. Sjogren, M. Ugander, M. Carlsson, H. Engblom, and H. Arheden, "Design and validation of Segment--freely available software for cardiovascular image analysis," *BMC Med Imaging,* vol. 10, p. 1, 2010.

[157] T. Hassan, E. V. Timofeev, T. Saito, H. Shimizu, M. Ezura, T. Tominaga*, et al.*, "Computational replicas: Anatomic reconstructions of cerebral vessels as volume numerical grids at three-dimensional angiography," *American Journal of Neuroradiology,* vol. 25, pp. 1356-1365, Sep 2004.

[158] G. Taubin, "A Signal Processing Approach To Fair Surface Design," in *Proc. 22nd Annual Conference on Computer Graphics and Interactive Techniques (SIGGRAPH 1995)*, 1995, pp. 351-358.

[159] Q. Long, B. Ariff, S. Z. Zhao, S. A. Thom, A. D. Hughes, and X. Y. Xu, "Reproducibility study of 3D geometrical reconstruction of the human carotid bifurcation from magnetic resonance images," *Magn Reson Med,* vol. 49, pp. 665-74, Apr 2003.

[160] M. H. Friedman, O. J. Deters, F. F. Mark, C. B. Bargeron, and G. M. Hutchins, "Arterial Geometry Affects Hemodynamics - a Potential Risk Factor for Atherosclerosis," *Atherosclerosis,* vol. 46, pp. 225-231, 1983.

[161] D. R. Wells, J. P. Archie, Jr., and C. Kleinstreuer, "Effect of carotid artery geometry on the magnitude and distribution of wall shear stress gradients," *J Vasc Surg,* vol. 23, pp. 667-78, Apr 1996.

[162] E. Bullitt, G. Gerig, S. M. Pizer, W. Lin, and S. R. Aylward, "Measuring tortuosity of the intracerebral vasculature from MRA images," *IEEE Trans Med Imaging,* vol. 22, pp. 1163-71, Sep 2003.

[163] M. Sitzer, D. Puac, A. Buehler, D. A. Steckel, S. von Kegler, H. S. Markus*, et al.*, "Internal carotid artery angle of origin: a novel risk factor for early carotid atherosclerosis," *Stroke,* vol. 34, pp. 950-5, Apr 2003.

[164] S. W. Lee, L. Antiga, J. D. Spence, and D. A. Steinman, "Geometry of the carotid bifurcation predicts its exposure to disturbed flow," *Stroke,* vol. 39, pp. 2341-7, Aug 2008.

[165] M. Markl, F. Wegent, T. Zech, S. Bauer, C. Strecker, M. Schumacher*, et al.*, "In vivo wall shear stress distribution in the carotid artery: effect of bifurcation geometry, internal carotid artery stenosis, and recanalization therapy," *Circ Cardiovasc Imaging,* vol. 3, pp. 647-55, Nov 2010.

[166] A. Harloff and M. Markl, "In vivo wall shear stress patterns in carotid bifurcations assessed by 4D MRI," *Perspectives in Medicine,* vol. 1, pp. 137-138, 2012.

[167] P. B. Bijari, L. Antiga, D. Gallo, B. A. Wasserman, and D. A. Steinman, "Improved prediction of disturbed flow via hemodynamically-inspired geometric variables," *J Biomech,* vol. 45, pp. 1632-7, Jun 1 2012.

[168] N. Aristokleous, I. Seimenis, Y. Papaharilaou, G. C. Georgiou, B. C. Brott, E. Eracleous*, et al.*, "Effect of posture change on the geometric features of the healthy carotid bifurcation," *IEEE Trans Inf Technol Biomed,* vol. 15, pp. 148-54, Jan 2011.

[169] Q. Zhang, D. A. Steinman, and M. H. Friedman, "Use of factor analysis to characterize arterial geometry and predict hemodynamic risk: application to the human carotid bifurcation," *J Biomech Eng,* vol. 132, p. 114505, Nov 2010.

[170] E. King, X. Y. Xu, A. D. Hughes, Q. Long, S. A. Thom, and K. H. Parker, "Quantification of the non-planarity of the human carotid bifurcation," *Biorheology,* vol. 39, pp. 419-24, 2002.

[171] H. Sun, B. D. Kuban, P. Schmalbrock, and M. H. Friedman, "Measurement of the geometric parameters of the aortic bifurcation from magnetic resonance images," *Ann Biomed Eng,* vol. 22, pp. 229-39, May-Jun 1994.

[172] J. Alastruey, J. H. Siggers, V. Peiffer, D. J. Doorly, and S. J. Sherwin, "Reducing the data: Analysis of the role of vascular geometry on blood flow patterns in curved vessels," *Physics of Fluids,* vol. 24, p. 031902, Mar 2012.

[173] M. Piccinelli, A. Veneziani, D. A. Steimman, A. Remuzzi, and L. Antiga, "A framework for geometric analysis of vascular structures: applications to cerebral aneurysm," *IEEE Transactions on Medical Imaging,* vol. 28, pp. 1141-1155, 2009.

[174] J. B. Thomas, J. S. Milner, and D. A. Steinman, "On the influence of vessel planarity on local hemodynamics at the human carotid bifurcation," *Biorheology,* vol. 39, pp. 443-448, 2002.
[175] J. B. Thomas, L. Antiga, S. L. Che, J. S. Milner, D. A. Steinman, J. D. Spence*, et al.*, "Variation in the carotid bifurcation geometry of young versus older adults: implications for geometric risk of atherosclerosis," *Stroke,* vol. 36, pp. 2450-6, Nov 2005.
[176] O. J. Dunn and V. A. Clark, *Basic Statistics-A Primer for the Biomedical Sciences*, 4th ed ed.: Wiley, 2009.
[177] "R Development Core Team. R: A Language and Environment for Statistical Computing," ed. Vienna Austria: R Foundation for Statistical Computing, http://www.r-project.org, 2005.
[178] L. Goubergrits, K. Affeld, J. Fernandez-Britto, and L. Falcon, "Geometry of the human common carotid artery. A vessel cast study of 86 specimens," *Pathol Res Pract,* vol. 198, pp. 543-51, 2002.
[179] K. Affeld, L. Goubergrits, J. Fernandez-Britto, and L. Falcon, "Variability of the geometry of the human common carotid artery. A vessel cast study of 31 specimens," *Pathol Res Pract,* vol. 194, pp. 597-602, 1998.
[180] T. Gohil, R. H. P. McGregor, D. Szczerba, K. Burckhardt, K. Muralidhar, and G. Szekely, "Simulation of oscillatory flow in an aortic bifurcation using FVM and FEM: A comparative study of implementation strategies," *International Journal for Numerical Methods in Fluids,* vol. 66, pp. 1037-1067, Jul 20 2011.
[181] ANSYS, *ICEM CFD 12.0 User Manual*: ANSYS Inc., 2009.
[182] F. J. Thompson, B. K. Soni, and N. P. Weatherill, *Handbook of Grid Generation*. Boca Raton, FL: CRC Press, 1999.
[183] E. Makris, P. Neofytou, S. Tsangaris, and C. Housiadas, "A novel method for the generation of multi-block computational structured grids from medical imaging of arterial bifurcations," *Medical Engineering and Physics,* vol. 34, pp. 1157-1166, Oct 2012.
[184] V. D. Liseimin, *A Computational Differential Geometry Approach to Grid Generation*, 1 ed.: Springer, 2003.
[185] L. Antiga, B. Ene-Iordache, L. Caverni, G. P. Cornalba, and A. Remuzzi, "Geometric reconstruction for computational mesh generation of arterial bifurcation from CT angiography," *Comput Med Imaging Graph,* vol. 26, pp. 227-235, 2002.
[186] G. De Santis, M. De Beule, K. Van Canneyt, P. Segers, P. Verdonck, and B. Verhegghe, "Full-hexahedral structured meshing for image-based computational vascular modeling," *Med Eng Phys,* vol. 33, pp. 1318-25, Dec 2011.
[187] S. Hodis, S. Uthamaraj, A. L. Smith, K. D. Dennis, D. F. Kallmes, and D. Dragomir-Daescu, "Grid convergence errors in hemodynamic solution of patient-specific cerebral aneurysms," *J Biomech,* vol. 45, pp. 2907-13, Nov 15 2012.
[188] U. Olgac, D. Poulikakos, S. C. Saur, H. Alkadhi, and V. Kurtcuoglu, "Patient-specific three-dimensional simulation of LDL accumulation in a human left coronary artery in its healthy and atherosclerotic states," *Am J Physiol Heart Circ Physiol,* vol. 296, pp. H1969-82, Jun 2009.
[189] S. W. Lee and D. A. Steinman, "On the relative importance of rheology for image-based CFD models of the carotid bifurcation," *J Biomech Eng,* vol. 129, pp. 273-8, Apr 2007.
[190] R. Balossino, G. Pennati, F. Migliavacca, L. Formaggia, A. Veneziani, M. Tuveri*, et al.*, "Computational models to predict stenosis growth in carotid arteries: Which is the role

of boundary conditions?," *Computer Methods in Biomechanics and Biomedical Engineering,* vol. 12, pp. 113-123, 2009.

[191] U. Morbiducci, D. Gallo, D. Massai, F. Consolo, R. Ponzini, L. Antiga*, et al.*, "Outflow conditions for image-based hemodynamic models of the carotid bifurcation: implications for indicators of abnormal flow," *J Biomech Eng,* vol. 132, p. 091005, Sep 2010.

[192] U. Morbiducci, D. Gallo, D. Massai, R. Ponzini, M. A. Deriu, L. Antiga*, et al.*, "On the importance of blood rheology for bulk flow in hemodynamic models of the carotid bifurcation," *J Biomech,* vol. 44, pp. 2427-38, Sep 2 2011.

[193] K. R. Moyle, L. Antiga, and D. A. Steinman, "Inlet conditions for image-based CFD models of the carotid bifurcation: is it reasonable to assume fully developed flow?," *J Biomech Eng,* vol. 128, pp. 371-9, Jun 2006.

[194] D. Ambrosi, A. Quarteroni, and G. Rpzza, *Modeling of Physiological Flows*. Milan: Springer-Verlag, 2011.

[195] A. Zupančič Valant, L. Žiberna, Y. Papaharilaou, A. Anayiotos, and G. C. Georgiou, "The influence of temperature on rheological properties of blood mixtures with different volume expanders—implications in numerical arterial hemodynamics simulations," *Rheologica Acta,* vol. 50, pp. 389-402, 2011.

[196] I. Marshall, P. Papathanasopoulou, and K. Wartolowska, "Carotid flow rates and flow division at the bifurcation in healthy volunteers," *Physiological Measurement,* vol. 25, pp. 691-697, Jun 2004.

[197] H. C. Groen, L. Simons, Q. J. van den Bouwhuijsen, E. M. Bosboom, F. J. Gijsen, A. G. van der Giessen*, et al.*, "MRI-based quantification of outflow boundary conditions for computational fluid dynamics of stenosed human carotid arteries," *J Biomech,* vol. 43, pp. 2332-8, Aug 26 2010.

[198] A. Manbachi, Y. Hoi, B. A. Wasserman, E. G. Lakatta, and D. A. Steinman, "On the shape of the common carotid artery with implications for blood velocity profiles," *Physiol Meas,* vol. 32, pp. 1885-97, Dec 2011.

[199] X. He and D. N. Ku, "Unsteady entrance flow development in a straight tube," *J Biomech Eng,* vol. 116, pp. 355-60, Aug 1994.

[200] Y. Hoi, B. A. Wasserman, E. G. Lakatta, and D. A. Steinman, "Effect of common carotid artery inlet length on normal carotid bifurcation hemodynamics," *J Biomech Eng,* vol. 132, p. 121008, Dec 2010.

[201] J. R. Womersley, "Method for the calculation of velocity, rate of flow and viscous drag in arteries when the pressure gradient is known," *J Physiology,* vol. 127, pp. 553-563, 1955.

[202] D. W. Holdsworth, C. J. Norley, R. Frayne, D. A. Steinman, and B. K. Rutt, "Characterization of common carotid artery blood flow waveforms in normal human subjects," *Physiol Meas,* vol. 20, pp. 219-40, Aug 1999.

[203] M. D. Ford, Y. J. Xie, B. A. Wasserman, and D. A. Steinman, "Is flow in the common carotid artery fully developed?," *Physiol Meas,* vol. 29, pp. 1335-49, Nov 2008.

[204] ANSYS, *FLUENT 12.0 Theory Guide*: ANSYS Inc., 2009.

[205] Y. Papaharilaou, N. Aristokleous, I. Seimenis, M. I. Khozeymeh, G. C. Georgiou, B. C. Brott*, et al.*, "Effect of head posture on the healthy human carotid bifurcation hemodynamics," *Med Biol Eng Comput,* vol. 51, pp. 207-18, Feb 2013.

[206] P. H. Stone, A. U. Coskun, S. Kinlay, M. E. Clark, M. Sonka, A. Wahle*, et al.*, "Effect of endothelial shear stress on the progression of coronary artery disease, vascular remodeling, and in-stent restenosis in humans: in vivo 6-month follow-up study," *Circulation,* vol. 108, pp. 438-44, Jul 29 2003.

[207] Tecplot, *Tecplot 360 User's Manual*: Tecplot, Inc., 2011.
[208] D. A. Steinman, "Simulated pathline visualization of computed periodic blood flow patterns," *J Biomech,* vol. 33, pp. 623-8, May 2000.
[209] J. M. Zhang, L. P. Chua, D. N. Ghista, T. M. Zhou, and Y. S. Tan, "Validation of numerical simulation with PIV measurements for two anastomosis models," *Med Eng Phys,* vol. 30, pp. 226-47, Mar 2008.
[210] N. A. Buchmann, M. Yamamoto, M. Jermy, and T. David, "Particle Image Velocimetry (PIV) and Computational Fluid Dynamics (CFD) Modelling of Carotid Artery Haemodynamics under Steady Flow: A Validation Study," *Journal of Biomechanical Science and Engineering,* vol. 5, pp. 421-436, 2010.
[211] R. O. Bude and J. M. Rubin, "Relationship between the resistive index and vascular compliance and resistance," *Radiology,* vol. 211, pp. 411-417, May 1999.
[212] C. H. Bai, J. R. Chen, H. C. Chiu, and W. H. Pan, "Lower blood flow velocity, higher resistance index, and larger diameter of extracranial carotid arteries are associated with ischemic stroke independently of carotid atherosclerosis and cardiovascular risk factors," *J Clin Ultrasound,* vol. 35, pp. 322-30, Jul-Aug 2007.
[213] R. L. Vanninen, H. I. Manninen, P. L. Partanen, P. A. Vainio, and S. Soimakallio, "Carotid artery stenosis: clinical efficacy of MR phase-contrast flow quantification as an adjunct to MR angiography," *Radiology,* vol. 194, pp. 459-67, Feb 1995.
[214] M. Schoning, J. Walter, and P. Scheel, "Estimation of Cerebral Blood-Flow through Color Duplex Sonography of the Carotid and Vertebral Arteries in Healthy-Adults," *Stroke,* vol. 25, pp. 17-22, Jan 1994.
[215] U. Morbiducci, D. Gallo, R. Ponzini, D. Massai, L. Antiga, F. M. Montevecchi*, et al.*, "Quantitative analysis of bulk flow in image-based hemodynamic models of the carotid bifurcation: the influence of outflow conditions as test case," *Ann Biomed Eng,* vol. 38, pp. 3688-705, Dec 2010.
[216] I. C. Campbell, J. Ries, S. S. Dhawan, A. A. Quyyumi, W. R. Taylor, and J. N. Oshinski, "Effect of inlet velocity profiles on patient-specific computational fluid dynamics simulations of the carotid bifurcation," *J Biomech Eng,* vol. 134, p. 051001, May 2012.
[217] D. Bluestein, Y. Alemu, I. Avrahami, M. Gharib, K. Dumont, J. J. Ricotta*, et al.*, "Influence of microcalcifications on vulnerable plaque mechanics using FSI modeling," *J Biomech,* vol. 41, pp. 1111-8, 2008.
[218] Y. Vengrenyuk, S. Carlier, S. Xanthos, L. Cardoso, P. Ganatos, R. Virmani*, et al.*, "A hypothesis for vulnerable plaque rupture due to stress-induced debonding around cellular microcalcifications in thin fibrous caps," *Proc Natl Acad Sci U S A,* vol. 103, pp. 14678-83, Oct 3 2006.
[219] D. Tang, C. Yang, J. Zheng, P. K. Woodard, G. A. Sicard, J. E. Saffitz*, et al.*, "3D MRI-based multicomponent FSI models for atherosclerotic plaques," *Ann Biomed Eng,* vol. 32, pp. 947-60, Jul 2004.
[220] J. Golledge, R. M. Greenhalgh, and A. H. Davies, "The symptomatic carotid plaque," *Stroke,* vol. 31, pp. 774-81, Mar 2000.
[221] C. J. Slager, J. J. Wentzel, F. J. Gijsen, A. Thury, A. C. van der Wal, J. A. Schaar*, et al.*, "The role of shear stress in the destabilization of vulnerable plaques and related therapeutic implications," *Nat Clin Pract Cardiovasc Med,* vol. 2, pp. 456-64, Sep 2005.
[222] C. Yang, R. G. Bach, J. Zheng, I. E. Naqa, P. K. Woodard, Z. Teng*, et al.*, "In vivo IVUS-based 3-D fluid-structure interaction models with cyclic bending and anisotropic vessel properties for human atherosclerotic coronary plaque mechanical analysis," *IEEE Trans Biomed Eng,* vol. 56, pp. 2420-8, Oct 2009.

[223] Z. Y. Li, S. P. Howarth, T. Tang, and J. H. Gillard, "How critical is fibrous cap thickness to carotid plaque stability? A flow-plaque interaction model," *Stroke,* vol. 37, pp. 1195-9, May 2006.

[224] D. Massai, G. Soloperto, D. Gallo, X. Y. Xu, and U. Morbiducci, "Shear-induced platelet activation and its relationship with blood flow topology in a numerical model of stenosed carotid bifurcation," *European Journal of Mechanics B-Fluids,* vol. 35, pp. 92-101, Sep-Oct 2012.

[225] D. Tang, C. Yang, J. Zheng, P. K. Woodard, J. E. Saffitz, J. D. Petruccelli*, et al.*, "Local maximal stress hypothesis and computational plaque vulnerability index for atherosclerotic plaque assessment," *Ann Biomed Eng,* vol. 33, pp. 1789-801, Dec 2005.

[226] S. E. Lee, S. W. Lee, P. F. Fischer, H. S. Bassiouny, and F. Loth, "Direct numerical simulation of transitional flow in a stenosed carotid bifurcation," *J Biomech,* vol. 41, pp. 2551-61, Aug 7 2008.

[227] M. X. Li, J. J. Beech-Brandt, L. R. John, P. R. Hoskins, and W. J. Easson, "Numerical analysis of pulsatile blood flow and vessel wall mechanics in different degrees of stenoses," *J Biomech,* vol. 40, pp. 3715-24, 2007.

[228] G. L. Jiang, C. R. White, H. Y. Steven, M. R. Inzunza, and J. A. Frangos, "Temporal gradients in shear, but not ramp flow, stimulate the proliferation of osteoblast-like cells.," *Journal of Bone and Mineral Research,* vol. 16, pp. S494-S494, Sep 2001.

[229] A. W. Vos, M. A. Linsen, J. T. Marcus, J. C. van den Berg, J. A. Vos, J. A. Rauwerda*, et al.*, "Carotid artery dynamics during head movements: a reason for concern with regard to carotid stenting?," *J Endovasc Ther,* vol. 10, pp. 862-9, Oct 2003.

[230] A. R. Valibhoy, B. P. Mwipatayi, and K. Sieunarine, "Fracture of a carotid stent: an unexpected complication," *J Vasc Surg,* vol. 45, pp. 603-6, Mar 2007.

[231] N. Diehm, S. Baum, B. T. Katzen, M. Kovacs, and J. Benenati, "Fracture of a carotid stent: a word of caution," *J Vasc Interv Radiol,* vol. 19, pp. 622-3, Apr 2008.

[232] F. Auricchio, M. Conti, M. De Beule, G. De Santis, and B. Verhegghe, "Carotid artery stenting simulation: from patient-specific images to finite element analysis," *Med Eng Phys,* vol. 33, pp. 281-9, Apr 2011.

[233] J. R. Cebral, F. Mut, M. Raschi, E. Scrivano, R. Ceratto, P. Lylyk*, et al.*, "Aneurysm rupture following treatment with flow-diverting stents: computational hemodynamics analysis of treatment," *AJNR Am J Neuroradiol,* vol. 32, pp. 27-33, Jan 2011.

[234] D. Fiorella, C. Sadasivan, H. H. Woo, and B. Lieber, "Regarding 'aneurysm rupture following treatment with flow-diverting stents: computational hemodynamics analysis of treatment'," *AJNR Am J Neuroradiol,* vol. 32, pp. E95-E97; author reply E98-E100, 2011.

[235] D. A. Steinman, D. A. Vorp, and C. R. Ethier, "Computational modeling of arterial biomechanics: insights into pathogenesis and treatment of vascular disease," *J Vasc Surg,* vol. 37, pp. 1118-28, May 2003.

[236] D. A. Steinman, Y. Hoi, P. Fahy, L. Morris, M. T. Walsh, N. Aristokleous*, et al.*, "Variability of Computational Fluid Dynamics Solutions for Pressure and Flow in a Giant Aneurysm: The ASME 2012 Summer Bioengineering Conference CFD Challenge," *J Biomech Eng,* vol. 135, p. 021016, Feb 2013.

Appendices

Appendix I: Publications

Publications in Peer Reviewed Journal Papers

- **N. Aristokleous**, I. Seimenis, G. C. Georgiou, Y. Papaharilaou, B. C. Brott and A. S. Anayiotos, "Impact of Head Rotation on the Individualized Common Carotid Flow and Carotid Bifurcation Hemodynamics," IEEE Trans. Inf. Technol. Biomed., (submitted/under review), Apr 2013.

- D. A. Steinman, Y. Hoi, P. Fahy, L. Morris, M. T. Walsh**, N. Aristokleous**, et al., "Variability of Computational Fluid Dynamics Solutions for Pressure and Flow in a Giant Aneurysm: The ASME 2012 Summer Bioengineering Conference CFD Challenge," J Biomech Eng, vol. 135, p. 021016, Feb 2013.

- Y. Papaharilaou, **N. Aristokleous**, I. Seimenis, M. I. Khozeymeh, G. C. Georgiou, B. C. Brott, E. Eracleous and A. S. Anayiotos, "Effect of Head Posture on the Healthy Human Carotid Bifurcation Hemodynamics," Med Biol Eng Comput, vol. 51, pp. 207 - 18, Feb 2013.

- **N. Aristokleous**, I. Seimenis, Y. Papaharilaou, G. C. Georgiou, B. C. Brott, E. Eracleous and A. S. Anayiotos, "Effect of Posture Change on the Geometric Features of the Healthy Carotid Bifurcation," IEEE Trans. Inf. Technol. Biomed., vol. 15, pp. 148-154, Jan 2011.

Publications in International Conference Proceedings

- **N. Aristokleous**, Y. Papaharilaou, I. Seimenis, G. C. Georgiou, B. C. Brott, and A. S. Anayiotos. “Head Rotation Effects on the Flow and Hemodynamics of the Human Carotid Bifurcation”. ASME 2013 Summer Bioengineering Conference, Sunriver, Oregon, USA, June 26-29 2013.

- **N. Aristokleous**, I. Seimenis, Y. Papaharilaou, M. I. Khozeymeh, G. Georgiou, B. Brott, and A. Anayiotos, “Head Posture Influences the Geometric and Hemodynamic Features on the Healthy Human Carotid Bifurcation”, Bioinformatics & Bioengineering (BIBE), 2012 IEEE 12th International Conference on, pp. 727-731, November 11-13, 2012, Larnaka, Cyprus.

- **N. Aristokleous**, I. Seimenis, Y. Papaharilaou, E. Eracleous, G. C. Georgiou, B. C. Brott, and A. S. Anayiotos, “Head Rotation Influences the Geometric Features of the Stenotic Carotid Bifurcation”, ASME 2012 Summer Bioengineering Conference, Farjardo, Puerto Rico, USA, June 20-23, 2012.

- **N. Aristokleous**, M. I. Khozeymeh, Y. Papaharilaou, G. C. Georgiou, and A. S. Anayiotos “Inaugural CFD Challenge Workshop: Solutions Using the Commercial

Finite Volume Solver Fluent", ASME 2012 Summer Bioengineering Conference, Farjardo, Puerto Rico, USA, June 20-23, 2012.

- **N. Aristokleous**, I. Seimenis, Y. Papaharilaou, G. Georgiou, B. Brott, and A. Anayiotos, "Rightward And Leftward Head Rotation Influence The Geometric Features Of The Healthy Carotid Bifurcation", ASME 2011 Summer Bioengineering Conference, 22-25 June, 2011, Famington, Pennsylvania, USA.

- **N. Aristokleous**, I. Seimenis, Y. Papaharilaou, G. Georgiou, B. Brott and A. Anayiotos, "Effect of Posture Change on the Geometric Features of The Healthy Carotid Bifurcation", ASME 2010 Summer Bioengineering Conference. 16-19 June, 2010, Naples, Florida, USA.

- **N. Aristokleous**, I. Seimenis, Y. Papaharilaou, G. Georgiou, B. Brott and A. Anayiotos, "Effect of Posture Change On The Geometric Features Of The Healthy Carotid Bifurcation", IEEE 9th International Conference on Information Technology & Applications in Biomedicine. 4-7 November, 2009, Larnaca, Cyprus.

Appendix II: Murray's Law Results

Table A1: Murray's Law results (n=40)

	RADIUS			Parameters	
n	CCA3	ICA5	ECA1	BI=ECA/ICA	BAR=$(ICA^2 + ECA^2)/CCA^2$
1	3.12	2.81	2.09	0.74	1.26
2	2.83	2.68	2.3	0.86	1.56
3	3.22	1.97	2.82	1.43	1.14
4	3.39	2.49	3.04	1.22	1.34
5	3.56	2.9	3.02	1.04	1.38
6	3.64	3.09	2.8	0.91	1.31
7	3.31	2.56	2.09	0.82	1.00
8	3.2	2.73	2.06	0.75	1.14
9	2.95	2.37	2.63	1.11	1.44
10	2.97	2.37	2.81	1.19	1.53
11	2.97	2.27	2.58	1.14	1.34
12	3.2	2.61	2.36	0.90	1.21
13	3.3	2.58	2.48	0.96	1.18
14	3.26	2.5	2.22	0.89	1.05
15	3.64	2.68	2.68	1.00	1.08
16	3.49	2.6	3.19	1.23	1.39
17	3.63	2.95	2.04	0.69	0.98
18	3.24	2.55	2.62	1.03	1.27
19	3.2	2.82	2.25	0.80	1.27
20	3.01	2.97	1.8	0.61	1.33
21	3.19	3.01	2.16	0.72	1.35
22	3.14	2.9	2.84	0.98	1.67
23	3.17	2.26	2.65	1.17	1.21
24	2.87	1.92	2.54	1.32	1.23
25	3.42	2.85	2.86	1.00	1.39
26	3.27	2.77	2.71	0.98	1.40
27	3.17	2.82	2.04	0.72	1.21
28	3.24	2.64	2.16	0.82	1.11
29	2.91	2.36	2.56	1.08	1.43
30	3.02	2.49	2.59	1.04	1.42
31	3.21	2.62	2.42	0.92	1.23
32	3.12	2.25	2.02	0.90	0.94
33	3.28	2.32	1.92	0.83	0.84
34	3.16	2.47	2.18	0.88	1.09
35	3.26	2.56	2.52	0.98	1.21
36	3.32	2.52	2.46	0.98	1.13
37	3.1	2.32	2.37	1.02	1.14
38	3.61	2.93	2.38	0.81	1.09
39	3.05	2.85	1.99	0.70	1.30
40	3.26	2.83	2.02	0.71	1.14
mean	3.22	2.60	2.43	0.95	1.24
median	3.21	2.61	2.44	0.94	1.23

Murray's Law: mean: $3.22^3 = 2.6^3 + 2.43^3$ <=> 38.39 = 31.92 (16.9 %)
median: $3.21^3 = 2.61^3 + 2.44^3$ <=> 33.08 = 32.31 (2.3 %)

Square Law: mean: $3.22^2 = 2.6^2 + 2.43^2$ <=> 10.37 = 12.66 (22.1 %)
median: $3.21^2 = 2.61^2 + 2.44^2$ <=> 10.30 = 12.77 (24.0 %)

The median values from 40 carotids obey Murray's law in this study.

Appendix III: Realistic Velocity Waveform Acquired from PC-MRI

The flow data acquired for the purposes of this study, from PC-MRI, are in the form of discrete data points. The velocity is represented as intensity in each pixel for each cardiac phase and is not an analytical function that could be analytically integrated to give a periodic signal. Thus, the calculations needed to be performed numerically. First, the data were transformed to a continuous function and after using the Fourier series presented in section 7.5.1 with the integral equations 7.11-7.13, the Fourier coefficients were provited.

The best and easiest way to compute the Fourier transformation of discrete data is the Fast Fourier Transform (FFT), and with the use of FFT, all the coefficients were calculated. The FFT is applied only when the number of points is a power of 2 (*N=2,4,8,16,32,…*), so the first step was to use an interpolation technique to recapture 256 discrete points from the initial 20. The decision for so many points was to achieve smoothness of the velocity curve and to approximate better the realistic heart pulse. Figure A1 represents the rough curve from the initial 20 points, and also the graphs of 256 points with the use of interpolation, spline and polyfit techniques in Matlab (R2012b, WathWorks). The same results are presented in Fig. A2 with superposition of the graphs showing that the spline technique is closer to real values. From the 256 points, the highest frequency is 128 and the ordering of the frequencies is [0 1 2 3 … 127 128 -127 -126 … -2 -1]. The first 128 frequencies are the positive frequencies and the second half is the negative. The ordering is called reverse wrap-around order.

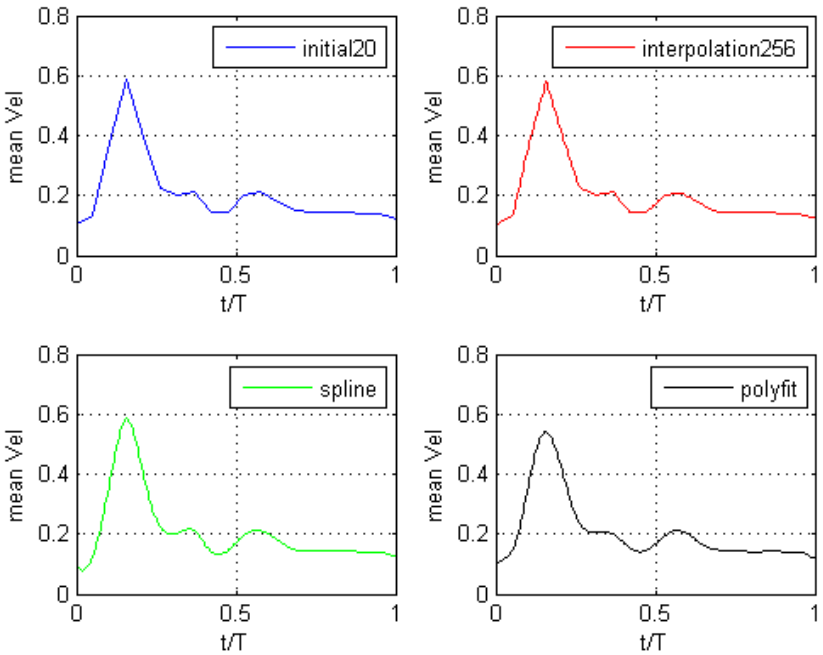

Figure A1: Velocity waveform from the initial 20 points and from 256 points using interpolation, spline, and polyfit.

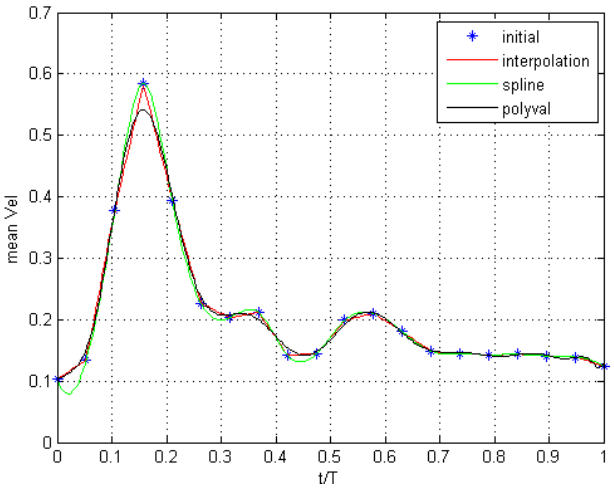

Figure A2: The superposition of graphs show that spline technique is closer to real values.

The Matlab code for spline interpolation:

```
% This script is to interpolate to 256 discrete points
% Also uses spline and polyfit to plot the mean velocity vs t/T
clear all;
clc ;

data =load ('a20.txt');

x=data(:,1);
y=data(:,2);
```

```
xi=(0:1/255:1)';
L=erf(xi);

yi = interp1 (x,y,xi);

%figure(1);
subplot(2,2,1);
plot (x,y)
grid on;
box on;
xlabel ('t/T');
ylabel ('mean Vel')
legend ('initial20')

%figure(2);
subplot(2,2,2);
plot (xi,yi, 'r')
grid on;
box on;
xlabel ('t/T');
ylabel ('mean Vel')
legend ('interpolation256')

zi= spline (x,y,xi);

%figure(3);
subplot(2,2,3);
plot (xi,zi, 'g')
grid on;
box on;
xlabel ('t/T');
ylabel ('mean Vel')
legend ('spline')
axis([])

p=polyfit(xi,yi,17);
f=polyval(p,xi);

%figure(4);
subplot(2,2,4);
plot (xi,f, 'k')
grid on;
box on;
xlabel ('t/T');
ylabel ('mean Vel')
legend ('polyfit')
```

The use of the FFT leads to complex numbers the real part of which corresponds to the cosines and the imaginary part corresponds to the sines. To obtain the real values for Fourier coefficients, an appropriate scaling and rearrangement of values is necessary. The coefficients from FFT are:

$$\alpha_n = \frac{1}{2N} real(c_n), 0 < n < \frac{N}{2}$$

$$b_n = -\frac{1}{2N} imag(c_n), 0 < n < \frac{N}{2}$$

where N=256/2

For the confirmation of the results, for one case, the Fourier coefficients were calculated by numerical summation and using the numerical integration (Trapezoidal Rule).

Table A2: The first seven Fourier coefficients represent agreement, calculated with three techniques.

Harm-onics	Numerical Summation		Num. Trapezoidal Rule		FFT		FFT13	
	a	b	a	b	a	b	a	b
0	0,2099	-	0,2090	-	0,2083	-	0,2083	-
1	0,0247	0,0915	0,0229	0,0915	0,0230	0,0911	0,0230	0,0911
2	-0,0440	0,0775	-0,0458	0,0775	-0,0444	0,0776	-0,0444	0,0776
3	-0,0649	-0,0079	-0,0667	-0,0079	-0,0678	-0,0064	-0,0678	-0,0064
4	-0,0422	-0,0263	-0,0440	-0,0263	-0,0441	-0,0248	-0,0441	-0,0248
5	0,0079	-0,0473	0,0062	-0,0473	0,0035	-0,0480	0,0035	-0,0480
6	0,0157	-0,0070	0,0176	-0,0070	0,0179	-0,0078	0,0179	-0,0078
7	0,0076	-0,0003	0,0058	-0,0003	0,0058	-0,0001	0,0058	-0,0001

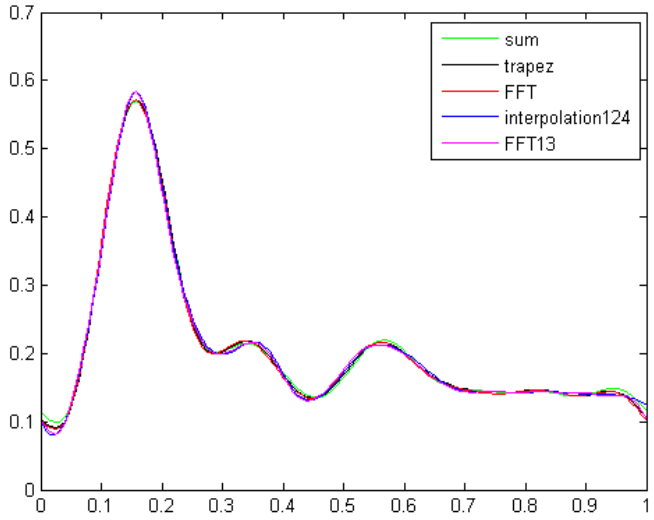

Figure A3: The velocity waveform calculated with various techniques.

The Matlab code for the Fourier coefficients calculation:

```
% This script gives the Fourier Coefficients a,b
% Using the Trapezoidal rule
% Plots the initial graph from discrete data and the reconstructed
% signal from coefficients

clear all
clc;
```

```
waveform=load( 'inter124.txt');

t = waveform(:,1)
f = waveform(:,2)

% find a_0

a0=trapz(t,f);

% find the rest coefficients

nm=7; % this is the number of modes. use more for better accuracy

for i=1:nm
    in1 = f.*cos(2*pi*(i)*t);
    in2 = f.*sin(2*pi*(i)*t);

    a(i)=2.*trapz(t,in1)
    b(i)=2.*trapz(t,in2)
end

%reconstruct the signal

fr=zeros(length(t),1);

for i =1:nm
    fr = fr+a(i)*cos(2*pi*i*t)+b(i)*sin(2*pi*i*t);
end

fr=fr+a0;

% plot the raw data

plot(t,f,'*',t,fr)
grid on;
xlabel('t/T')
ylabel('mean V')
legend ('Fourier Coefficients', 'Plot from discrete data');

% This script gives the Fourier Coefficients a,b
% Using the FFT

clear all;
clc;

data = load ('inter124.txt');

t= data (:, 1);
f= data (:, 2);

plot (t,f)

coeff = fft (f)

coeffss = conj (coeff)
```

```
cn = coeff./(length(t))

a0 = cn(1)

an = 2*real (cn(2:(length(t)/2)))
bn = -2*imag (cn(2:(length(t)/2)))

tf=[an bn]
save tf.txt an –ascii

% Using FFT to acquire the Fourier Coefficients

F = fft (zi);
F = conj (F);

an = (1/length(zi))*real (F (129:end));
bn = -(1/length(zi))*imag (F (129:end));

a0=(1/length(zi))*real (F(1));
a=2*an(2:end);
b=2*bn(2:end);

a=fliplr(a);
b=fliplr(b);
```

Appendix IV: Impact in Flow Data from the Number of Phases per Cardiac Cycle

The flow data acquired in this study from PC-MRI were spread in 20 phases throughout the cardiac phase. For an individual, the acquired flow data were in 40 phases, for the supine position and for both CB. Figure A4 below shows good agreement between the data acquired with different resolution time, rather than the expected higher differences, as the possibility to miss the peak-systole is greater in smaller number rather in bigger number of phases.

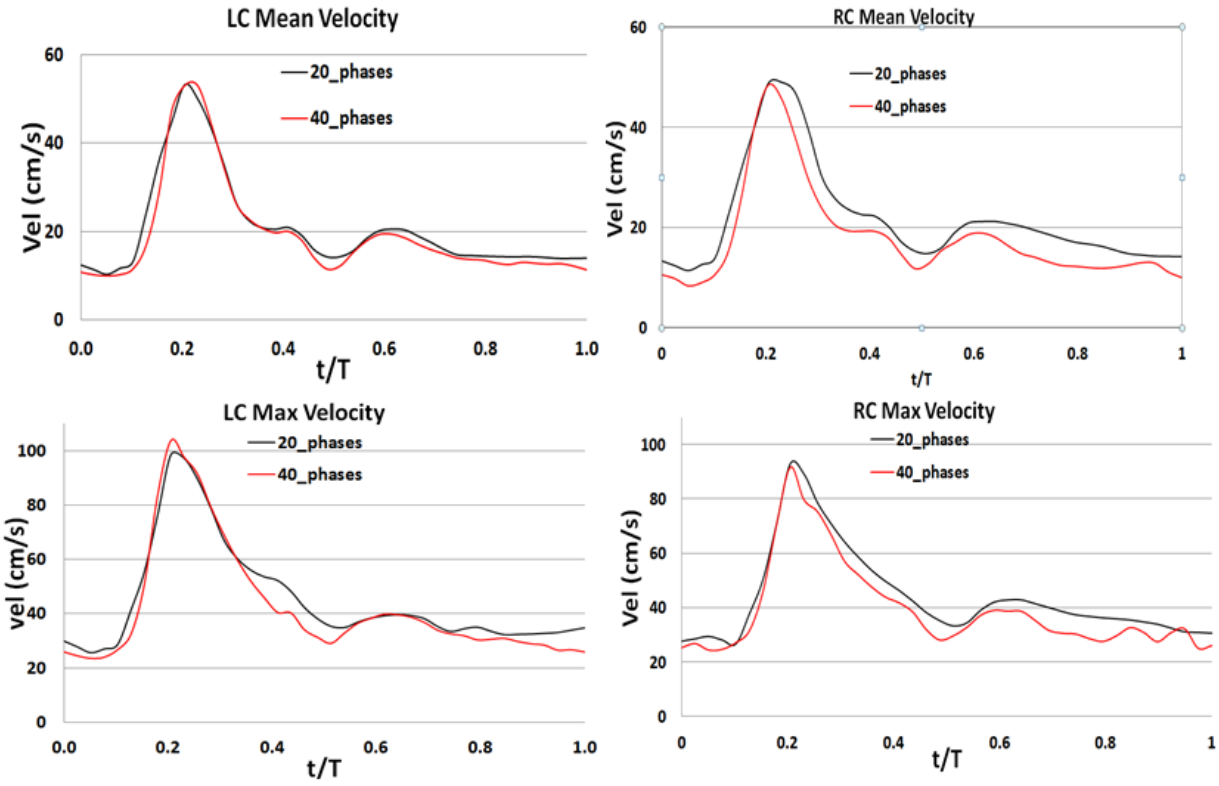

Figure A4: The averaged-velocity waveforms for 20-phases and 40-phases data for both CB (Above). The maximum velocity waveforms for 20-phases and 40-phases data for both CBs (Below).

Appendix V: CFD Solutions for Pressure and Flow in a Giant Aneurysm

This study was presented in a workshop for the American Society of Mechanical Engineers (ASME) 2012 Summer Bioengineering Conference (SBC). In more detail, after the publication of Cebral *et al.* [233] for computational hemodynamics in an aneurysm, Fiorella *et al.* [234] mentioned that the pressure drops were abnormally high and expressed concerns regarding CFD solution errors. Steinman [235] replied that pressures may be overestimated because of other reasons rather the CFD solution. So an imaged-based CFD challenge took place and around 25 different groups participated. All contributed groups were provided with the same surface model and the same inlet boundary conditions. All performed CFD simulations using any strategy they preferred to reach accurate results for the pressures and velocities. This workshop was to estimate the variability of CFD solutions and to compare the results with those in Cebral et al. [233]. The results were presented at ASME SBC 2012 and also in the publication of Steinman [236]. To perform the simulations for this study, as already mentioned, the same lumen geometry of a giant cerebral aneurysm was used as in the study of Cebral *et al.* [233] and referred to as patient #1. The surface model and the inlet boundary conditions are represented in Fig. A5.

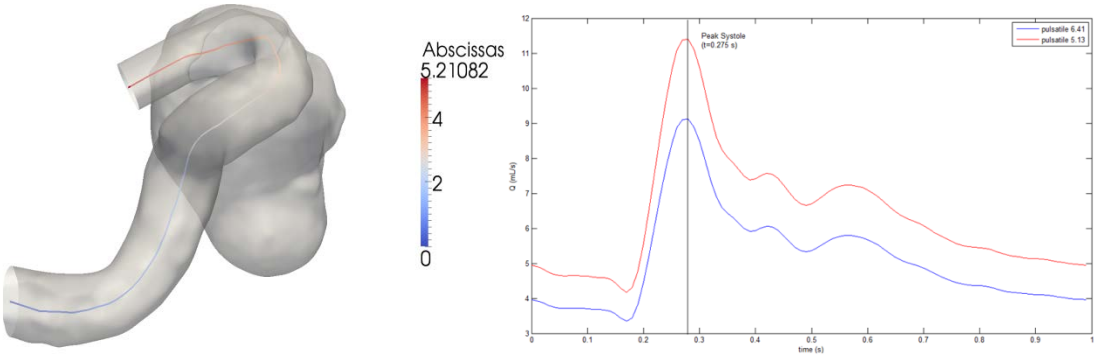

Figure A5: Surface model of the investigated aneurysm with the centerline represents the abscissa distance (cm) from inlet to outlet (left). The pulsatile flow rates was used as inlet boundary conditions (right).

Figure A6 presents the pressure values extracted along the centerline for all investigated cases. Inlet pressure was set to 90 and 120 mmHg for the averaged and peak systole respectively.

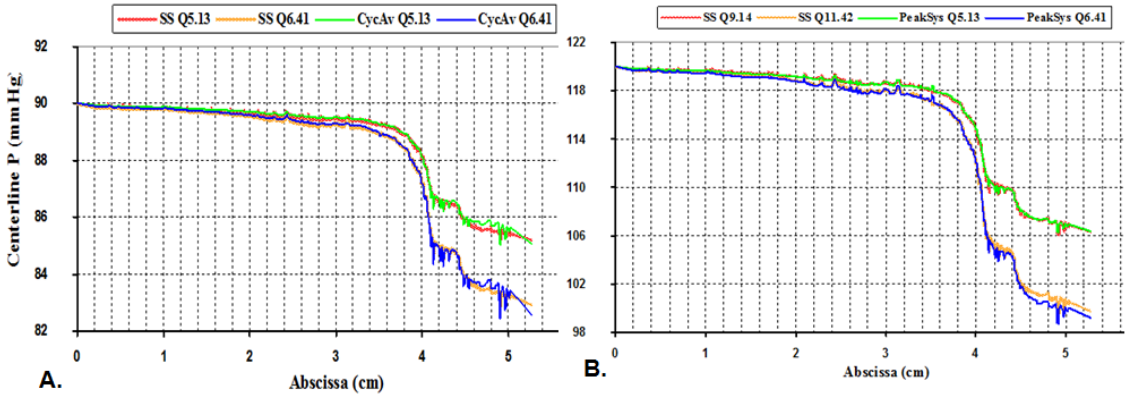

Figure A6: (A) Steady state (SS) and cycle-averaged (CycAv) centerline pressure. (B) Steaty state and peak systolic centerline pressures.

Figure A7 depicts the 3D plots of peak systolic velocity and surface pressure distributions for the two pulsatile cases.

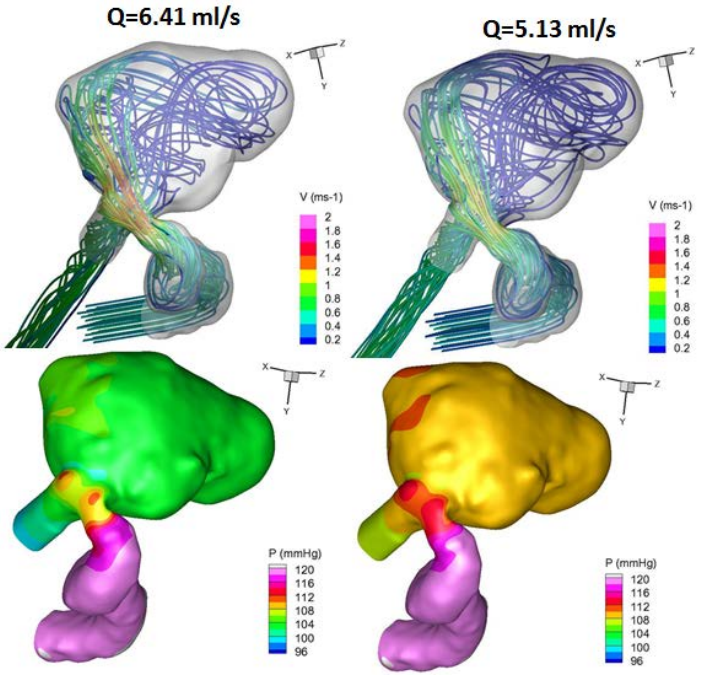

Figure A7: Velocity streamlines (above) and pressure distribution (below) at peak systole for the two pulsatile simulations with different flow rates.

The results indicate that the presence of the stenosis just proximal to the aneurysm ostium causes a peak systolic pressure drop of ~20 mmHg and a cycle averaged pressure drop of ~7 mmHg for case 1. For case 2 these values are ~14mmHg and ~5 mmHg respectively. Furthermore, only minor differences were observed, in the centerline

pressures between the time varying and steady state computations at peak systole flow rates (Fig. A6A). Thus, in this case the quasi steady assumption is acceptable in predicting both the peak systolic and the time averaged pressure drop along the centerline.

From the streamlines represented in Fig. A7, the conclusion was that as blood flows through the highly tortuous inlet conduit it obtains a spiral motion which is then further modulated by the lumen stenosis creating an asymmetric flow injection in the aneurismal sac. This asymmetric influx strongly influences the vortex structures that develop within the aneurismal expansion and the stress distribution on the sac wall. Finally, by comparing the results for the various steady and pulsatile flow cases shown in Fig. A6, the pressure drop across the stenosis, as expected, approximately scales with the flow rate.